CHEMICAL REVIEWS

pubs.acs.org/CR

Review

Conceptual and Practical Aspects of Metal−Organic Frameworks for Solid−Gas Reactions

Andrei Iliescu,[‡] Julius J. Oppenheim,[‡] Chenyue Sun,[‡] and Mircea Dincă*

Cite This: https://doi.org/10.1021/acs.chemrev.2c00537

Read Online

ACCESS | Metrics & More | Article Recommendations

ABSTRACT: The presence of site-isolated and well-defined metal sites has enabled the use of metal−organic frameworks (MOFs) as catalysts that can be rationally modulated. Because MOFs can be addressed and manipulated through molecular synthetic pathways, they are chemically similar to molecular catalysts. They are, nevertheless, solid-state materials and therefore can be thought of as privileged solid molecular catalysts that excel in applications involving gas-phase reactions. This contrasts with homogeneous catalysts, which are overwhelmingly used in the solution phase. Herein, we review theories dictating gas phase reactivity within porous solids and discuss key catalytic gas−solid reactions. We further treat theoretical aspects of diffusion within confined pores, the enrichment of adsorbates, the types of solvation spheres that a MOF might impart on adsorbates, definitions of acidity/basicity in the absence of solvent, the stabilization of reactive intermediates, and the generation and characterization of defect sites. The key catalytic reactions we discuss broadly include reductive reactions (olefin hydrogenation, semihydrogenation, and selective catalytic reduction), oxidative reactions (oxygenation of hydrocarbons, oxidative dehydrogenation, and carbon monoxide oxidation), and C−C bond forming reactions (olefin dimerization/polymerization, isomerization, and carbonylation reactions).

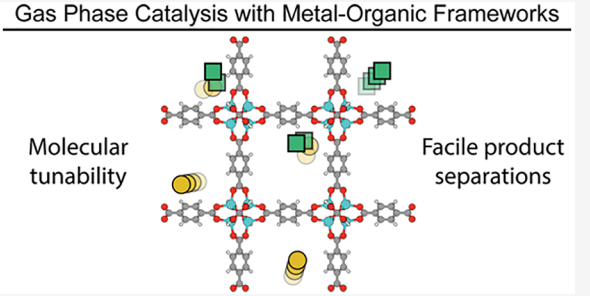

CONTENTS

1. INTRODUCTION

The reactivity of small molecule substrates, such as dihydrogen (H_2), dioxygen (O_2), dinitrogen (N_2), carbon monoxide (CO), carbon dioxide (CO_2), methane (CH_4), and ethylene (C_2H_4), is vital for the transformation of abundant feedstocks into higher-value products. However, challenges of kinetic

Special Issue: Bridging the Gaps: Learning from Catalysis across Boundaries

Received: August 1, 2022

stability (e.g., in the case of the strong nitrogen−nitrogen triple bond of N_2), high oxidation potential and over-reactivity (e.g., in the case of oxidation of substrates using O_2), and selectivity (e.g., in the case of olefin oligomerization to a distribution of products), among others, arise in the course of upgrading these simple, inexpensive gases into desirable commodity chemicals. The recognized value of addressing these challenges has engendered the search for so-called *designer catalysts*, able to selectively transform substrates into specific products. The rational design and synthesis of these ideal catalysts typically require precise control of the immediate and long-range chemical environments surrounding the catalytic center. To this end, a great deal of research has been carried out over the past many decades using soluble transition metal complexes, due to their ease of characterization and rational design.[1−6]

Although the advances in homogeneous catalysis have been and continue to be instrumental in the quest for efficient small molecule reactivity, heterogeneous catalysis represents an advantageous alternative. With respect to small molecule reactivity in particular, the use of solid-state catalysts for gas phase reactions provides an attractive option. From an application standpoint, gas−solid catalysis provides several industrial and environmental benefits. In the absence of solvent, solid catalysts are less prone to demetalation, leaching, and aggregation, leading to an improvement in lifetime. The lack of solvent also reduces the cost and energy consumption of separation and purification processes, while also producing significantly less chemical waste.[7] Solid catalysts can be easily recycled and reused and even used under flow conditions for continuous industrial processes. Additionally, the use of solid-state catalysts in the absence of solvent opens up new reactivity pathways, as common unproductive mechanisms, such as intramolecular or bimolecular degradation pathways, are greatly discouraged or entirely prohibited on solid supports.[8]

Among solid materials primed for catalysis with small molecule substrates, metal−organic frameworks (MOFs) emerge as particularly attractive candidates. MOFs are porous lattices composed of well-defined molecular building blocks: organic linkers and inorganic secondary building units (SBUs).[9,10] The distinctive characteristic of MOFs, compared to other solid platforms, is their well-defined structure and chemistry. As in the case of molecular complexes, MOFs are modular and highly tunable materials (Figure 1). The ability to methodically vary the metal used, the oxidation state of the metal, the electronic density at the metal by changing the electronics of the linker, and the steric profile of the active site by changing the topology of the MOF offers the possibility to fine-tune the primary and secondary coordination spheres of the catalytic active site. Additionally, the inherent porosity of MOFs leads to very high surface areas and, therefore, high concentration of active sites for catalysis within the pores of the materials.[11,12] Moreover, within MOFs, the active sites can often be easily studied and understood: they can be directly observed, via single-crystal X-ray, electron or neutron diffraction, or indirectly determined, via spectroscopy, diffraction, and computational methodologies.[13−17]

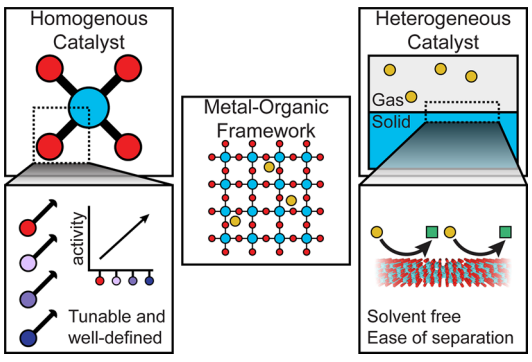

Figure 1. Metal−organic framework catalysts combine aspects of both homogeneous and heterogeneous catalysts.

On the other hand, the use of MOFs as solid catalysts for small molecule reactivity comes with its own caveats and limitations, some shared with molecular complexes and some unique to this class of materials. Similar to many organic and organometallic materials, but distinct from other classes of solid catalysts such as zeolites, MOFs have more limited thermal stability windows, which might lie below the vaporization temperatures of certain substrates. This window can become more restricted in the presence of strong oxidants, such as nitric oxides and dioxygen, which destroy the structural components of MOFs at elevated temperatures.[18] In addition, the low heat capacity of gases causes heat dissipation in gas−solid reactions to be nontrivial. For catalysts that are sensitive to temperature, highly exothermic reactions may require the use of lower catalyst loadings and lower reactant concentrations to circumvent thermal deactivation. That said, controlled thermal decomposition of MOFs can sometimes be exploited to create highly reactive intermediates.[15,19] Additionally, some commonly used synthetic methodologies in solution chemistry are incompatible with MOFs. For example, chloride abstraction to create coordination vacancy can be achieved by soluble silver(I) reagents in solution, but the insoluble silver halide produced would clog the pores and cause irreversible contamination in the case of MOFs.[20] Similarly, solid-state reductants, such as potassium graphite or sodium metal, are also incompatible due to the poor contact between the solid reagent with the solid substrate and difficulty in separation. Lastly, kinetic studies of gas−solid reactions, while extremely informative, require more sophisticated setups and careful consideration of diffusion, defects, surface reactivity, as well as reaction processes.

Despite these obvious challenges, it has become increasingly evident in recent years that great synergy exists between the fields of MOFs and small molecule catalysis. This work aims to provide an overview of and contextualize recent advancements in this area of research, focusing specifically on those reactions involving *exclusively* gas and solid reactants and products under the temperature and pressure conditions of the reaction. First, general considerations of gas−solid reactivity within MOFs, in the context of catalysis and in contrast to homogeneous systems, will be discussed. Fundamentally, reactions occurring at the gas−solid interface can have drastically different energy profiles along the reaction trajectories due to changes in charge screening, and specific interactions with solvent molecules or the catalytic active site (e.g., in the form of hydrogen bonding, van der Waals interactions, Lewis acid−base interactions, etc.). The surface of MOFs can also provide favorable interactions to reactants, intermediates, or products, thereby further altering the energetic landscape of reactions and potentially influencing specificity and selectivity. Second, selected works from recent literature will be presented and analyzed. Key advances will be discussed, with an emphasis on innovative scientific discoveries and ingenious ways to circumvent apparent limitations in

https://doi.org/10.1021/acs.chemrev.2c00537
Chem. Rev. XXXX, XXX, XXX−XXX

MOF-catalyzed gas-phase reactivity studies, by either catalyst or experiment design. Some practical examples of stoichiometric gas−solid reactions in MOFs are also presented in those cases where catalytic turnover might be achieved in the future. This review is intended to comprehensively discuss key reaction classes for gas−solid MOF catalysis with illustrative examples, rather than discuss all possible types of gas−solid reactivity in MOFs. Readers interested in further content are directed to a previous relevant review on related topics.[21] Lastly, emerging trends in MOF-catalyzed small molecule activation will be identified and discussed, with the goal of drawing meaningful insights from literature precedents.

2. KINETIC AND THERMODYNAMIC CONSIDERATIONS OF GAS−SOLID HETEROGENEOUS CATALYSIS

The following sections strive to inform the readers of some key factors that deserve consideration when studying heterogeneous catalysis, with a focus on gas−solid, MOF-catalyzed reactions. Naturally, the most fundamental principles of catalysis govern this type of reactivity as well. That is, MOF catalysts act to promote chemical reactions that are thermodynamically feasible by providing alternative reaction pathways with lower energy transition states, and hence lower activation energies, compared to the uncatalyzed reactions. This reactivity is achieved by the specific binding and activation of substrates and/or intermediates. As in all reactions, the rates of MOF-catalyzed reactions are affected by the intrinsic abilities of the MOF active sites to activate substrates, which are dictated by the nature of active site−substrate interactions, and by the concentration of substrate (Figure 2). The strength of these interactions can be modulated via synthetic design and tuning of the MOF active site for the specific desired reactivity. However, the likelihood of these interactions depends on the concentration of the MOF active site and the concentration of substrate. While reactivity may occur on the outside surface of MOFs, the number of active sites is generally many orders of magnitude higher inside the pores of these materials and, hence, it is reasonable to assume that, given the right size match between the pores of the MOF and the substrate, as well as reasonably swift transport through the pores, reactivity occurs essentially entirely within the pores of the MOFs.[22] Thus, the concentration of substrate molecules inside the pores of MOFs must be considered, which is, in turn, influenced by the adsorption properties of the MOF as well as the diffusion of new substrate into the MOF as product diffuses out.

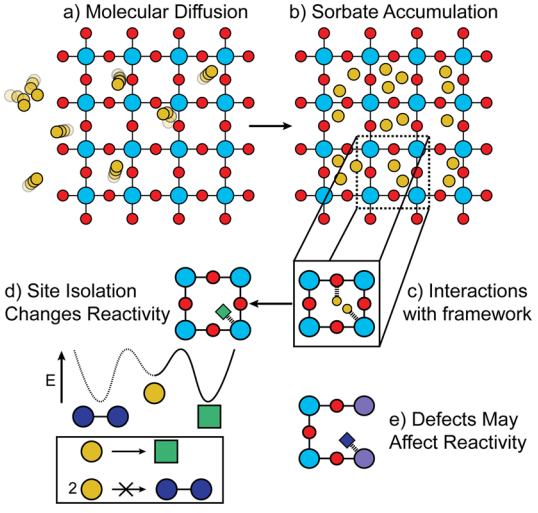

Figure 2. During a catalytic reaction inside the pores of a MOF, reactant molecules (a) diffuse to a MOF particle and then within the pores, (b) accumulate within the framework, (c) interact with various sites within the framework, including the active site as well as inert acidic/basic components of the framework, (d) may react in a manner different than that in homogeneous media due to site isolation, and (e) may react differently at defect sites within the framework.

The following sections will track a general reaction in which gas-phase substrate is converted into gas-phase product under MOF catalysis, illustrating important concepts with examples from recent literature. First, the diffusion of the substrate inside the pores of the MOFs will be discussed, and the role of gas pressure will be analyzed. Second, the accumulation of substrate in the pores and possible ways to increase its concentration will be considered. Next, the main factors dictating the chemical binding and activation of substrate within the pores will be reviewed, specifically solvation effects and acid−base interactions. The stabilization of reactive intermediates within the pores of MOFs via site isolation will then be discussed and contrasted with strategies commonly employed in solution chemistry. Lastly, the role of defects in MOF-catalyzed reactions will be analyzed.

2.1. Diffusion of Substrates within Confined Pores

A key advantage of MOF catalysis is the large concentration of active sites within the pores of these materials. An important consideration specific to MOF (and other porous material) catalysis is the ability of gas substrates to reach the active sites within these pores via diffusion. This section analyzes the factors governing the diffusion of gas molecules inside the confined pores of porous materials.

Diffusion within the confines of a MOF pore may be drastically different than that in homogeneous or nonconfined heterogeneous systems, thus greatly affecting reaction kinetics. Molecules surrounding MOF particles only move according to the bulk molecular diffusion and the motions of the fluid (e.g., in the case of flow reactions). However, the movement of molecules within the MOF pores is also affected by the fluxes of reactants and products into and out of the pores. The added complexity to molecular motions can greatly impact reaction rates and, if not considered properly, these diffusion factors may greatly inhibit overall reaction kinetics.[23]

Specifically, the mean free path of gas molecules, and hence all substrates considered later in this review, is often much greater than the diameter of MOF pores; understanding the implications of this fact is paramount to understanding the kinetics of MOF-catalyzed reactions involving gas-phase substrates. For example, the mean free path of dry air at 298 K and 1 atm is 67 nm,[24] whereas the vast majority of MOFs are microporous, with the pore diameter below 2 nm.[9] Even MOFs most renowned for their large pores, such as IRMOF-74-XI and MIL-101, with pore apertures of 9.8 and 3.4 nm, respectively, have pores far narrower than the mean free path of dry air.[25,26] This results in much more frequent collisions of the gas molecule with the pore walls than of the gas molecule with itself, giving rise to a regime termed Knudsen diffusion. Notably, this behavior does not typically apply to liquid molecules within porous materials as the mean free path of liquid molecules is on the same order of magnitude as the size

https://doi.org/10.1021/acs.chemrev.2c00537
Chem. Rev. XXXX, XXX, XXX−XXX

of liquid molecules. Therefore, the diffusion of liquid molecules in pores tends to fall under a molecular or intermediate regime.

Under a Knudsen diffusion regime, because collisions of the gas molecule with itself are significantly less likely than the collisions of the gas molecule with the porous material wall, the pressure of the gas molecule does not influence the diffusion flux. Broadly, the diffusion flux of a molecule is proportional to the diffusivity constant, D, and to the concentration gradient. In the limit of an unconfined molecular diffusion regime, the molecular diffusivity constant, D_M, is inversely proportional to the pressure. This is the result of increasing pressure leading to an increase in the number of intramolecular collisions given a set time frame. This, in turn, decreases the mean free path of the molecule and leads to an overall slower diffusion process. However, in the limit of Knudsen diffusion where the relevant collisions are those with the framework walls, the Knudsen diffusivity constant, D_K, is independent of pressure (Figure 3).[27] Instead, the Knudsen diffusivity coefficient scales with the

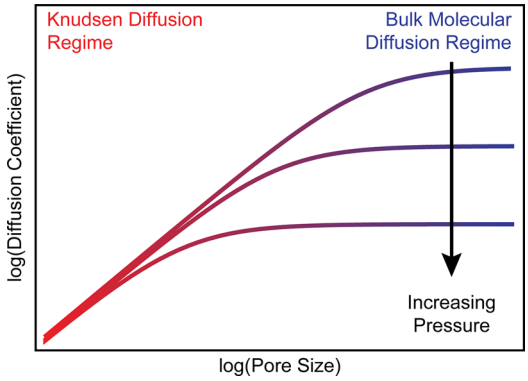

Figure 3. Relation of molecular and Knudsen diffusion on pressure and pore size. Under the Knudsen diffusion regime, commonly operating in the confined pores of MOFs, pressure changes do not impact the diffusion coefficient. However, increasing the pore sizes of MOFs increases the diffusion coefficients, and hence diffusion rates, of substrates within porous materials. Under bulk molecular diffusion or intermediate regimes, diffusion coefficients are larger in systems at low pressure.

pore radius and can be modulated by modifying the pore apertures of the framework. For example, in a 1D cylindrical channel, $D_K = \frac{2r}{3}\sqrt{\frac{8RT}{\pi M}}$, where r is the pore radius, R is the ideal gas constant, T is the temperature, and M is the molecular weight.[28] This is to say that in a small pore framework, if the reaction is diffusion-limited, reaction rates cannot be enhanced by pressure changes once steady-state concentration is established, but they could be influenced by varying the pore size of the porous material.

Besides Knudsen diffusion, other possible diffusion mechanisms in small-pore solids include viscous flow, surface diffusion, and single-file diffusion. For viscous flow, the molecules behave as a continuum and move in concert. The "apparent" diffusivity will scale as $D_V = \frac{B_0 P}{\mu}$, where B_0 is a parameter that scales with the square of pore diameter, P is the pressure, and μ is the viscosity.[29,30] The surface diffusion regime is one in which fluid molecules hop between surface sites. In this case, the diffusivity has a nonlinear dependence on surface coverage but typically increases with loading.[30] In the limiting case in which the pore size is comparable to the molecular size, single-file diffusion may occur, where molecules cannot pass by each other within the pore. Here, the mobility will decrease with increasing adsorbate−adsorbent interaction strength,[31] as well as with high concentrations of sorbate.[32]

Even though the effective diffusivity constant for a gas in a porous framework is three orders of magnitude greater than that for a liquid near room temperature,[28] if the pores of the framework are sufficiently small, the diffusion rate can be slower than the catalytic rate, which can be determined by calculating the Weisz−Prater parameter, C_{wp}.[27] Qualitatively, the Weisz−Prater parameter is equal to the actual reaction rate divided by the diffusion rate. Therefore, a large C_{wp} ($\gg 1$) is indicative of a mass transfer limited process because the reaction rate is much larger than the diffusion rate. In this case, catalysis occurs almost exclusively on or very close to the surface of the MOF. Quantitatively, the Weisz−Prater parameter can be calculated as $C_{wp} = \frac{k_{obs} R^2 / V_{cat}}{D_e C_s}$, where k_{obs} is the observed reaction rate, R is the catalyst particle radius, V_{cat} is the total catalyst volume, D_e is the effective diffusivity constant, and C_s is the substrate surface concentration. Because all of the parameters needed to calculate the Weisz−Prater parameter can be experimentally measured or otherwise determined, it is relatively straightforward to determine whether a reaction is mass transport limited or not. The observed reaction rate can be measured in the regime of low conversion, the catalyst particle radius and volume can be estimated by scanning electron microscopy, and the substrate surface concentration can be estimated assuming ideal gas conditions. The most challenging estimation, the effective diffusivity constant, can be determined using one of several experimental techniques, of which we will highlight a few. (1) Diffusion kinetics may be quantified using gas sorption gravimetric methods.[33,34] Assuming that the adsorbent particle has a spherical shape, at low time values t, the transient fraction uptake relates to the effective diffusivity constant as $\frac{Q_t}{Q_{t=\infty}} = \frac{6}{R\sqrt{\pi}}\sqrt{D_e t}$, where Q_t is the quantity of sorbate adsorbed per mass of adsorbent at time t, $Q_{t=\infty}$ is the quantity of sorbate adsorbed per mass of adsorbent at equilibrium, R is the radius of the particle, and D_e is the effective diffusivity constant. This equation generally holds well for transient fraction uptake values of $\frac{Q_t}{Q_{t=\infty}} \leq 0.6$. Significantly, these adsorption measurements can be run on routine sorption instruments. (2) Another related approach involves quantifying diffusion kinetics using changes in spectroscopic observables instead of changes in mass. By performing time-dependent spectroscopic measurements, such as monitoring the time dependence of infrared absorption bands for the sorbates, it is possible to relate the transient fraction uptake of a gas to its diffusivity constant, in a similar fashion to the method described above.[35] (3) Another technique that can be used to calculate diffusivity coefficients is pulsed field gradient solid-state NMR spectroscopy.[36,37] This method relies on the fact that sorbates inside crystals with different orientations with respect to the magnetic field applied will show different NMR signals, which will decay in time with the anisotropic reorientation of molecules inside the asymmetric pores of the adsorbent. The decay of the NMR signal intensity, I, is related to the diffusivity of the molecules inside the pores by the equation: $\frac{I}{I_0} = e^{-bD(\theta)}$, where I and I_0

https://doi.org/10.1021/acs.chemrev.2c00537
Chem. Rev. XXXX, XXX, XXX−XXX

are the current and initial signal intensities respectively, b is a time constant that depends on experimental parameters, and $D(\theta)$ is the diffusivity constant, which can further be deconvoluted into the through-channel and across-channels diffusivity constants. Notably, this third technique measures self-diffusion, or the movement of molecules in the absence of a concentration gradient, while the previous two techniques measure transport diffusion, or the movement of molecules in the presence of a concentration gradient. Other methods to determine if the system is mass transport limited include the Madon−Boudart test, which characterizes the dependence of activity on the concentration of active sites.[38,39]

There are several strategies MOF chemists can employ to transition from a diffusion limited process to a bond-breaking and forming limited process (i.e., $C_{wp} \ll 1$). For example, the particle size can be decreased (decreasing R), the flow rate of reactants can be increased (increasing C_s), or frameworks consisting of 1D channels can be altogether avoided given that single-file diffusion decreases D_e.[40] Other methods for avoiding the diffusion-controlled regime include using frameworks with low acidity and large pores, increasing the external surface area (i.e., decreasing crystal size or introducing mesopores), and using composites of active catalysts with materials in which transport is fast.[41] A recent example where the interplay between particle size and internal diffusion flux has been demonstrated is with the Co_2(dobdc) framework, where modulated solvothermal synthesis can be used to control the aspect ratio of the crystallites. Crystallites with large aspect ratios (long 1D channels) have longer diffusional path lengths, slower diffusion, and are more likely to exhibit mass transfer-limited transport.[42] Modulating the temperature of the reaction can also prevent a reaction from operating under a diffusion-controlled regime. However, both reaction rates and diffusion coefficients have complex temperature dependencies. Reaction rates will likely follow an Arrhenius dependence, while the effective diffusivity constant may follow a polynomial, exponential, or a more complicated temperature dependence, conditional on the diffusion regime.

Although this section focuses exclusively on intracrystalline diffusion, the permeability of gaseous reactants through the pore mouths at the surface of MOF crystallites can also play an important role in modulating reaction kinetics. A more thorough discussion of this process is presented in section 2.6, when discussing surface defects. For additional discussion of diffusion inside MOF catalysts, interested readers are directed to a recent review on the topic.[43]

2.2. Enrichment of Gaseous Reactants in Pores

Similar to solution-based catalysis, the reaction rates of gas−solid reactions are directly corelated, and often proportional, to the concentration of the substrates at the active site. As such, increasing the concentration of gas molecules in the pores of MOFs is essential for facilitating reactivity and catalysis. In transitioning from solution-based to gas-phase catalysis, the concentration of gaseous reactants generally increases. For example, at 298.15 K and 1.01 bar, the solubility of H_2 in n-hexane is only 13% of the bulk concentration of gaseous H_2 (5.45 mmol/L vs 40.9 mmol/L).[44] Better yet, owing to the micro- and mesoporosity of MOFs, enrichment of gaseous reactants in the pores can occur in the form of three main mechanisms: (1) surface adsorption, (2) pore condensation, and (3) oversolubility in confined liquid (Figure 4). Overall, these processes are sometimes referred to as confinement effects.[45−47] Below, we will provide a brief account of the three mechanisms as they occur in porous materials.

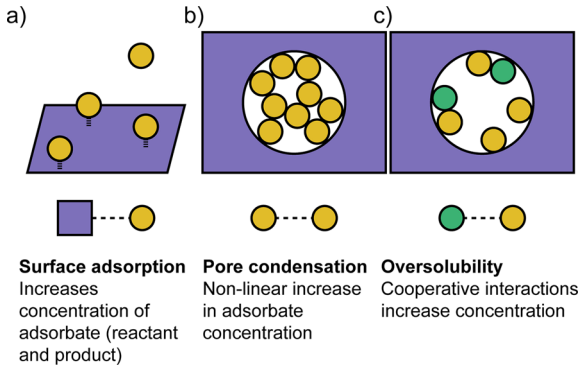

Figure 4. Three dominant interactions of adsorbate molecules in a porous material: (a) interaction with the adsorbent surface, (b) interaction between like adsorbates, which may cause pore condensation above a critical concentration, and (c) interaction between different adsorbates, which may increase the concentration of either adsorbate above the concentration if only one adsorbate were present.

For gas−solid interface reactions, surface adsorption equilibria of both reactants and products greatly influence reaction rates. For sorption in which only a single-layer of gases adsorb to the surface of the porous solid, the coverage is well described by the Langmuir equation, $\theta = \frac{KP}{1+KP}$, where θ is the fractional occupancy of adsorption sites, P is the pressure of the sorbate, and K is the equilibrium constant for the adsorption process.[48] According to this model, at low pressures (i.e., $1 \gg KP$), $\theta \approx KP$ (i.e., the Henry regime). In other words, the extent of adsorption is proportional to the pressure of the sorbate. On the other hand, at high pressures (i.e., $1 \ll KP$), $\theta \approx 1$, and all adsorption sites are occupied. However, this equation assumes that all adsorption sites are identical in nature and that each adsorption site can only accommodate one sorbate molecule. In reality, adsorbent surfaces are rough, present multiple types of adsorption sites, and sorbate molecules often generate multilayers. Explicit calculations of the adsorption sites and interaction strengths with adsorbates may be probed using molecular dynamic simulations. To capture the complexity of surface adsorption processes, several more sophisticated theories have emerged over time.[49]

All things considered, the exposed pore surface can interact strongly with gases and induce the formation of densely packed adsorbate layers far below the saturation pressure. This effect manifests as excess uptake capacity and can be measured by adsorption measurements at pressures and temperatures relevant to the reaction. Here, *excess* uptake is defined as the difference between amount of gas adsorbed (*total* uptake) and amount of gas displaced by the adsorbent. This distinction is particularly relevant at high pressures, a regime under which many gas phase reactions take place, when the *excess* uptake capacity noticeably deviates from the total uptake capacity because the amount of gas displaced by the adsorbent becomes non-negligible.

The interaction strengths between the adsorbate and different chemical moieties within a porous solid affect the degree of adsorption, and thus the overall catalytic rates of a reaction. Derouane and co-workers were early in recognizing the molecular nesting effect in microporous materials; they

https://doi.org/10.1021/acs.chemrev.2c00537
Chem. Rev. XXXX, XXX, XXX−XXX

rationalized the higher pentane cracking activity of smaller-pore zeolites as the result of enhanced adsorption due to matching surface curvature and molecular dimension. In particular, a quantitative relationship between heat of adsorption and catalytic activity was established.[46] Similar arguments have been invoked to explain the enhanced catalytic CO_2 cycloaddition activity of sulfone-functionalized USTC-253 versus EL-MIL-53,[50] although the effect of adsorption has not been quantified in this case. Another example of the adsorption-based enrichment, albeit not strictly a gas phase reaction, can be found in the work of Xiao et al., where they demonstrated that differences in cyclohexane adsorption enthalpies give rise to different alcohol versus ketone selectivity in cyclohexane oxidation reactions.[51]

For mesoporous materials, gases with higher critical temperatures can condense into liquid-like phases within the pores through capillary condensation, the second substrate enrichment mechanism in the pores of MOFs we will consider. Pore condensation can occur only if the temperature is lower than the critical temperature of the confined sorbate, which is always lower than the bulk critical temperature of the sorbate. In fact, the critical temperature of the confined sorbate decreases as the pore size shrinks.[52] Pore condensation can be readily discerned by steep rise in the relevant adsorption isotherm and is sometimes accompanied by hysteresis. The partial pressure at which capillary condensation occurs can be correlated to pore size by the Kelvin equation.[53] Intrapore condensation has been invoked to explain the abrupt improvement in ethylene dimerization catalyst stability above a threshold ethylene pressure in mesoporous Ni-MCM-41.[54,55]

A third mechanism of gas enrichment arises when the liquid-like condensate in mesopores enhances the sorption of a second gas, which is often known as oversolubility. A striking example was reported by Soubeyrand-Lenoir et al., who found that MIL-100(Fe) adsorbs 5 times more CO_2 upon increasing the relative humidity from 3 to 40%.[56] Later that year, Clauzier et al. found that the H_2 uptake was enhanced 1.9-fold in MIL-101(Cr) when 60% of the pores are filled with hexane. This hybrid adsorbent dissolves H_2 42 times more than bulk hexane in terms of volumetric concentration.[57] The same authors later studied the mechanism of oversolubility with grand-canonical Monte Carlo simulations and attributed it to three factors: adsorption at liquid−solid interface, enhanced solubility in confined liquid, and adsorption at gas−liquid interface.[58] Applied to catalysis, oversolubility was first proposed to explain the zeroth-order H_2 dependence of nitrobenzene hydrogenation in mesoporous γ-Al_2O_3.[59,60] More recently, Liu et al. reported enhanced methane oxidation catalytic activity for molecular tricopper complex immobilized onto mesoporous silica nanoparticles. The improvement was attributed to oversolubility of methane and oxygen.[61]

While reactant enrichment in the pores promotes reactivity, the accumulation of reaction products (or other off-pathway side products) in the pores may slow down or fully prohibit further reactivity, or lead to undesired further reactivity. In an experimental setup that admittedly did not involve strictly gas-phase reactivity, the Dincă lab has shown that increasing the pressure of ethylene in the ethylene dimerization reaction increases the formation rate of the desired kinetic product, 1-butene, while decreasing the formation rates of the thermodynamic 2-butene products and limiting the formation of larger C_{6+} oligomers.[62] In the presence of larger amounts of reactant, product accumulation in the pores is minimized, and over-reactivity is prevented. In a more extreme case, the formation and accumulation of large solid products (such as large polymers in the example above) could lead to pore clogging and eventual catalyst deactivation. We note that running gas phase reactions in flow, as opposed to in batch, should lead to less product accumulation in the pores, as the active stream of reactant molecules can help elute product molecules from the pores of the material.

2.3. Solvation by Framework and Sorbate

As discussed in the previous section, the strength of sorbate-framework interactions affects the degree of adsorption. In the context of reactivity, framework interactions directly modulate the energies of substrates, reaction intermediates, and products, as well as any transition states along the reaction trajectory. Framework interactions should lead to substrate binding to promote accumulation of the substrate, but the stabilization should not be as strong as to prevent the reaction from proceeding forward. Similarly, framework interactions should stabilize the bound product to promote the substrate to product transformation but not so strong as to prevent the product from desorbing to allow new substrate molecules to bind to the active site. In fact, as with all catalytic reactions, the ideal MOF catalyst should stabilize the productive transition state most to facilitate the selective transformation to the desired product (Figure 5a). This section will consider sorbate-framework dipolar and dispersive interactions, understood together as solvation interactions. The next section will analyze sorbate framework acid−base interactions.

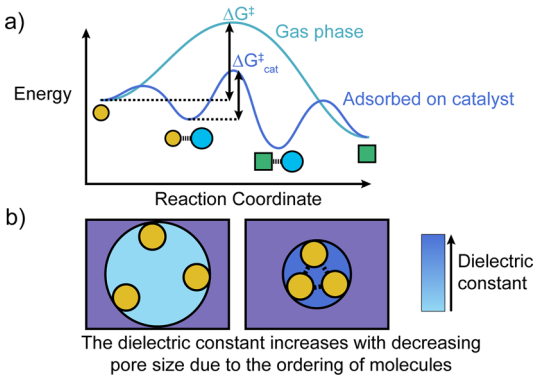

Figure 5. (a) Solvation effects within MOFs greatly alter the energies of species along the reaction coordinate. Ideal MOF catalysts should stabilize the desired transition state most to minimize the activation energy of the reaction. (b) For microporous solids, adsorbate may preferentially orient, which will increase the dielectric constant and provide charge stabilization.[74]

Even though gases provide significantly less stabilization of charged species through solvation than liquids in solution due to the smaller dielectric constants of gases compared to liquids,[63] solid supports in this case exert a strong influence on guest molecules through dipolar and dispersive interactions. In the case of anhydrous zeolite Y exchanged with alkali metals, it was determined that the exposed cation sites render the framework more polar than water, as manifested by the large red-shift of the absorption spectrum for the dye Nile Red. Interestingly, the apparent polarity of the framework is reduced when the sample is exposed to polar solvents and enhanced when exposed to nonpolar solvents.[64,65] In the context of catalysis, Corma and co-workers found that while 1,8-

https://doi.org/10.1021/acs.chemrev.2c00537
Chem. Rev. XXXX, XXX, XXX−XXX

bis(dimethylamino)naphthalene (DMAN) catalyzes Knoevenagel reaction more efficiently in polar solvents, the dependence is much less pronounced if DMAN is grafted onto pure-silica MCM-41. They argued that the higher polarity of the silica support serves to stabilize the transition-state complex, diminishing the role of the solvent and its polarity.[66] In addition to the dipolar interactions, guest molecules can be stabilized through attractive van der Waals interaction. For example, the excellent size- and shape-matching between *para*-xylene and SAPO-34 gives rise to a very high heat of adsorption (ca. 90 kJ/mol).[67] It is worth noting that such dispersive interaction is often factored into heat of adsorption and is sometimes effectively the same as the molecular nesting effect aforementioned. In terms of catalysis, Iglesia and co-workers have observed that the low temperature carbonylation of dimethyl ether is catalyzed by zeolites containing 8-member ring cavities, but not by zeolites with larger pores, which can be explained by a 30 kJ/mol difference in calculated activation energies when considering dispersive stabilization effects.[68] Analogous effects have also been found for mesoporous materials, where the curvature is much smaller. Raja et al. found that when immobilized into mesoporous silica, the stereoselectivity of chiral hydrogenation catalysts are vastly enhanced, and the enhancement decays as pore size increases. They purported that the reason is that a curved support reinforces anisotropic access of substrate toward active site, beyond the effect of the ligand itself.[69]

In cases where pore condensation happens, as discussed in the earlier section, solvation of various species by the intrapore liquid can occur. It should be noted, however, that for smaller mesopores, as is common for MOFs, the properties of intrapore liquid (e.g., dielectric constant) can be significantly different to bulk liquid (Figure 5b). Rieth et al. recently examined the water condensed in MOFs containing open metal sites lining 1D hexagonal channels of 2.2 nm diameter and found that the water molecules bound to metal sites and their immediate H-bond partners are essentially translationally immobile and reorient much more slowly than bulk water molecules.[70] The mobility of the water, they found, increases as it gets closer to the center of the pore, where it is similar to bulk water. The H−Al−β-F zeolite catalyzed ethanol dehydration reaction is first-order in water at low H_2O pressures but third-order at higher H_2O pressures as a result of the different water cluster formed at higher partial pressure.[71]

Catalytic performance of porous solids can be significantly altered by the presence of coadsorbed molecules, even in the absence of capillary condensation. Paolucci et al. observed that at temperatures below 225 °C, the rate of the copper-exchanged chabazite catalyzed reduction of nitric oxide scales quadratically with volumetric copper concentration in the zeolites, which they attributed to a bimetallic oxidation step, where two ammonia-solvated Cu^I species can diffuse away from their lowest-energy ion-paired location and jointly react with O_2 to form $Cu_2O_2(NH_3)_4^{2+}$.[72] Haw and co-workers observed that acetone dimerization on acidic zeolite in flow can only be observed when nitromethane, which solvates the charged transition state and facilitates proton transfer, was co-fed into the gas flow reactor.[73]

2.4. Acidity and Basicity at Gas−Solid Interfaces

Acid−base interactions can similarly stabilize compounds or transition states along the reaction coordinate. Many reviews and accounts have been dedicated to acidity and basicity of solids, some of which specifically concern MOFs.[75−77] Herein, we provide a brief summary of key concepts and methods used to study them. Due to the very limited solvation, the scale of Brønsted acidity and basicity in the gas phase can be vastly different from the scale in solution. Hence, the pK_a and pK_b scales commonly used for acids and bases in solution become inapplicable.[78] Instead, absolute scales, such as proton affinity (for gaseous species), and relative scales from spectroscopic and thermal desorption techniques (for solid surface) are more suitable. As for Lewis acidity and basicity, absolute scales that are commonly used in molecular chemistry, such as fluoride affinity and hydride affinity,[79,80] are intrinsically gas-phase and thus can be applied to gas−solid interfaces readily.

Consider the surface of a simple metal oxide: the coordinatively unsaturated metal (M^{n+}) and oxide (O^{2-}) ions are the origin of surface acidity and basicity.[78] The overall property of the surface depends on the relative strength and abundance of the two and in many cases can be indeed amphoteric. As a general trend,[81] small cations with high charge tend to make acidic metal oxides, such as Nb_2O_5 and MoO_3, whereas large cations with low charge tend to give basic metal oxides, such as Na_2O and MgO. Doping and surface modification of a simple metal oxide with a second element will modify the surface following the same guiding principle of charge-to-radius ratio. Without rigorous high-temperature activation, hydrated metal oxide surfaces also contain −OH groups, which can be either acidic or basic.[78] The same principle applies in the case of zeolites. All-silica zeolites are only weakly acidic due to the presence of silanol groups at defect sites. Similar to doping in metal oxides, substituting Si with Al necessitates an additional cation for charge balance, and in H-Zeolites such cations are H^+. The Al−(OH)−Si thereby created is much more acidic than silanols, and it was found that the acid-catalyzed hexane cracking activity in H-ZSM-5 is solely proportional to Al content.[82] Similar to surface modification, exchanging protons for alkali metal cations eliminates the acidity and cracking activity and indeed makes the zeolite basic.[83]

Experimentally, Brønsted acidity of O−H in zeolites can be measured by infrared spectroscopy, as detailed in the review by Bordiga et al.[84] Briefly, a series of probe molecules with different basicity (e.g., from N_2 to deuterated acetonitrile, CD_3CN) are dosed onto the zeolites and the red-shift of the acidic O−H bands are used to calculate the deprotonation energy. IR spectroscopy with a single adsorbate (often CO) is also useful for obtaining the *relative* strength of the Brønsted acid sites. Other commonly used techniques in zeolites include temperature-programmed desorption (TPD) of basic molecules such as ammonia, calorimetry,[85] and solid-state nuclear magnetic resonance (ssNMR) spectroscopy.[86,87] It should be noted that many of these methods are heavily influenced by confinement effect (i.e., dispersive stabilization) when applied to zeolites[88] and probe both Brønsted and Lewis acidic sites. Lewis acidity, for example, is readily probed by monitoring the IR frequency of adsorbed CO.[78,84] In absence of π-interaction, the Lewis acid forms a nonclassical carbonyl complex and raises the ν(C−O) above the value of free CO (2143 cm^{-1}). Other common methods include CD_3CN-dosed IR, TPD and ssNMR.[78,86,87,89] Lewis and Brønsted basicity are most commonly studied by TPD or IR study with CO_2 as a probe molecule, although the results are often more complicated due to the multitude of surface reactions that can happen.[81,90]

https://doi.org/10.1021/acs.chemrev.2c00537
Chem. Rev. XXXX, XXX, XXX−XXX

2.5. Stabilization of Reactive Intermediates via Site Isolation

Following the catalytic cycle, after diffusion of the substrate through the MOF framework, accumulation in the pores, and binding to the active site, the chemical transformation may occur, often involving high energy reactive intermediates. Common reactive intermediates in organic reactions include carbocations, carbanions, radicals, and carbenes. In metal-catalyzed reactions, they can include species such as metal hydrides, alkyls, aryls, nitrenes, oxos, and nitro/nitritos. Overall, the observation and characterization of such reactive intermediates has become an attractive target in solution-based chemistry because these transient species may offer mechanistic insight. However, unsurprisingly, many attempts at isolating these intermediates result in the isolation of the lowest-energy state in the catalytic cycle, the resting state. A common strategy employed in solution chemistry involves the addition of only a subset of the reagents that, in theory, could generate the reactive intermediate. The hope is that, in the absence of other substrates, this reactive intermediate can then be isolated, or at least observed. However, many times, these intermediates are so reactive that even without substrate they will decompose, be it through intramolecular pathways, bimolecular decomposition in solution, or reaction with solvent. To circumvent these deleterious side-reaction, solution chemists often employ steric bulk to shield the active site of the reactive intermediate and kinetically prevent it from reacting, a strategy which has allowed for the successful isolation of some reactive species.

On the other hand, MOFs provide an attractive alternative platform for the isolation of reactive intermediates owing to site isolation.[91−93] Due to the geometrical arrangement of metal active sites in MOFs, certain decomposition reaction pathways become forbidden. The anchoring of the metal active sites within the MOF framework spatially separates the reactive intermediate site from other active sites, preventing bimolecular decomposition pathways, as well as from the organic linkers of the MOF, preventing intramolecular reactivity (Figure 2d). Moreover, being able to carry out many of the MOF catalyzed reaction at the solid−gas interface (i.e., in the absence of solvent) prevents solvent-related decomposition pathways. As a direct result, highly reactive species can be stabilized within MOFs. While a similar argument can be made for other solid supports, such as frozen glass matrices, one of the many advantages of using MOFs for the isolation and characterization of reactive intermediates is the well-defined geometry within the MOF environment. We note that certain reactions do require the cooperative interaction between two or more active sites. Some of these reactions may not be suitable inside the rigid framework of MOFs. On the other hand, we anticipate that the development and exploration of MOFs with carefully designed active sites, whereby two reactive intermediates can be generated in close proximity to each other, could facilitate cooperative reactivity inside MOF frameworks.

One emblematic example of the usage of site isolation to alter reaction pathways is the work by Zhang et al., who utilized site isolation within Zn-IRMOF-3 to install well-defined single atoms of Au(III).[94] Unlike in homogeneous media, where during the progress of the reaction the gold atoms may accumulate together and form nanoparticles, the gold atoms remain monatomic within the confines of the MOF. The differentiation allows for a clear demonstration that monometallic gold active sites are capable of achieving the desired reactivity for olefin hydrogenation.

In situ spectroscopic and diffraction methods are valuable tools for the characterization of reactive species inside the pores of MOFs.[95−97] For example, vibrational spectroscopies have been used to identify the nature of certain reactive species. Dincă and co-workers studied the stoichiometric nitric oxide disproportionation in Fe-MOF-5 and Cu(I)-ZrTpmC* with diffuse reflectance IR spectroscopy and identified the previously unobserved radical $M-N_2O_2^{\bullet-}$ as a key intermediate.[98,99] Baek et al. used resonance Raman spectroscopy to identify a bis(μ-oxo) dicopper active site capable of selective methane to methanol oxidation using N_2O as an oxidant, within the pores of a postsynthetically modified MOF-808 framework.[100] Using neutron powder diffraction, Bloch et al. determined that O_2 reacts reversibly with Fe_2(dobdc) below 220 K to from a symmetric side-on O_2 ligand (d(O−O) = 1.25(1) Å, intermediate between superoxo and free dioxygen), while the same combination reacts irreversibly at higher temperature to from a slipped side-on peroxo (d(O−O) = 1.6(1) Å).[101] In the IR spectra, the low temperature $Fe-O_2$ adduct has a ν(O−O) at 1129 cm^{-1}, while the room temperature adduct shows a 790 cm^{-1} band, which are again consistent with the assignment of superoxo and peroxo, respectively.[101] Similarly, Dincă and co-workers characterized a $V(III)-O_2$ adduct formed by the gas−solid reaction of dioxygen with V(II) and were able to assign a ν(O−O) at 1013 cm^{-1} to a side-on superoxo species. Anderson et al. went further to characterize the O_2−heme adduct in PCN-224 via single-crystal diffraction and provided the first structural characterization of the elusive five-coordinated end-on ferric superoxo complex.[102]

2.6. Generation and Characterization of Defect Sites

Defects in extended structures such as MOFs can promote or fully inhibit catalysis. For example, the oxidation of CO catalyzed by copper carboxylate-based MOFs, discussed at length in section 3.2.3, only occurs after defects have been introduced in the framework by thermal decarboxylation of the linkers.[19] It is therefore necessary to develop an understanding of both the role of defects and methods to characterize them, in order to identify catalytic active sites, draw structure−function correlations, and inform the rational design of future synthetic targets (Figure 6). However, defects in MOFs, as well as other materials, have proven very difficult to properly characterize.

Given their extended structures, MOFs are inevitably defective.[103−106] Yet, our ability to control and characterize MOF defects lags compared to more mature fields of study,

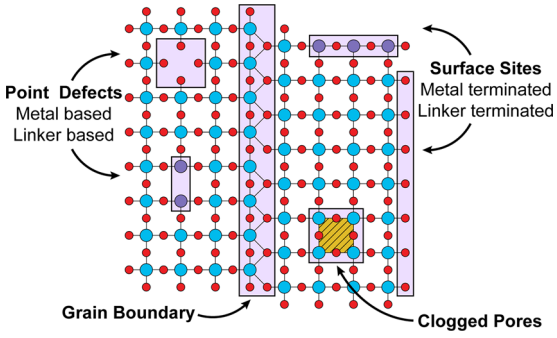

Figure 6. Types of defects present in metal−organic frameworks.

https://doi.org/10.1021/acs.chemrev.2c00537
Chem. Rev. XXXX, XXX, XXX−XXX

such as zeolites. Nevertheless, the robust field of zeolites has provided MOF scientists the knowledge and intuition needed to start defect characterization in MOFs. Notably, three different kinds of defects can be identified in MOFs: point defects, extended defects, and surface defects.

Point defects most often arise from linker, metal, or cluster vacancies, or linker or metal substitution. On one hand, they can be the result of rapid crystallization that does not allow for the equilibration of the system toward the local energetic minimum.[107] On the other hand, adding modulators to slow down crystallizations by competitive binding of either metals or linkers can result in the incorporation of said modulators into the final MOF structure as point defects.[108,109] Sometimes, decomposition of the MOF during catalysis or during the preactivation step can also lead to the introduction of point defects. These defects can be deleterious and completely prohibit catalysis. For example, a possible deactivation pathway includes the deposition of coke in the MOF pores during catalysis, which leads to pore clogging and/or active site blocking. We note that due to the organic linkers of MOFs, these materials cannot be regenerated under oxidative conditions after coke deposition, which might inhibit or prohibit their usage for certain reactions. Conversely, the generation of point defects under catalysis conditions or during the preactivation step can turn on the catalytic activity. This is the case for copper(II) carboxylate-based MOFs which promote the CO oxidation at the Cu(I) defects generated via reductive linker decarboxylation during preactivation.[19] Additionally, the active sites for catalytic reactions may be defect sites and not the SBU sites which one might naively expect. Therefore, it is always necessary to thoroughly characterize MOF catalysts and their defects, both as synthesized and *post operando*, in order to gain a better understanding of the operative reactivity pathway. Techniques to characterize point defects in MOFs include: acid−base titration,[110,111] nitrogen adsorption isotherms,[112−114] water adsorption isotherms,[115] TGA,[112,113,116] IR,[117−119] EPR,[117] XPS,[120] TEM,[112,121] PXRD,[121−123] anomalous X-ray scattering,[122] pair distribution function (PDF) measurements,[122] EXAFS,[120] high resolution neutron scattering,[109] or post-digestion NMR,[113,117,123] HPLC,[112] or ICP-MS.[120] Most of the time, multiple techniques must be used in tandem to appropriately characterize defects.

The second type of defects, extended defects, are the result of imperfections in the crystal structure, and can be one- or two-dimensional. They often result from microcracks in the macroscopic crystals/crystallites, the cocrystallization of different MOF polymorphs with similar energies, or simply from the growth of multiple nearby crystallites, which generates grain boundaries. TEM can often be employed to analyze extended defects.[124] We note, however, that many MOFs may be damaged by the intense electron beam of TEM instruments. Other methods that can be used to probe extended defects in MOFs include atomic force microscopy (AFM)[125] and confocal fluorescence microscopy (CFM).[126,127]

The last type of defects, surface defects, are prevalent on the outside surface of all crystallites and can also be understood as a particular case of extended defects. Close to the outer layer of such crystallites, the approximation of the local structure as ever-repeating unit cells fails and lattice instability is pronounced. On the surface of the crystal, the valencies of the terminal linkers or metal ions are often completed by ill-defined species from the crystallization solution or the environment to generate complex surface layers. These layers can have profound effects on the efficiency of a MOF catalyst, as all substrate molecules have to pass through these surface layers to reach the catalytically active sites. Gas transport models at the surface of nanoscale crystallites (as well as at other interfaces such as extended defects) often consider a thin layer of drastically decreased diffusivity to account for the changes in lattice properties close to the surface.[128,129] Kärger and co-workers studied the transport resistances at the crystal surface, referred to as surface barriers, of Zn(tbip) (tbip = 5-*tert*-butyl isophthalate), a MOF with one-dimensional pores.[130,131] The authors used varied temperature interference microscopy (IFM) and IR microscopy (IRM) measurements to quantify the uptake of gas molecules in the MOF crystallite and calculate the surface permeability and intracrystalline diffusivity for each gas (ethane, propane, *n*-butane) at various temperatures and loadings. This work showed that only 1 in every ∼2000 pore mouths is accessible on the surface of Zn(tbip), the others being blocked, although the exact mechanism of blocking remains unclear. However, the distribution of guest molecules within all one-dimensional pores (despite the vast majority of them being blocked on the crystal surface) suggests that local defects inside the crystal, connecting the 1D pores, are also prevalent. In addition, the authors unexpectedly observed that the ratio of the permeability and diffusivity constants calculated for any given crystal stays invariant with changes in the identity of the gas, gas loading, or diffusion regime, i.e., equilibrium or non-equilibrium conditions. This observation suggests that surface permeation and intracrystalline diffusion in Zn(tbip) are controlled by the same molecular mechanism. Overall, while surface defects are prevalent and greatly impact the diffusion inside the MOF crystallites, their characterization throughout the literature remains wanting.

Defects are prevalent in MOFs and play an important role in understanding catalysis in MOFs. Many point defects have no effect on catalysis, but in some select cases point defects can completely prohibit or, conversely, fully enable the catalytic activity within MOFs, as discussed above. Extended and surface defects, in turn, greatly impact transport within MOFs, hence influencing the rate of catalysis if the reaction is operating under a diffusion-controlled regime. Therefore, a thorough characterization of MOF defects is necessary to understand their catalytic performance. Additionally, the possible introduction of defects during preactivation or under catalytic conditions requires the careful *post operando* characterization of the MOF catalysts. During catalytic reactions, the frameworks may deteriorate, generating defect sites or decomposition products (e.g., metal salts). These products may be the key active catalysts. It is thus critical in all reports on catalysis that there be a comparison between detailed characterizations of the MOF catalyst before and after catalysis. If there is any amount of catalyst deterioration, then one cannot claim that the MOF itself is necessarily the active species without proper experimental evidence. However, defect characterization in MOFs is often non-trivial and, when possible, usually requires multiple techniques used in tandem. Nevertheless, the potential impact of fully understanding the structure of defects within materials is high, and we strongly encourage all MOF catalysis chemists to thoroughly characterize their materials *pre* and *post operando*.

https://doi.org/10.1021/acs.chemrev.2c00537
Chem. Rev. XXXX, XXX, XXX−XXX

Table 1. Comparison of Olefin Hydrogenation MOF Catalysts

MOF	gas	reaction conditions	catalyst stability	TOF	ref
Ir pincer@NU-1000	ethene	tubular flow reactor, 1:1 ethene/H_2, 80 mL/min	4% loss in activity after 24 h, no *post operando* characterization	0.321 s^{-1} at 50 °C/1 bar, 0.135 s^{1} at 23 °C/0.5 bar	133
$Ir(C_2H_4)_2$@UiO-66	ethene	tubular plug flow reactor, 298 K, 1 bar (0.1/0.2/0.7 = C_2H_4, H_2, He), 100 mL(NTP)/min	activity decreases with time, CO dosed IR spectra after catalysis reveals little change in the Ir geometry	0.00035−0.017 s^{-1}, some dimerization occurs	134,135
$Ir(CO)_2$@R-UiO-66	ethene	once through tubular plug flow reactor, 313 K, 1 atm 100 mL(NTP)/min, 0.2/0.2/0.6 = C_2H_4/H_2/He	activity decreases with time on stream, in situ IR indicates liberation of CO, no structural characterization performed *post operando*	0.0025 s^{-1}	143
$Ir(C_2H_4)_2$@UiO-67	ethene	tubular plug flow reactor, 298 K, 1 bar (0.1/0.2/0.7 = C_2H_4, H_2, He), 100 mL(NTP)/min	activity decreases with time, no *post operando* characterization	0.012 s^{-1}, some dimerization occurs	134
$Ir(C_2H_4)_2$@UiO-67	ethene	once-through isothermal plug-flow reactor, 1 bar (0.05/0.05/0.9 = C_2H_4, H_2, He)		0.012 s^{-1}	136
Ir_4@UiO-67	ethene	once-through isothermal plug-flow reactor, 1 bar (0.05/0.05/0.9 = C_2H_4, H_2, He), preactivated with H_2 at 353 K, 1 h		0.027 s^{-1}	136
Ir@NU-1000	ethene	tubular plug flow reactor, 298 K, 1 bar (0.1/0.2/0.7 = C_2H_4, H_2, He), 100 mL(NTP)/min	CO dosed IR spectra after catalysis reveals little change in the Ir geometry, lifetime of catalyst not determined	0.010 s^{-1}, some dimerization occurs	135
Ni_xO_y@UiO-66	ethene	packed-bed flow reactor, 373 K, 1.5 bar, 1:2 = C_2H_4/H_2	regeneration with H_2 at 200 °C for 2 h restores some activity. SEM images of particles after catalysis demonstrate some morphological change and 77 K N_2 capacity changes	0.04−0.15 s^{-1} depending on Ni_xO_y loading	137
Ni@NU-1000	ethene	pretreated with 3% H_2/Ar at 200 °C for 5 h, flow reactor, 473 K, 200 mL/min, 1:2:3 = C_2H_4/H_2/Ar	active for >2 wk time on stream with slight decrease in activity, no change in structure after catalysis (PXRD, EXAFS)	0.9 s^{-1}	138
Ni_xO_y@R-NU-1000 (R = NH_2, OCH_3, CH_3, H, F, NO_2)	ethene	pretreated with 5% H_2/Ar at 200 °C for 2 h, 1:2 = C_2H_4/H_2, 200 mL/min, 373 K	no loss in crystallinity postcatalysis (PXRD), decrease in 77 K N_2 capacity	0.0002−0.0052 s^{-1}	139
Rh@UiO-67	ethene	once through flow reactor, 298 K, 1 bar, 0.05/0.05/0.9 = C_2H_4/H_2/He, 100 mL(NTP)/min	no *post operando* characterization	0.036 s^{-1}	140
Rh(I)BF4@Mn(bdpdmpm)	ethene	batch reactor, 1.2/0.8 = C_2H_4/H_2, 319 K, 2 bar	nanoparticle formation if excess H_2 is used, some activity loss after 5 cycles	$TOF^{90\%}$ = 0.018 s^{-1}	141
IRMOF-3−SI-Au	1,3-butadiene	fixed-bed quartz reactor, 2.0 vol% 1,3-butadiene in H_2 (13 mL/min) and Ar (28 mL/min), 1 atm, 403 K	stable on stream for 6 h and 2 cycles, no *post operando* characterization	0.15 s^{-1}, ∼40% 1-butene, ∼43% *E*-2-butene, ∼8% *Z*-2-butene, 3% butane	94
Ir(I)@MIL-101(Cr)-SO_3	but-1-ene	batch reaction: ∼1/1: C_4H_8:H_2, 298 K	no loss in activity after 2 cycles, no *post operando* characterization	0.075 s^{-1}	142
Rh-HKUST-1	propene	packed bed tubular flow reactor, 0.05:0.2:0.75 = C_3H_6/H_2/He, 100 sccm	no change in Rh by XPS or crystallinity (PXRD) after catalysis	0.017 s^{-1} CuRh(33%)BTC 298 K, 0.008 s^{-1} CuRh(18%)BTC 298 K	144
Pt (5 wt %) on alumina (reference)	ethene			35 s^{-1}	138

3. EXAMPLES OF GAS−SOLID REACTIONS IN MOFS

Here, we survey and discuss several key gas−solid small molecule transformations, spanning reductive reactions (olefin hydrogenation, alkyne semihydrogenation, selective catalytic reduction), oxidative reactions (oxygenation of hydrocarbons, oxidative dehydrogenation, carbon monoxide oxidation), and C−C bond forming reactions (olefin dimerization and polymerization, carbonylation, isomerization reactions). Broadly speaking, we find two dominant strategies for the design of MOF catalysts. The first method is best described as a traditional heterogeneous catalysis approach, whereby the secondary building units are considered as a highly dispersed and well-defined mimic of heterogeneous metal oxides. The second method is a molecular complex approach, whereby the frameworks are considered inert hosts for molecularly defined active species. In particular, we place emphasis on frameworks hosting well-defined molecular active species.

3.1. Reductive Reactions

3.1.1. Olefin Hydrogenation. The hydrogenation of ethylene to ethane has served as a model gas−solid reaction to probe the behavior of porous solids under reductive catalytic conditions (Table 1). The reaction $C_2H_4 + H_2 \rightarrow C_2H_6$ has a negative $\Delta G°$ of −25 kcal/mol and remains thermodynamically favorable below ∼1000 °C.[132] MOF catalysts that have been shown to promote this reaction typically consist of catalytically inert frameworks that have postsynthetically installed active metal sites. Predominantly, the metals of choice are noble metals, such as iridium, rhodium, gold, and palladium, as well as nickel. These metals are known to form stable hydride and/or alkyl species, key intermediates in the hydrogenation reaction, and undergo oxidative addition and reductive elimination reactions toward H−H and C−H σ bonds, key elemental steps. The frameworks typically used are considered inert: Zr-carboxylate frameworks, such as NU-1000, UiO-66, and UiO-67 (e.g., Ir,[133−136] Ni,[137−139] and Rh[140]), known for their high thermal and chemical stability.

Although one of the key features for performing catalysis within MOFs is the well-defined active sites, Peralta et al. have demonstrated that during the catalytic cycle the active site can degrade and form other species.[141] Rh(I) can be incorporated into the dipyrazole binding pocket of the framework Mn(bcpdmpm) (bcpdmpm^{2-} = bis(4-carboxyphenyl-3,5-dimethyl-pyrazol-1-yl)methane) whereby the metalated framework is crystallographically well-defined (Figure 7). This resulting framework is active for the hydrogenation of ethylene, with the highest activity being demonstrated for a bis(ethylene) bound Rh(I) with a weakly coordinating BF_4^- anion in the presence of an excess of ethylene. The MOF-supported $[Rh(ethylene)_2]BF_4$ species showed full conversion of H_2 within 25 min and a turnover frequency (TOF) of 64 h^{-1} in a batch reactor. The TOF remained high on subsequent cycles (44 h^{-1} for cycle 5), indicating a long lifetime of the catalyst. If an excess of hydrogen is present, however, then the Rh(I) is reduced to Rh(0) nanoparticles, which are initially active for ethylene hydrogenation (TOF = 32 h^{-1} for the first cycle). However, the turnover frequency quickly diminishes after multiple cycles (TOF = 9 h^{-1} for the second cycle). Moreover, based on the system's ability to engage in C−H bond oxidative addition at the Rh(I) center, the system also acts as a good catalyst for the isomerization of 1-butene to 2-butene, discussed more in section 3.3.2.

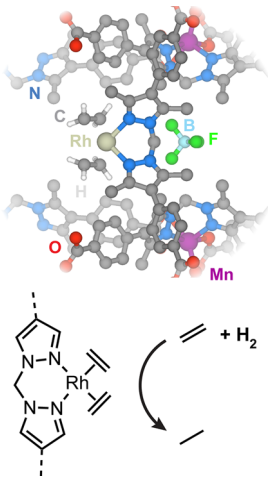

Figure 7. Metalloligand centered Rh(I) incorporated into Mn(bcpdmpm) catalyzes the hydrogenation of ethylene.[141]

Zhang et al. investigated the hydrogenation of 1,3-butadiene employing a gold-incorporated framework.[94] The postsynthetic installation of Au(III) into Zn-IRMOF-3 results in a unique system in which gold atoms are site isolated, preventing the formation of gold nanoparticles which often takes place in solution. Taking advantage of the site isolated, monometallic active sites, the study demonstrated the ability of single gold atoms to catalyze the hydrogenation reaction. It was found that the catalyst was quite active for the hydrogenation of 1,3-butadiene, resulting in a conversion of 96% with selectivity for 1-butene and *E*-2-butene over *Z*-2-butene and *n*-butane, when the H_2:1,3-butadiene ratio used was 1:49. However, no *post operando* characterization (such as PXRD or TEM) has ruled out the possibility of gold aggregation. We note that for the other catalytic cycle that the authors present (three component coupling), the *post operando* PXRD does not scan to a value of 2θ that is sufficiently high to allow potential observation of gold metal. Under identical reaction conditions but using the nongold-incorporated framework, the 1,3-butadiene conversion was <1%. Importantly, this study confirms the ability of single-site Au(III) atoms to catalyze the hydrogenation of π bonds.

It has recently been demonstrated that Crabtree's catalyst, $[Ir(cod)(PCy_3)(py)]^+$, can be appended to a framework with preserved catalytic activity toward the hydrogenation of 1-butene.[142] Grigoropoulos et al. demonstrated that postsynthetic cation exchange of sodium for the Ir(I) species in MIL-101(Cr)-SO_3Na resulted in 7% exchange (compared to a theoretical space filling limit of 9%). The exchanged framework exhibits a roughly 6-fold increase in the TON per Ir site compared to that of finely ground $[Ir(cod)(PCy_3)(py)][PF_6]$, which was attributed to the porosity of the MOF framework and the higher number of exposed active sites. It was also demonstrated that the system is competent for the hydrogenation of other various alkenes, including oct-1-ene, 3-methylhex-1-ene, 2-methylhex-1-ene, cyclohexene, as well as several alkenes bearing alcohol functional groups.

Babucci et al. have taken advantage of the modularity of MOFs to further study the correlation between the electron density on Ir single-atom active sites and ethylene hydrogenation rates.[143] $Ir(CO)_2(acac)$ (acac = acetylacetonato) was chemisorbed to the Zr secondary building units of a series of isoreticular UiO-66-type frameworks, forming $Ir(CO)_2$ species

https://doi.org/10.1021/acs.chemrev.2c00537
Chem. Rev. XXXX, XXX, XXX−XXX

Table 2. Comparison of Semihydrogenation MOF Catalysts

MOF	gas	reaction conditions	catalyst stability	activity	selectivity	ref
$[Fe^{III}(H_2O)_6][Fe_2{}^{III}(\mu\text{-}O)_2(H_2O)_6]_{1/2}\{Ni^{II}{}_4[Cu^{II}{}_2(Me_3mpba)_2]_3\}$	acetylene	1.2% C_2H_2 in C_2H_4 (1 mL/min, 2 bar) and H_2 92 mL/min, 4 bar), GHSV = 4000 h^{-1}	minor structural changes after catalysis (PXRD) and UV−vis remains similar	<10 ppm acetylene in product stream	ethane concentration increases with time on stream at 423 K from 6% to 14%, at 373 K, ethane concentration decreases from 18% to 12%	149
Ru_1@ZIF-8	acetylene	pretreated 5% H_2/Ar 400 °C 1 h, 0.005/0.05/0.5/0.445 = $C_2H_2/H_2/C_2H_4$/He, 40 mL/min, 200 °C	minor structural changes after catalysis (PXRD). HAADF-STEM EDS and AC HAADF-STEM images do not rule out some amount of Ru aggregation	12.5 mol/mol h	51% ethylene	150
Ru_3@ZIF-8	acetylene	pretreated 5% H_2/Ar 400 °C 1 h, 0.005/0.05/0.5/0.445 = $C_2H_2/H_2/C_2H_4$/He, 40 mL/min, 200 °C	minor structural changes after catalysis (PXRD), HAADF-STEM EDS and AC HAADF-STEM images do not rule out some amount of Ru aggregation	603.6 mol/mol h	84% ethylene	150
RhGa(py_3tren)@NU-1000	propyne	fixed bed reactor, 50−250 °C, 1−7.5 atm. 2% C_3H_4/Ar and 5% H_2/Ar or 100% H^2, 15 mL/min	5 cycles with no significant loss in activity/selectivity, EAXFS/XANES indicates no recomposition of RhGa moiety, HAADF-STEM suggests no metal aggregation, NMR and ICP-AES indicate no metal leaching, however 10% decrease in Ga after 5 cycles, crystallinity preserved (PXRD), some loss in 77 K N_2 capacity	TOF = 3.1 min^{-1}, 82% yield	88% propene	151
Rh(C_2H_4)(κ^2-H_3py_3tren)@NU-1000	propyne	fixed bed reactor. 50−250 °C, 1−7.5 atm, 2% C_3H_4/Ar and 5%H_2/Ar or 100% H_2, 15 mL/min		TOF = 3.6 $min^{-1,}$ >99% yield	>99% propane	151

https://doi.org/10.1021/acs.chemrev.2c00537
Chem. Rev. XXXX, XXX, XXX−XXX

supported by two additional O atoms belonging to the Zr_6O_8 SBUs. While the $[Zr_6O_8]Ir(CO)_2$ species was found to be inactive toward ethylene hydrogenation, catalytically active $[Zr_6O_8]Ir(CO)$(ethylene) was generated by flowing ethylene through the pores of the MOF at 40 °C for 1 h. The electron density of the Ir sites was modified by the usage of different carboxylate linkers and modulators during the MOF synthesis. Using a combination of infrared spectroscopy (probing the symmetric and antisymmetric ν(CO) modes) and XAS, the study concluded that Ir centers with less electron density were more active hydrogenation catalysts. In particular, the TOF, calculated at steady-state under low conversions (<5%), increased 7-fold upon changing the modulator used during the MOF synthesis from benzoic acid to trifluoroacetic acid. This work highlights the opportunity to perform structure−function studies of MOF catalysts by systematically varying the secondary coordination sphere.

Postsynthetic metal exchange of Rh(III) into HKUST-1 ($Cu_3(BTC)_2$, BTC = 1,3,5-benzentricarboxylate), with subsequent reduction to Rh(II), yields a framework competent for the room temperature hydrogenation of propylene to propane.[144] This framework is the first example of a MOF bearing Rh^{2+} in the SBU. Similar isoreticular structures of $M_xM'_{3-x}(BTC)_2$, including the all Cu, all Ni, mixed Cu−Ru, mixed Cu−Co, mixed Cu−Ir, and mixed Cu−Ni, are all reported to be relatively inactive for propylene hydrogenation. The Rh system appears remarkably stable, with no significant changes to the crystallinity (as monitored by PXRD) or chemical identities (as monitored by XPS) after catalysis. In this example, computational studies suggest that the carboxylate anion of the linker dissociates from the Rh(II) site to generate a Lewis acid−base pair, which, in turn, heterolytically splits H_2 during the hydrogenation reaction.

The majority of MOF-based olefin hydrogenation catalysts function by the incorporation of catalytically active metals into a framework, simply heterogenizing previously known molecular catalysts. As discussed previously, this strategy results in many advantages, including the ability to carry out the reaction in flow and the increased access of the gaseous reactants to the active sites due to the framework's porosity. However, this strategy also gives rise to low active metal number densities. We hypothesize that frameworks in which the catalytically active metals are also the structural metals, such that every metal of the framework is competent for catalysis, could result in even higher activities of the catalyst. It is important to note that a key design criterion for such a framework would require the SBU metals to have at least one open coordination site (either in equilibrium or fluctional). We note that MOFs with single-metal SBUs tend to be less stable than those with multinuclear SBUs. Targeting the latter becomes an important consideration for those considering practical applications.

3.1.2. Semihydrogenation. The semihydrogenation, or selective hydrogenation, of acetylene to produce ethylene ($\Delta G°$ = −33.6 kcal/mol) is an important industrial process that purifies the ethylene feed for polyethylene production (Table 2). Ethylene produced from cracking contains about 1% acetylene, which needs to be reduced to <5 ppm to avoid poisoning the polymerization catalyst. For this purpose, the semihydrogenation catalyst must selectively hydrogenate acetylene in the presence of ethylene without significant production of ethane.[145−147] Supported Pd catalysts are currently employed industrially, and effort is devoted to searching for a cheaper and more earth-abundant catalyst.[148] Here, we discuss three examples of MOF-catalyzed alkyne semihydrogenation. The use of well-defined active sites in MOFs allows for mechanistic studies, which would otherwise be significantly more challenging to interpret. Moreover, the use of MOFs allows for the generation of particularly active metal sites that do not undergo bimolecular decomposition, which might otherwise occur in homogeneous media.

Inspired by the selective hydrogenation reaction catalyzed by iron oxides, Tejeda-Serrano et al. introduced mono- and dinuclear Fe(III)-aqua complexes into the large channels of the anionic framework, $\{Ni_4[Cu_2(Me_3mpba)_2]_3\}^{4-}$ (Me_3mpba^{4-} = 2,4,6-trimethyl-1,3-phenylenebis(oxamate)) through aqueous cation exchange.[149] At 150 °C, the MOF can reduce the acetylene level from 1.2% to less than 10 ppm in a mixture of 2 bar ethylene and 4 bar hydrogen in flow (gas hourly space velocity (GHSV) = 4000 h^{-1}), similar to industrially relevant reaction conditions for acetylene hydrogenation. The initial selectivity for ethane, the undesired product, is low (<10%) but it gradually increases, which suggests degradation of the selective active site. The authors hypothesized that isolated $Fe^{III}(H_2O)_6$ species hosted in the pores of the anionic framework are the catalytic active sites and showed that the material is competent for H−H bond breaking in the absence of substrate by H_2/D_2 scrambling experiments.

Ji et al. demonstrated the ability of atomically dispersed triatomic Ru_3 clusters anchored on ZIF-8 to catalyze the selective hydrogenation of acetylene to ethylene.[150] The Ru_3 units were generated by loading $Ru_3(CO)_{12}$ into the pores of ZIF-8 during synthesis, followed by CO removal via H_2 treatment at 400 °C. The encapsulated Ru_3 units were proposed to retain their trinuclear arrangement (rather than agglomerating into nanoparticles) based on extended X-ray absorption fine structure (EXAFS) and aberration-corrected high-angle annular-dark-field scanning transmission electron microscopy (AC HAADF-STEM). The resulting catalyst (0.032 wt % Ru) was found to be highly active (603.6 (mol C_2H_2)·(mol Ru)$^{-1}$·h^{-1}) and highly selective for ethylene (84%) at 200 °C. DFT calculations suggest that the triatomic Ru_3 cluster can oxidatively add both acetylene and H_2, facilitating the two C−H bond formation processes via two reductive elimination steps.

Following the path of heterogenizing molecular catalysts, Lu and co-workers grafted bimetallic py_3trenGaRhX (py_3tren^{3-} = $[N(CH_2CH_2N(o\text{-}C_5H_4N))_3]^{3-}$, X = PhO or Me) onto the Zr_6 node of NU-1000.[151] Inductively coupled plasma (ICP) metal content analysis and ^1H NMR clearly established the stoichiometry to be one py_3trenGaRh per Zr_6 cluster. They also ascertained that the Rh−Ga unit remained intact after grafting through EXAFS analysis and pair distribution function (PDF) study. The grafted MOF can catalyze the selective semihydrogenation of propyne with 88% selectivity for propylene (200 °C, excess H_2, flow) (Figure 8). The catalyst remained active for over 10 h, although the selectivity dropped from 88.7% to 64.7%. Importantly, they found that the ungrafted catalyst is inactive in solution due to the formation of insoluble degradation products likely containing Rh(μ-H)Rh units. Notably, the computationally determined reaction mechanism invokes the heterolytic splitting of H_2 by the Rh(I)-pyridine couple acting as a Lewis acid−base pair, in agreement with isotope labeling experiments. It has been suggested that the Lewis acidic Ga atom serves to decrease the

https://doi.org/10.1021/acs.chemrev.2c00537
Chem. Rev. XXXX, XXX, XXX−XXX

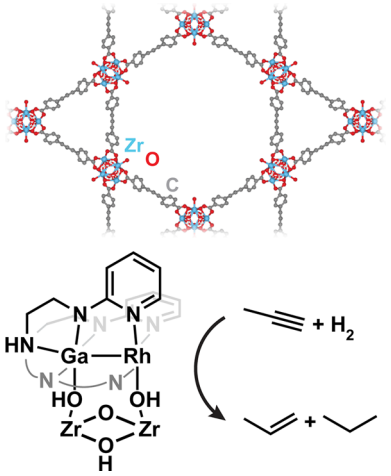

Figure 8. Rh(I)-Ga bimetallic motifs grafted onto NU-1000 catalyze the semihydrogenation of propyne.[151]

electron density at the Rh(I) site, facilitating the Lewis acid−base activation of H_2.

3.1.3. Selective Catalytic Reduction. Nitrogen oxides, NO_x, are highly regulated atmosphere pollutants often found at the output of diesel engines.[152] Methods to mitigate NO_x postcombustion emissions include selective reduction to dinitrogen gas, as well as NO_x storage. The selective reduction reaction can be run either noncatalytically (i.e., combustion) or catalytically, known as selective catalytic reduction (SCR). The primary reaction in the process is $NO + NH_3 + {}^1/_4O_2 \rightarrow N_2 + {}^3/_2H_2O$, which is energetically downhill with a change in free energy of $\Delta G° = -99$ kcal/mol.[132] Alternatively, urea can be used as the reductant instead of ammonia. Additionally, the reaction can also reduce mixtures of NO and NO_2 in the so-called fast SCR reaction.[152] Typical catalysts are composed of metal oxides, such as V_2O_5 and CeO_2, which are also active when embedded within MOFs.[153,154] When developing new SCR catalysts, one must address the issues of catalyst poisoning and preventing solid salt formation.[155] The benefit of MOF-based SCR catalysts lies in the higher specific surface area, which can increase activity, as well as chemical tunability to promote the desired reaction over detrimental side reactivity and to lower the temperature at which the reaction can be run (preventing coke formation and surface passivation, allowing the catalyst to be moved downstream of desulfurization and particle removal scrubbers) (Table 3).[156] A dedicated account of the use of MOFs for SCR was previously published by Liu et al.[155] In this section, we will highlight a few key studies and elaborate on design principles. In particular, we will focus on results with MIL-100 and MOF-74. We note that if there is a possibility that a SCF MOF catalyst can decompose into a catalytically active metal oxide, then the catalysts must have thorough *post operando* characterization to rule out a decomposed metal oxide active catalyst. We find that many of the MOF SCR catalysts are insufficiently characterized.

The first use of a MOF system for SCR was with Fe-MIL-100.[157] While the conventional V_2O_5−WO_3/TiO_2 heterogeneous catalyst is only active above 300 °C, it was demonstrated that Fe-MIL-100 achieves above 97% conversion between 240 and 300 °C and 100% selectivity for N_2 between 100 and 260 °C (measured in flow with 500 ppm of NO, 500 ppm of NH_3, 4% O_2, N_2 balance, gas hourly space velocity (GHSV) of 30000 h^{-1}). At higher temperatures, the framework undergoes irreversible decomposition concurrent with mass loss and loss of crystallinity. The system also tolerates both SO_2 and H_2O, with only a decrease to 90% conversion upon introduction of 500 ppm of SO_2 and 5% H_2O, with an increase in conversion after the supply of SO_2 and H_2O was terminated. The authors measured in situ DRIFT spectra and proposed two possible mechanisms, including a Langmuir−Hinshelwood type mechanism by which NO is oxidized to NO_2 with Fe^{3+} as an oxidant, which can subsequently react with adsorbed NH_4^+ to form N_2 and H_2O, and an Eley−Rideal type mechanism by which oxidative dehydrogenation of NH_3 to a transient NH_2 species is followed by reaction with NO to form the products.

Based upon the success of Fe-MIL-100 as an SCR catalyst, as well as high activity for mixed metal Fe−Mn oxide catalysts, the mixed metal (Fe,Mn)-MIL-100 frameworks were probed.[158] In this study, monometallic Fe-MIL-100 only displayed up to 78% conversion, while the mixed-metal (Fe,Mn)-MIL-100 (Fe:Mn = 4:1) framework surpassed 96% conversion (measured in flow with 500 ppm of NO, 500 ppm of NH_3, 5% O_2, N_2 balance, GHSV of 15000 h^{-1}). The operating temperatures of maximum conversion for both (Fe,Mn)-MIL-100 and Fe-MIL-100 is between 250 and 300 °C. Despite the disparity between activity of Fe-MIL-100 across the two studies, it is clear that the presence of a second metal improves activity.

Density functional theory (DFT) calculations at the PBE level were used to probe the mechanism for SCR on Fe-MIL-100 and suggested an Eley−Rideal mechanism.[159] The authors put forward two catalytic cycles with a single iron atom as the active site: the first generates equivalents of NO_2 from O_2 and NO, while the second converts NH_3, NO_2, and NO into H_2O and N_2. Here, the rate limiting step is the reaction of iron-bound NO_2 with NH_4^+ to form iron-bound nitrosamine and an equivalent of H_2O.

Recently, it has been demonstrated that both Mn-MOF-74 and Co-MOF-74 can catalyze SCR.[156] Both frameworks display maximal activity between 200 and 240 °C, with that for Mn-MOF-74 reaching 99% conversion, and nearly 100% selectivity for N_2 (measured in flow with 1000 ppm of NO, 1000 ppm of NH_3, 2% O_2, Ar balance, GHSV of 50000 h^{-1}). Above this temperature, both frameworks decompose, forming metal oxides. In the presence of 100 ppm of SO_2 and 5% H_2O, activity for both frameworks decreases but is mostly restored upon halting the flow of the poisons. It was subsequently demonstrated that Cu-MOF-74 is also active for catalysis, reaching 97.8% conversion and 100% selectivity for N_2 at 230 °C (1000 ppm of NO, 1000 ppm of NH_3, 2% O_2, Ar balance, GHSV of 50000 h^{-1}).[160] Computational studies at the DFT level have considered the effect of point defects (oxygen atom vacancies) on the binding energy of NH_3, NO, O_2, and NO_2 and found a substantial decrease in binding energies.[161] The study suggests that the lower binding energies of defective frameworks allows for the fast desorption of oxidized products, improving reaction efficiency by increasing turnover frequencies.

3.2. Oxidative Reactions

3.2.1. Oxygenation of Hydrocarbons. Natural gas is composed primarily of methane (70−90%) and other small gaseous alkanes (i.e., ethane, propane, and butane) and is extracted in large quantities across the world to be used as an energy source for heat generation and transportation as an alternative to petroleum. Natural gas therefore plays an

https://doi.org/10.1021/acs.chemrev.2c00537
Chem. Rev. XXXX, XXX, XXX−XXX

Table 3. Comparison of Selective Catalytic Reduction MOF Catalysts

MOF	reaction conditions	catalyst stability	max conversion	ref
$(Ce_{0.1}Zr_{0.9})$-CAU-24	500 ppm of NO, 500 ppm of NH_3, 10% O_2, N_2 balance. total flow rate = 30 mL/min, GHSV = 9000 h^{-1}	no missing linker defects based on TG analysis, large decrease in crystallinity after catalysis (PXRD)	~65% (~275 °C)	153
Ce-UiO-66	500 ppm of NO, 500 ppm of NH_3, 10% O_2, N_2 balance, total flow rate = 30 mL/min, GHSV = 9000 h^{-1}	the MOF contains missing linker defects, large decrease in crystallinity after catalysis (PXRD)	~80% (~225 °C)	153
MnCe-UiO-67 (solvothermal synthesis with Mn, Ce, Zr)	500 ppm of NO, 500 ppm of NH_3, 5% O_2, N_2 balance, total flow rate = 450 mL/min, GHSV = 45,000 h^{-1}	crystallinity retained after catalysis at 200 °C [decomposed samples are also competent catalysts]	<20% (200−300 °C)	154
MnCe@UiO-67 (postsynthetic doping of metals)	500 ppm of NO, 500 ppm of NH_3, 5% O_2, N_2 balance. total flow rate = 450 mL/min, GHSV = 45,000 h^{-1}	[decomposed samples are also competent catalysts]	98% (200−300 °C)	154
Mn-MOF-74	1000 ppm of NO, 1000 ppm of NH_3, 2% O_2, Ar balance. total flow rate = 100 mL/min, GHSV = 50,000 h^{-1}	decomposition to Mn_3O_4 at higher temperatures, activity fairly consistent across 3 cycles	99% (220 °C)	156
Co-MOF-74	1000 ppm of NO, 1000 ppm of NH_3, 2% O_2, Ar balance, total flow rate = 100 mL/min, GHSV = 50,000 h^{-1}	decomposition to Co_3O_4 at higher temperatures, activity fairly consistent across 3 cycles	70% (210 °C)	156
Cu-MOF-74	1000 ppm of NO, 1000 ppm of NH_3, 2% O_2, Ar balance, total flow rate = 100 mL/min, GHSV = 50,000 h^{-1}	no *post operando* characterization	97.8% (230 °C)	160
Fe-MIL-101	500 ppm of NO, 500 ppm of NH_3, 4% O_2, N_2 balance. total flow rate = 315 mL/min, GHSV = 30,000 h^{-1}	crystallinity retained after catalysis, decomposition to Fe_2O_3 occurs at 325 °C, active for >20 h on stream.	97% (245−300 °C)	157
Fe-MIL-101	500 ppm of NO, 500 ppm of NH_3, 5% O_2, N_2 balance, total flow rate = 100 mL/min, GHSV = 15,000 h^{-1}	active for >5 h on stream, no *post operando* structural characterization	78% (300 °C)	158
Mn-MIL-101	500 ppm of NO, 500 ppm of NH_3, 5% O_2, N_2 balance. total flow rate = 100 mL/min, mL/min. GHSV = 15,000 h^{-1},	active for >5 h on stream, no *post operando* structural characterization	53% (240 °C)	158
(Fe,Mn)-MIL-101	500 ppm of NO, 500 ppm of NH_3, 5% O_2, N_2 balance, total flow rate = 100 GHSV = 15,000 h^{-1}	active for >5 h on stream, no *post operando* structural characterization	96% (260 °C)	158
V_2O_5−WO_3/TiO_2 (reference)	500 ppm of NO, 500 ppm of NH_3, 4% O_2, N_2 balance. total flow rate = 315 mL/min, GHSV = 30,000 h^{-1}		51−90% (245−300 °C), >90% (325−375 °C)	157

https://doi.org/10.1021/acs.chemrev.2c00537
Chem. Rev. XXXX, XXX, XXX−XXX

Table 4. Comparison of Hydrocarbon Oxygenation MOF Catalysts

MOF	hydrocarbon	oxidant	reaction conditions	catalyst stability	activity	ref
$(Fe_{0.1}Mg_{1.9})$-MOF-74	ethane	N_2O	packed bed flow reactor: 20 mL/min (2:5:13 = N_2O:C_2H_6:Ar) 75 °C; batch reactor: 1.5 bar N_2O, 7.5 bar C_2H_6, 75 °C	crystallinity retained after exposure to N_2O/ethane; Fe-hydroxide or Fe-alkoxide species terminate catalysis	flow: 9.5:1 ethanol:acetaldehyde; 60% yield (based on Fe); batch: 25:1 ethanol:acetaldehyde, 1.6 turnovers/Fe	165
Fe-MIL-100	methane	N_2O	1.5 kPa CH_4, 2.6 kPa N_2O, 2.9 kPa Ar, He balance, total flow rate = 65 mL/mol	crystallinity declines and porosity is slightly decremented after 5 cycles	18:1 methanol:$CO_2$34% yield methanol at 180 °C (based on Fe)	167
MOF-808-Bzz-Cu	methane	N_2O	(1) He (30 sccm) 150 °C, 1 h (2) 3% N_2O/He (30 sccm) 150 °C, 2 h (3) CH_4 (30 sccm) 1 h (4) He (50 sccm) 1 h (5) 5% steam/He (30 sccm)	large decrease in activity during cycling, possibly due to strongly bound water, crystallinity is retained after reactions	~0.023 mol(MeOH)/mol(Cu) = ~110 μmol(MeOH)/g(cat)	100
Cu-NU-1000 (ALD)	methane	O_2	(1) O_2 16 mL/min, 200 °C, 3 h (2) CH_4:He = 90:10, 16 mL/min, 150 °C, 3 h (3) 50:50 or 10:90 = H_2O:He, 20 mL/min, 2 h, 135 °C	decrease in activity during cycling, crystallinity is retained after reactions	17.7:2.0:24.2 μmol/g(cat) = MeOH:dimethyl ether:CO_2 (first cycle)	168
Cu-NU-1000 (aq)	methane	O_2	(1) O_2 16 mL/min, 200 °C (2) CH_4, 16 mL/min, 150 or 200 °C, 3 h (3) 10:90 = H_2O:He, 20 mL/min, <3 h, 135 °C	mild decrease in activity during cycling, crystallinity is retained after reactions, mild decrease in porosity after cycling (N_2 77 K)	0.0097 mol(MeOH)/mol(Cu) = 4.4 μmol(MeOH)/g(cat)	169
Ti-NU-1000	cyclohexene	H_2O_2	cyclohexene partial pressure varied between 0.6 and 3 kPa with a total He flow rate of 25 mL/min, H_2O_2 injected in an acetonitrile stream with rate of 0.2 mL/h (partial pressure 0.8−3 kPa)	product distribution changes and total yield decreases over time	0.011 mol(C6)/mol(Ti)/min at 120 °C and 3 kPa both reactants, C6 = epoxide/diol/cyclohexanone/cyclohexanol/cycloexenone	170
Nb-NU-1000	cyclohexene	H_2O_2	cyclohexene partial pressure varied between 0.6 and 3 kPa with a total He flow rate of 25 mL/min, H_2O_2 injected in an acetonitrile stream with rate of 0.2 mL/h (partial pressure 0.8−3 kPa)	product distribution changes and total yield decreases over time	0.0059 mol(C6)/mol(Nb)/min at 120 °C and 3 kPa both reactants, C6 = epoxide/diol/cyclohexanone/cyclohexanol/cycloexenone	170

https://doi.org/10.1021/acs.chemrev.2c00537
Chem. Rev. XXXX, XXX, XXX−XXX

important role in energy generation during the maturation and implementation of emerging renewable energy technologies. However, difficulties in storing natural gas, especially methane, as well as its greenhouse effects, lead to flaring of large amounts of natural gas each year (e.g., 4790 billion cubic feet of natural gas were flared worldwide in 2015).[162] The functionalization of small hydrocarbons is a desirable alternative. In particular, the conversion of methane to methanol has been a holy grail in catalysis research.[163,164] Methanol is an attractive product, as it is both a commodity chemical with many industrial uses, and an alternative liquid fuel, easier to store than methane and with a much higher volumetric energy density. However, the high energy barrier for initial C−H activation and the tendency toward uncontrolled subsequent oxidation of increasingly weaker C−H bonds of the oxygenated products makes the selective oxidation of methane to methanol extremely challenging. Industrially, the upgrading of methane is done in multiple steps, involving the initial steam reforming reaction: $CH_4 + H_2O \rightarrow CO + 3H_2$, $\Delta G^\circ = +36$ kcal/mol. The CO and H_2 thus generated can further be used to synthesize larger hydrocarbons, via the Fischer−Tropsch process, or methanol: $CO + 2H_2 \rightarrow CH_3OH$, $\Delta G^\circ = -7$ kcal/mol. However, this indirect synthesis is energy consuming due to the reforming reaction; the direct functionalization of hydrocarbons through oxygen atom insertion is a much-desired alternative to the current multistep processes (Table 4).

Inspired by the C−H activation reactivity of high-valent iron-oxos in nature, the Long group examined reactivity of five-coordinated iron sites in Fe_2(dobdc) (Fe-MOF-74) in the presence of N_2O and ethane (Figure 9). The weak-field,

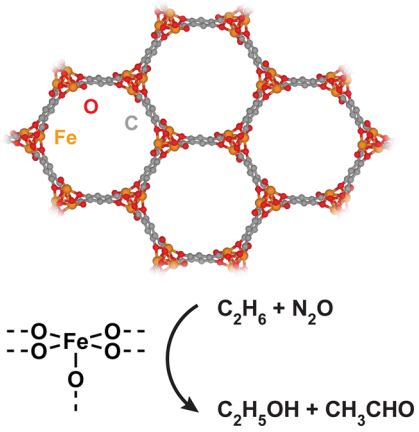

Figure 9. Exposed iron metal sites in MOF-74 facilitate the oxidation of ethane to ethanol with nitrous oxide.[165]

tetragonal coordination environment provided by MOF-74 was expected to facilitate the generation of highly reactive, high-spin iron-oxo species. Indeed, the diluted solid solution $Fe_{0.1}Mg_{1.9}$(dobdc) can mediate the oxygenation of ethane at 75 °C at the gas−solid interface with a TON of 1.6 (vs Fe) and good selectivity (ethanol:acetaldehyde 25:1). Diluting the iron sites with magnesium was found necessary for mitigating overoxidation and improving selectivity for ethanol.[165] Future experiments systematically varying the Fe:Mg ratio might be interesting to test if the mechanism necessitates neighboring Fe atoms: recent theoretical work has demonstrated that the reactivity of terminal and bridging oxygen species can differ substantially.[166] More recently, MIL-100(Fe) was found to mediate the low-temperature (473 K), low-pressure (1.5 kPa CH_4, 1.6 kPa N_2O) methane-to-methanol transformation using N_2O as an oxidant with very high yield (34% vs Fe).[167]

Drawing inspiration from the dicopper active site of particulate methane monooxygenase, Yaghi and co-workers installed imidazole ligands onto the Zr_6 clusters in MOF-808 and metalated them with Cu(I) in air to afford bis(μ-oxo)dicopper(II) moieties inside the pores. The structure was heavily disordered and thus could only be inferred from a combination of XAS, Raman spectroscopy, and DFT computation. In situ XAS revealed the oxidation of Cu(I) to Cu(II) species upon dosing of N_2O, followed by a subsequent reduction of Cu(II) to Cu(I) upon dosing of CH_4. Additionally, resonance Raman spectra of the MOF dosed with isotopically labeled O_2 or by ex situ dosing of N_2O reveals a stretching band consistent with a bis(μ-oxo) dicopper species. Cu EXAFS fitting upon dosing with N_2O is also consistent with the possibility of a bis(μ-oxo) dicopper species. The catalyst was found to be active for methane to methanol oxidation through a multistep N_2O/CH_4/steam cycle. The yield was very low (1−2% vs Cu) but exclusively methanol was formed at lower temperature (150 °C).[100]

Similar to copper oxo clusters exchanged into zeolites for methane-to-methanol conversion, copper oxo clusters were also deposited via atomic layer deposition (ALD) onto the zirconium oxo cluster of NU-1000. The catalyst was subjected to a stepwise $O_2/CH_4/H_2O$ cycle. Only 9% of the copper was found to be redox-active by XANES fitting. The methanol yield was low (19.7 $\mu mol_{(MeOH+Me2O)}/g_{catalyst}$, or 1% vs Cu), but the selectivity was decent (40−60% MeOH and Me_2O, the rest is CO_2).[168] In a later study, the same authors introduced copper into NU-1000 via aqueous cation exchange, achieving a mass loading of 2.9 wt % (1 Cu per Zr_6 cluster). They found the activity comparable to Cu-NU-1000 obtained via ALD, discussed previously, with 1 bar CH_4 (1% yield vs Cu, or 4.4 $\mu mol_{MeOH}/g_{catalyst}$) and the selectivity slightly higher (70% MeOH, the rest is CO_2). The performance was shown to improve if higher pressure was used during the methane treatment step (3.5% yield vs Cu at 200 °C, 40 bar, 90% selectivity). The catalytic site was proposed to be dimeric $Cu^{II}(\mu-OH)_2Cu^{II}O^\bullet$ supported on the Zr_6 node, albeit it is the minority species according to calculations.[169]

In addition to the oxygenation of alkane substrates discussed thus far, oxygenation reactions of alkenes were also studied on MOF platforms. Although this reactivity is often carried out in solution, examining the reaction in vapor phase allowed Ahn et al. to decipher the roles of solvent molecules. Specifically, the authors examined the gas-phase reaction between cyclohexene and H_2O_2 over niobium oxo and titanium oxo clusters deposited on NU-1000 and amorphous silica. NU-1000-based catalysts were found to produce a significant number of radical-derived products such as CO_2, cyclohexanol and cyclohexanone, whereas silica-based catalysts produce exclusively cyclohexene oxide and cyclohexanediol. Because radical-derived products stem from bimolecular decomposition of cyclohexenyl hydroperoxide, the difference in reactivity was attributed to the strong adsorption of cyclohexene and thereby a high concentration on the MOF surface. They also found that moving from condensed to vapor phase significantly reduced the apparent $\Delta H^\ddagger$ as a result of adsorption.[170]

Overall, we find that the use of dioxygen as an oxygen atom source has been much more challenging to achieve than the use of nitrous oxide. This can be attributed to the kinetic stability of N_2O, which prevents over oxidation. However, this

https://doi.org/10.1021/acs.chemrev.2c00537
Chem. Rev. XXXX, XXX, XXX−XXX

Table 5. Comparison of Oxidative Dehydrogenation MOF Catalysts

MOF	hydrocarbon	oxidant	reaction conditions	catalyst stability	activity	ref
V@UiO-66	cyclohexene	O_2	packed-bed flow reactor, cyclohexene introduced via vaporiztion at 120 °C at 0.2 mL/min and a 20 vol % O_2/N_2 stream mixed to 1.6 mol % cyclohexene and 3.2 mol % O_2, total flow rate 50 mL/min, GHSV = 1653 h^{-1}	crystallinity and porosity preserved *post operando*, no metal leaching, catalyst active for >48 h on stream	E_a = 110 kJ/mol. 100% benzene at 250 °C	174
Co-SIM+NU-1000	propane	O_2	48 mL/min O_2 (10% diluted with He), 96 mL/min C_3H_8 (3%, diluted with Ar), 230 °C	some loss in porosity, crystallinity mostly preserved, some Co(II) species by XPS after catalysis	$E_a \sim 210$ kJ/mol, 0.54 ± 0.12 h^{-1} at 230 °C	175
Co-AIM+NU-1000	propane	O_2	48 mL/min O_2 (10% diluted with He), 96 mL/min C_3H_8 (3%, diluted with Ar), 230 °C	some loss in porosity, crystallinity mostly preserved, some Co(II) species by XPS after catalysis	$E_a \sim 200$ kJ/mol, 1.02 ± 0.09 h^{-1} at 230 °C	175
Co-SIM-NDC-SALI-NU-1000	propane	O_2	48 mL/min O_2 10%, diluted with He), 96 mL/min C_3H_8 (3%, diluted with Ar), 0.5 bar, 4 h, 230 °C	mild loss in porosity and crystallinity preserved after catalysis	0.68 h^{-1} at 230 °C	176
CoAIM-NiSIM+NU-1000	propane	O_2	48 mL/min O_2 10%, diluted with He), 96 mL/min C_3H_8 (3%, diluted with Ar), 0.5 bar, 4 h, 230 °C	large loss in porosity, crystallinity deteriorates after catalysis	2.41 ± 0.22 h^{-1} at 230 °C	177
CoAIM-ZnSIM+NU-1000	propane	O_2	48 mL/min O_2 10%, diluted with He), 96 mL/min C_3H_8 (3%, diluted with Ar), 0.5 bar, 4 h, 230 °C	some loss in porosity, crystallinity preserved after catalysis	1.65 ± 0.09 h^{-1} at 230 °C	177
CoAIM-AlSIM+NU-1000	propane	O_2	48 mL/min O_2 10%, diluted with He), 96 mL/min C_3H_8 (3%, diluted with Ar), 0.5 bar, 4 h, 230 °C	some loss in porosity, crystallinity preserved after catalysis	0.95 ± 0.10 h^{-1} at 230 °C	177
CoAIM-TiSIM+NU-1000	propane	O_2	48 mL/min O_2 10%, diluted with He), 96 mL/min C_3H_8 (3%, diluted with Ar), 0.5 bar, 4 h, 230 °C	large loss in porosity, crystallinity deteriorates after catalysis	0.76 ± 0.08 h^{-1} at 230 °C	177
CoAIM-MoSIM+NU-1000	propane	O_2	48 mL/min O_2 10%, diluted with He), 96 mL/min C_3H_8 (3%, diluted with Ar), 0.5 bar, 4 h, 230 °C	large loss in porosity, crystallinity deteriorates after catalysis	0.47 ± 0.05 h^{-1} at 230 °C	177
Fe-MIL-100	propane	N_2O	recirculating batch reactor system; recirculation rate 70 mL/min, total reactor volume 68 mL. 35 kPa N_2O, 1.3 kPa C_3H_8, 77.7 kPa He	crystallinity and porosity preserved	majority products propylene and 2-propanol; minority products 1-propanol, acetone, 1,2-diol, 1.3-diol	178
Fe-MIL-100	ethane	N_2O	recirculating batch reactor system, recirculation rate 70 mL/min, total reactor volume 68 mL, 10 kPa N_2O, 10 kPa C_2H_6, 94 kPa He	crystallinity and porosity preserved	majority products ethylene and ethanol, minority product acetic acid	178

https://doi.org/10.1021/acs.chemrev.2c00537
Chem. Rev. XXXX, XXX, XXX−XXX

is also the result of the difficulty to promote the 4-electron reduction of O_2 at single metal sites within MOFs. The ability to use dioxygen as oxidant in the case of Cu-NU-1000 rests upon the fact that the multinuclear copper cluster can distribute the redox burden associated with the 4-electron reduction of O_2 among multiple metal centers. We propose that judicious design of well-defined multimetallic, redox-active cluster SBUs within MOFs capable to cooperatively reduce O_2 by 4 electrons could lead to improved technologies in alkane oxygenation catalysis. To this end, Dincă and co-workers have recently demonstrated the viability of four-electron reduction of molecular O_2 to metal-oxo species by employing the polynuclear, site-isolated tetramanganese cluster of MnMnBTT.[171] The resulting bis(μ-oxo) species catalytically oxidize weak C−H bonds in solution and, more importantly, is able to evolve O_2.

3.2.2. Oxidative Dehydrogenation. Propylene is an important industrial chemical for the production of polypropylene and a variety of monomers, such as acrylonitrile, acrylic acid, and propylene oxide.[172] Direct dehydrogenation of propane is strongly endothermic and thus requires high temperature (500−700 °C) for productive equilibrium (Table 5).[173] Coupling the dehydrogenation reaction with combustion of hydrogen brings the reaction into the exothermic regime. The oxidative dehydrogenation (ODH) of propane is therefore a promising alternative to direct dehydrogenation to meet the increasing gap between demand and supply. The key parameter of interest, and the current limitation, for ODH is the selectivity of propylene versus combustion product such and CO and CO_2, especially at high conversion.

Inspired by the oxidative dehydrogenation reactivity of supported vanadium oxides for various hydrocarbons, Nguyen et al. installed V(V) onto the Zr_6 clusters (0.6 V per Zr_6) of UiO-66 via impregnation in methanol and tested its activity for ODH of cyclohexene to benzene, $C_6H_{10} + O_2 \rightarrow C_6H_6 + 2\ H_2O$.[174] They proposed that V ligates to the missing linker defect sites in mostly mononuclear form, based on combined evidence from NMR, Raman, and diffuse-reflectance UV−vis and IR spectroscopies. When fed with a flow of 1.6% cyclohexene and 3.2% O_2 in N_2, the catalyst V-UiO-66 can achieve 100% selectivity for benzene at 250 °C, albeit with low conversion (<2%). With increasing temperature up to 350 °C, the selectivity drops rapidly and settles at ∼80% above 270 °C (versus total carbon, the rest being CO and CO_2), while the conversion gradually increases to >85% at 350 °C. The conversion remains unchanged (>85%) after 48 h at 350 °C and SEM and PXRD confirmed the crystalline framework remains intact.

Reasoning that site isolation would improve the stability of nanosized spinel Co_3O_4 catalysts, previously shown to promote the propane ODH reaction, Li et al. incorporated cobalt-oxo clusters onto the isolated Zr_6 nodes of NU-1000.[175] Two methods were used for cobalt deposition, the gas-phase atomic-layer-deposition in MOF (AIM), and solution-phase solvothermal-deposition in MOF (SIM). Despite similar metal loadings (4 Co per Zr_6), the two methods gave rise to cobalt clusters with different local structures. Regardless, at 230 °C, both MOF catalysts outperformed cobalt dispersed on zirconia powder in terms of turnover frequency per Co (1.02 ± 0.09 and 0.54 ± 0.12 versus 0.15 h^{-1}) and both remained stable over a time-on-stream of 24 h. Between the two MOF catalysts, Co-AIM+NU-1000 displayed better activity and selectivity than Co-SIM+NU-1000 under identical conditions, which the authors ascribed to the more spinel-like cluster structure in the former as indicated by EXAFS measurements. High propylene selectivity can be achieved at lower temperatures and lower conversion, i.e., selectivity up to 100% at 180 °C and <2% conversion, but combustion products (i.e., CO_2) become dominant at higher conversion or higher temperatures. Additional modification to the cobalt-oxo cluster can be achieved by selectively blocking certain binding sites on the Zr_6 cluster with ditopic carboxylate ligands. The different cobalt-oxo sites were confirmed by differential envelop density (DED) analysis. The resulting catalyst was slightly more active (TOF = 0.68 ± 0.05 h^{-1} at 230 °C) but undergoes similar rapid loss of selectivity at higher conversion.[176] Larger improvements, although still not significant, can be achieved by deposition of different metal-oxo clusters before the deposition of cobalt onto NU-1000. These metal-oxo clusters installed via SIM were found to occupy roughly the same crystallographic position as the initial Co-oxo clusters in Co-SIM+NU-1000 based on DED analysis. The Co-oxo clusters installed thereafter were determined to be mononuclear by EXAFS. As one increases the Lewis acidity of the promoter metal (Ni(II) < Zn(II) < Al(III) < Ti(IV) < Mo(VI)), the turnover frequency decreases, and the least Lewis acidic metal Ni(II) gives the highest TOF of 2.41 ± 0.22 h^{-1} at 230 °C. In all cases, the cobalt-free material had no ODH reactivity, and the selectivities were identical.[177]

Another class of MOF catalysts for ODH feature $Fe_2MO(RCO_2)_6$ as the metal node, inspired by nonheme Fe enzymes competent for C−H activation, as well as their molecular mimics. In a recirculating batch reactor at 120 °C, the $Fe_3O(RCO_2)_6$ node of MIL-100(Fe) was found to mediate the oxidation of propane with N_2O into propylene and oxygenated products such as 2-propanol.[178] Five-coordinated high-spin (S = 2) Fe(II) was determined to be the active site in the precatalyst. Quantifications via NO titration and Mössbauer spectroscopy suggested only 4−5% of all iron in MIL-100(Fe) participates in the catalysis. Interestingly, no oxidation products were observed when N_2O and propane were fed sequentially despite consumption of N_2O, implying that the active site is only transiently formed in the absence of propane. Later, PCN-250(Fe_2M), which contains the same trinuclear cluster as MIL-100, $Fe_2MO(RCO_2)_6$ (M = Mn, Fe, Co, Ni; R = 3,3′,5,5′-azobenzenetetracarboxylate), were tested for cyclohexane ODH at 250 °C with N_2O as oxidant.[179] Cyclohexane was chosen because of its similar C−H bond strength to propane but simpler product distribution. At low conversion (<8%), all four MOFs gave relatively high selectivity for cyclohexene (>75%). The highest possible selectivities are obtained by extrapolation to zero conversion, which are 100% for PCN-250(Fe_3) and (Fe_2Mn) and 95% for (Fe_2Co) and (Fe_2Ni). The reaction rates follow the trend $Fe_3 \sim Fe_2Mn > Fe_2Co > Fe_2Ni$, which the authors correlated to the increasing N_2O activation barrier in the sequence.

Systems capable of promoting ODH of propane and other small alkanes still suffer from low selectivities at high conversion, and most probe reactions are carried out at low concentration of reactants, diluted with inert gases such as N_2 and Ar. In the future, more selective systems must be designed and investigated. In particular, the pathways for alkane dehydrogenation, and further oxidation reactivity must be better understood on the studied platforms. This could facilitate the informed design of new systems where the undesirable pathways can be disfavored. Still, the main

https://doi.org/10.1021/acs.chemrev.2c00537
Chem. Rev. XXXX, XXX, XXX−XXX

Table 6. Comparison of Carbon Monoxide Oxidation MOF Catalysts[a]

MOF	reaction conditions	catalyst stability	activation energy	rate	ref
MOF-808(Ce)	60−150 °C, 1%:2.5%:10% = CO:O_2:N_2, He balance, flow rate = 1300 mL/min/g	no *post operando* characterization	48.1 kJ/mol	0.00024−0.01095 mol/mol (SBU)/min	186
Cu-UiO-66	80−250 °C, 1%:1% = CO:O_2, N_2 balance, 30 N mL/min	stable on stream for 20 h, crystallinity preserved after catalysis	43.5 kJ/mol	∼4−375 μmol/g/s or 0.0132−.05 mol/mol/min	187
Ni-4,5-imidazoledicarboxylate	25−305 °C, 100 mL/min, 1%:20% = CO:O_2, He balance, HSV = 20,000 mL/min/g(cat)	crystallinity preserved after catalysis	64.9 kJ/mol	∼0.006 to 0.06 mol/mol/min (202−305 °C)	192
Cu-HKUST-1	1%:20% = CO:O_2, space velocity = 24,000 mL/h, flow rate = 20 mL/min	undergoes decomposition at 240 °C, low temperature reactivity is attributed to defects, but may be MOF decomposition		T^{50} = 235 °C, T^{100} = 240 °C, no activity below 200 °C	196,198,207
Cu-1*H*-pyrazole-4-carboxylate	1%:6% = CO:O_2, Ar balance, space velocity = 30,000 mL/h/g(cat), flow rate = 30 mL/min	deterioration of crystallinity after catalysis	72.8 kJ/mol	∼0.004−0.055 mol/mol (Cu)/min	197
CuZn-FDM-3	1% CO in air, flow rate = 50 mL/min	crystallinity preserved after catalysis		T^{50} = 200 °C	198
CuZn-FDM-4	1% CO in air, flow rate = 50 mL/min	crystallinity preserved after catalysis		T^{50} = 180 °C	198
CuZn-FDM-5	1% CO in air, flow rate = 50 mL/min	crystallinity deteriorates after catalysis		T^{50} = 215 °C	198
CuZn-FDM-6	1% CO in air, flow rate = 50 mL/min	crystallinity preserved after catalysis		T^{50} = 195 °C	198
CuZn-FDM-7	1% CO in air, flow rate = 50 mL/min	crystallinity preserved after catalysis		T^{50} = 190 °C	198
Cu-5-methylisophthalate	1%:20% = CO:O_2, He balance, space velocity = 20,000 mL/g(cat)/h, flow rate = 100 mL/min, 25−205 °C	crystallinity mostly preserved after catalysis	70.1 kJ/mol	∼0.0006−0.012 mol/mol(Cu)/min	199
Cu-5-nitroisophthalate	1%:20% = CO:O_2, He balance, space velocity = 20,000 mL/g(cat)/h, flow rate = 37 mL/min, 25−205 °C	crystallinity mostly preserved after 20 h on stream	62.3 kJ/mol	∼0.004−0.035 mol/mol(Cu)/min	200
Co-MOF-74	1% CO in air, flow rate = 30 mL/min	decomposition above 130 °C		T^{50} = 84 °C	202
Co_3(benzenetricarboxylate)$_2$•12H_2O	1 vol% CO and 37.5 vol% air (sum ≠100%). Flow rate = 800 mL/min, GHSV = 48,000 mL/g(cat)/h	no *post operando* characterization, the MOF likely collapses between 150 and 200 °C (TGA)		T^{100} = 160 °C	203
Co_3O_4 (reference)	5%:10% = CO:O_2, He balance, flow rate = 50 mL/min		70 kJ/mol	T^{50} = 104 °C; at 90 °C, 16.4 μmol/g/s	204
thermolyzed Co-ZIF-67 (600 °C) (reference)	0.1%:20% = CO:O_2, He balance, flow rate = 25 mL/min, space velocity = 7500 mL/g(cat)/h		22 kJ/mol	T^{100} = 0 °C	201
Cu_x[Ce(La)]$_{1-x}O_x$ (reference)	∼40−180 °C, 1:1 = CO:O_2	activity changes with precalcination	x = 0.01, 41 kJ/mol; x = 0.09, 67 kJ/mol	x = 0.01, ∼0.007−0.2 mmol/g/min	185
Cu (reference)	200−350 °C, 97:3 = CO/O_2	will oxidize to Cu(II)O in an oxygen rich atmosphere	36.8 kJ/mol	∼0.003−0.02 mmol/min	184
Cu(I)$_2$O (reference)	200−350 90:10 = CO/O_2	will oxidize to Cu(II)O in an oxygen rich atmosphere	58.2 kJ/mol	∼0.0001−0.008 mmol/min	184
Cu(II)O (reference)	200−350 °C, 66:33 = CO/O_2		69.9 kJ/mol	∼0.00005−0.008 mmol/min	184
Pt (reference)	200−350 °C, 66:33 = CO/O_2		83.3 kJ/mol	∼0.0001−0.06 mmol/min	184

[a] T^{50} = temperature of half-conversion.

https://doi.org/10.1021/acs.chemrev.2c00537
Chem. Rev. XXXX, XXX, XXX−XXX

challenge arises from the tendency of O_2 to fully oxidize hydrocarbons at elevated temperatures, in the presence or in the absence of the MOF support. Therefore, selective activation of alkanes at lower temperatures must be achieved in order for ODH processes to become more efficient.

3.2.3. Carbon Monoxide Oxidation. CO oxidation has been pursued as a model reaction for heterogeneous catalysis, as well as for practical purposes given that carbon monoxide is an air pollutant (Table 6).[180] In particular, low temperature CO oxidation catalysts are needed for catalytic converters.[181] Typically, the CO oxidation reaction is interpreted as $CO + {}^1/_2 O_2 \rightarrow CO_2$, where $\Delta G^\circ = -61$ kcal/mol, and remains thermodynamically favorable below ~3000 °C, at which point entropy dominates and the reverse reaction becomes favorable.[132] Alternative reactions have been proposed, such as the utilization of nitrous oxide as the O atom donor, $CO + N_2O \rightarrow CO_2 + N_2$, $\Delta G^\circ = -86$ kcal/mol. Although such a reaction has been computationally analyzed and there are predictions for which materials to pursue this reaction with, a practical system is yet to be realized.[182]

CO oxidation is a useful model reaction due to positive correlation scaling relations, which state that the adsorption energies and reaction barriers involving CO can be correlated with other bound ligands.[183] In particular, the reaction progress can be easily monitored with IR spectroscopy. For example, CO bound to Cu(II) and Cu(I) sites can be easily observed and differentiated in situ during the course of the reaction.[19] As far as practical catalysis goes, much of the current research focuses on decreasing the temperature required for turnover, finding ways of increasing the rate of catalysis (such as increasing surface area), and increasing stability toward poisons (such as water).

Catalysts for this reaction can be grouped into two categories: those based on late first row transition metals and those based upon platinum group metals. We note that one of the dominant industrially used catalysts for this reaction, hopcalite, a Mn−Cu oxide, belongs to the former group.[180] Of the former group, much of the research focuses on the catalytic properties of copper. Copper metal, copper(I) oxide, and copper(II) oxide are all competent for CO oxidation, with activation energies of 36.8, 58.2, and 69.9 kJ/mol, respectively.[184] A key feature of this data is that the presence of reduced copper species decreases the activation energy, thereby allowing for catalysis at lower temperatures. This attribute has been demonstrated by the inclusion of Cu in CeO_2, which stabilizes Cu(I) sites and improves activity.[185] Redox active supports also make a difference within MOFs. It has been recently demonstrated that three-coordinate copper-(II) embedded within MOF-808(Ce) is active for CO oxidation (with an activation energy of 48.1 kJ/mol), while a similar Cu species supported within the isostructural MOF-808(Zr) is relatively inactive, a difference that has been ascribed to Ce participating in the catalytic cycle by way of reducing the Cu.[186] Interestingly, copper(II) supported onto UiO-66 (a framework chemically similar to MOF-808(Zr)) is also active for CO oxidation upon pretreatment with H_2, with an apparent activation energy of 43.5 kJ/mol.[187] The pretreatment is the likely cause of this activity, as it generates the reduced copper species active for catalysis. Contrary to experiments, DFT calculations of a single copper atom on UiO-66 reveal that the barriers for CO oxidation on Cu(II) are slightly lower in energy than those for Cu(I).[188] However, in this case, the calculated activation barriers for CO oxidation are 3 to 4 times larger than experimentally determined values. These discrepancies between experiment and computations could be due to the identified mechanism for the oxidation reaction. In comparison to the late first row transition metal catalysts, platinum metal has an activation energy of 83.3 kJ/mol.[184]

The leading catalysts for CO oxidation are spinels, mixed metal oxides.[189] Many of these, such as $MnCo_2O_{4.5}$, can have T_{50} and T_{100} values (the temperature at which half or all of the feed stream is converted) near or even below room temperature.[190] One key feature to note is that the activity of these catalysts is intrinsically tied to the surface area. Thus, a MOF mimic of such systems could result in a high-performance material. Perhaps there is potential for such mimics using mixed metal MOF-74 analogues,[191] however, the success of such a material would depend upon the dominant mechanism for CO oxidation in the spinel parent. Certain mechanisms involving oxygen atom vacancies would be prohibited in a MOF-74 structure as bridging oxo ligands are absent, however, such a mechanism could be allowed if a mixed metal framework with metal oxide SBUs was used as a mimic instead.

Here we will discuss some of the progress toward using MOFs as scaffolds to support active catalyst sites (such as Cu(I)) while maintaining high surface areas. While this is a relatively recent pursuit (with the first study of MOF based CO oxidation occurring only as recently as 2006, using a nickel-imizadole-4,5-dicarboxylate framework[192]), there has been considerable progress more recently.

Similar to heterogeneous Cu, Cu_2O, and CuO, many copper-based MOFs catalyze CO oxidation. One of the most widely studied system in this sense is HKUST-1, a prototypical MOF composed of Cu_2(tetracacrboxylate) paddlewheel SBUs and 1,3,5-benzenetricarboxylate (Figure 10). Early on, it was believed that every dimeric Cu(II) SBU was capable of performing catalysis, as the IR handle for CO bound to Cu(II) (2180 cm^{-1}) decreases as the reaction progresses, while that to Cu(I) (2120 cm^{-1}) remains constant.[194] These Cu(I) sites were believed to be inert defects. It was subsequently demonstrated by comparing the catalytic activity of pristine thin films of HKUST-1 against those with engineered defects, that the active sites are in fact Cu(I)−Cu(II) SBU defects.[19] These defective thin films are engineered by activating the framework at elevated temperatures (>150 °C) under vacuum. This process causes decarboxylation of the 1,3,5-benzene-tricarboxylate linkers, a surprising occurrence at fairly low temperatures as this temperature is in the pre-shoulder before significant mass loss according to thermogravimetric analysis (TGA).[195] While CO bound to Cu(II) sites decreases as the reaction progresses for defective thin films, for pristine frameworks, CO is not consumed. It was thus rationalized that migration of CO from Cu(II) to Cu(I) is fast on the time scale of IR spectroscopy. DFT and wave function calculations suggest that CO binds to Cu(II) and O_2 to Cu(I), which undergo a bond formation process, followed by coordination of a second equivalent of CO and release of two equivalents of CO_2. Considering that the reduced copper within defects is responsible for the catalytic activity, further disorder and defects may increase activity. As such, it has been demonstrated that amorphized HKUST-1 promotes CO oxidation at lower temperatures than pristine HKUST-1. Loading of palladium(IV) oxide into this material (another

https://doi.org/10.1021/acs.chemrev.2c00537
Chem. Rev. XXXX, XXX, XXX−XXX

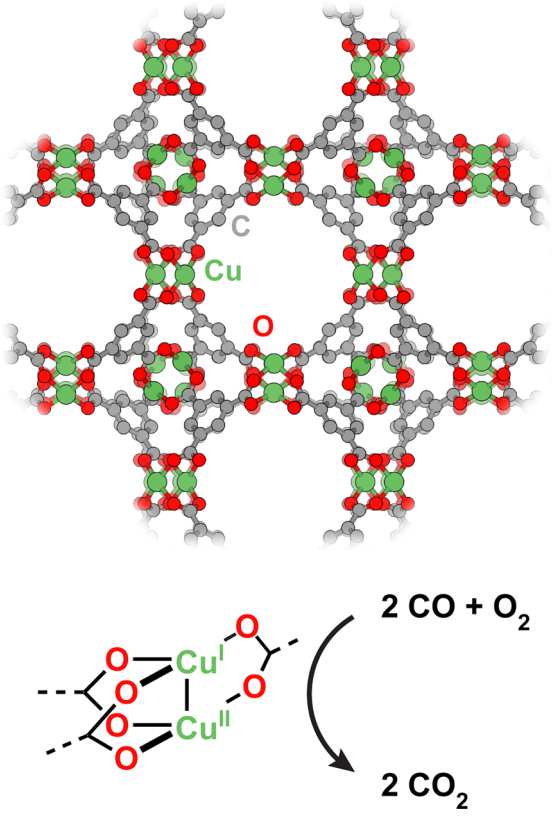

Figure 10. Defective HKUST-1 with Cu(I)−Cu(II) sites catalyzes the oxidation of carbon monoxide.[193]

active metal for CO oxidation) further decreases the temperature at which catalytic activity begins.[196]

Another class of copper frameworks that has been explored for CO oxidation catalysis comprises materials built from pyrazole-4-carboxylates. Depending on the crystallization conditions and metals present (as with combinations of copper and zinc), pyrazole-4-carboxylate frameworks can adopt one of several topologies. As a monometallic framework, copper and this linker adopt a geometry containing trinuclear triangular SBUs of Cu(II). This Cu material is competent for CO oxidation with an activation energy of 72.8 kJ/mol.[197] Mixed metal Zn/Cu frameworks (possessing the same Cu cluster) have also been demonstrated to promote CO oxidation. These frameworks exhibit two distinct CO binding sites identified by respective C−O stretching bands at 2171 and 2109 cm^{-1}, which are assigned to Cu(II) and Cu(I).[198]

A similar microporous framework, composed of dicopper paddlewheels and 5-methylisophthalic acid performs CO oxidation catalysis with an activation energy of 70.1 kJ/mol (similar to that of CuO).[199] Interestingly, the stretching frequency of the bound CO is quite red-shifted for a Cu(II) site, 2113 cm^{-1}. It is worth noting that this framework is activated in air at 250 °C, and decarboxylation of linkers to form Cu(I)−Cu(II) defects cannot be excluded. 5-Nitroisophthalic acid also forms frameworks with copper, containing pentameric SBUs, which catalyzes the reaction with an activation energy of 62.3 kJ/mol.[200]

Other frameworks that have been explored include ZIFs, M-MOF-74, MIL-125, and MOF-808. It has been demonstrated that the thermolysis product of ZIF-67 yields a catalyst that is moisture insensitive, all the way up to 500 ppm of H_2O, and has a low activation energy of 22 kJ/mol.[201] These catalysts are active at remarkably low temperature, down to 0 °C. Interestingly, there is a slight dip in CO conversion between 90 and 130 °C under wet conversion. The M-MOF-74 series has been demonstrated to catalyze CO oxidation, with higher activity correlating with stronger Lewis acidic metals and with redox-active metals: cobalt instead of zinc or magnesium.[202] A different cobalt framework, made with 1,3,5-benzenetricarboxylate, is also active for CO oxidation allowing near completion at 160 °C.[203] For Co-MOF-74, its activity has been rationalized by analogy with cobalt oxide: the infinite SBU of Co-MOF-74 can be considered as a slice of bulk cobalt oxide.[204] Copper oxide nanoparticles can be embedded with most frameworks (including MIL-125(Ti)[205] and MIL-53-(Al)[206]), with the resulting composites acting as competent catalysts.

3.3. Redox Neutral C−C Bond Forming Reactions

3.3.1. Olefin Dimerization and Polymerization. Oligomerization of ethylene into longer-chain linear α-olefins (LAOs) is a particularly important industrial process for the upgrading of ethylene.[208,209] The selective dimerization of ethylene to 1-butene has been the topic of many studies in recent years, as the latter is a comonomer for linear low-density polyethylene and high-density polyethylene (Table 7). The key challenge for heterogeneous ethylene dimerization catalysts is selectivity. For one, the overwhelmingly desirable product 1-butene is less thermodynamically stable than the internal butene isomers. In addition, high selectivity for butene is required over larger oligomers to prevent reactor fouling and catalyst deactivation, a particular challenge given the structure similarities between dimerization and polymerization catalysts.[62] We note that efficiently separating the MOF catalyst from polyethylene resulting from polymerization remains an unsolved problem. Hence, a key parameter to consider when evaluating olefin dimerization catalysts is their selectivity, which must be kept as close to 100% as possible, even at the cost of the lifetime of the catalyst. A second consideration arises from the exothermic nature of olefin dimerization. For instance, for ethylene dimerization to 1-butene $\Delta H° = -25.0$ kcal/mol of 1-butene formed. Given the heat generated during the dimerization process, catalysts that are optimized for operation at elevated temperatures (>50 °C) eliminate the need for active cooling, which improves overall process efficiency. In terms of catalyst design principles, it has been shown that nickel aluminosilicate materials can catalyze the dimerization of light olefins at their Ni(II) sites.[210−212] Therefore, many studies have emerged in the MOF literature, surveying the activity of Ni(II) nodes toward alkene dimerization. We note that the use of later transition metals, such as Ni, over earlier transition metals capable of promoting olefin dimerization, such as V or Cr, generally results in better selectivity for dimerization products over larger polymerization products. Notably, most nickel-based ethylene dimerization catalysts use a metal−alkyl initiator, often Et_2AlCl.[213,214] It is often suggested that the ethylene dimerization reaction at Ni centers proceeds through a Ni-alkyl species in what is known as the Cossee−Arlman mechanism, which was first suggested for homogeneous reactions.[215,216] An alkene equivalent coordinates to the Ni-alkyl species and the C−C bond formation occurs via a migratory insertion mechanism to generate a new Ni-alkyl species. Lastly, the alkene product can be formed by a β-hydride elimination reaction. The next alkene equivalent can coordinate to the Ni−H species thus formed,

https://doi.org/10.1021/acs.chemrev.2c00537
Chem. Rev. XXXX, XXX, XXX−XXX

Table 7. Comparison of Olefin Dimerization and Polymerization MOF Catalysts

MOF	reaction conditions	catalyst stability	activity	product distribution	ref
Ni-MOF-74 (Ni_2(dobdc))	5 bar C_3H_6, 180 °C, flow rate 30 mL/min, WHSV = 64 h^{-1}	crystallinity preserved after catalysis	0.61−2.13% conversion	0.29−1.01% C_6 and 0−0.054% C_9 after 371 min, 11 different C_6 isomers formed	219
Ni_2(dobpdc)	5 bar C_3H_6, 180 °C, flow rate 30 mL/min, WHSV = 64 h^{-1}	no *post operando* characterization	∼0.25−0.75% conversion	10 different C_6 isomers formed	219
NU-1000-(bpy)Ni^{II}	Et_2AlCl activator, 15 bar C_2H_4, 21 °C	active after 3 cycles, some loss in crystallinity after catalysis, activity decreases over time on stream due to polyethylene buildup	1950 mol(butenes)/mol(Ni)/h	85% 1-butene:8% 2-butene:6% C_{6+}	220
Ni-AIM@NU-1000	Et_2AlCl, 2 bar total, 1:2:3 = C_2H_4:H_2:Ar, 45 °C	crystallinity preserved after 20 h catalysis, some polyethylene buildup on the crystallites (SEM)	252 mol(C_2)/mol(Ni)/h	at 5% C_2H_4 conversion: 46% C_4:8% C_6:46% C_8	138
Ni-UiO-67-bpy	26 bar C_2H_4, 4 bar inert gas (He/Ne), flow rate = 30 mL/min, contact time 5.0 mg(cat)min/mL(C_2H_4)	crystallinity preserved after catalysis, large decrease in porosity after catalysis	41 mol/mol(Ni)/h	41% 1-butene:26% *trans*-2-butene:32% *cis*-2-butene:1% C_{6+}	221
Ni-Facac-AIM-NU-1000	2 bar C_2H_4, 45 °C, flow rate = 20 sccm	the TOF drops off and C4 selectivity for C_4 increases after an induction period, crystallinity retained after catalysis	12.6 mol/mol(Ni)/h(Ni)/h	after induction period, ∼75−80% 1-butene:∼10−15% *trans*-2-butene:∼10% *cis*-2-butene, with very little C_{6+}	222
Ni-Acac-AIM-NU-1000	2 bar C_2H_4, 45 °C, flow rate = 20 sccm	crystallinity retained after catalysis	15.84 mol/mol(Ni)/h	after induction period, ∼75−80% 1-butene: ∼10−15% *trans*-2-butene: ∼10% *cis*-2-butene, with very little C_{6+}	222
Ru-HKUST-1	42 bar, 650 °C, 10−20 mol/g/h C_2H_4	mean life >120 h, no *post operando* characterization	200 mol/mol(Ru)/h	99% 1-butene	223
Cr-MFU-4l	$AlMe_3$ pretreatment, 40 bar C_2H_4, 130 °C, 1 h	$AlMe_3$ treated MOF retains some crystallinity and porosity, *post operando* characterization convoluted by polyethylene	52,000 mol(C_2H_4)/mol(Cr)/h	polyethylene, polydispersity index = 1.36, number-averaged molecular weight = 298 kDa	224
S-MOF-808	4 mmol/h propene, 53 mmol/h He, 1.01325 bar, 100 °C	no *post operando* characterization	<0.05 mmol/g(cat)/h		233
S-MOF-808	4 4 mmol/h 2-methylpropene, 53 mmol/h He, 1.01325 bar, 100 °C	active for 22 h on stream, MOF retains crystallinity and some loss in porosity after catalysis	6.28 mmol/g(cat)/h	72.5% dimers:23.7% trimers:3.6% tetramers	233
S-MOF-808	4 mmol/h 1-butene, 53 mmol/h He, 1.01325 bar, 100 °C	no *post operando* characterization	0.05 mmol/g(cat)/h oligomerization and competitive isomerization at 1.03 mmol/g(cat)/h	48.9% trimers:51.0% tetramers	233
Ni-MFU-4l (reference)	in toluene, 50 bar C_2H_4, (a) 0 °C, 100 equiv methylaluminoxane, (b) 25 °C, 500 equiv methylaluminoxane	crystallinity preserved after catalysis, active after 8 cycles	(a) 22,600 mol/mol(Ni)/h, (b) 41,500 mol/mol(Ni)/h	(a) 96.2% 1-butene:2.2% 2-butene:1.6% C_6, (b) 92.0% 1-butene:5.4% 2-butene:2.6% C_6	62

https://doi.org/10.1021/acs.chemrev.2c00537
Chem. Rev. XXXX, XXX, XXX−XXX

and regenerate a Ni-alkyl species following a migratory insertion step, to complete the catalytic cycle.[217] Metzger et al. verified the often-suggested ethylene dimerization mechanism in a Ni-incorporated MFU-4l framework by a combination of isotope labeling studies, mechanistic probes, and DFT calculations, confirming that MOFs mimic homogeneous catalysts both functionally and mechanistically.[218]

In 2014, Milnar et al. investigated Ni-MOF-74, a Ni(II) framework with open-metal sites, and demonstrated that the material is active for both ethylene and propylene dimerization.[219] Specifically, at 180 °C and 5 bar olefin pressure, Ni-MOF-74 catalyzes the dimerization in flow with >95% dimer selectivity. For both olefins, an induction period was observed, and maximum activity was reached at around 50 min time-on-stream, after which the activity quickly diminished. The activity for ethylene dimerization was higher than that for propylene. The isostructural Mg-MOF-74 showed no activity, thus supporting the hypothesis that the nickel ions act as the active sites. The catalyst is apparently self-activating (i.e., no alkylating activator used), avoiding the need for expensive alkylaluminum activators, but the exact mechanism of activation has not been elucidated. Nevertheless, it can be hypothesized that the induction period noticed is caused by the comparatively slow catalyst self-activation step.

Madrahimov et al. tested a bpyNi^{II} (bpy = 2,2′-bipyridyl) complex grafted onto NU-1000 for ethylene dimerization.[220] The presence of bpyNiCl_2 units in the grafted MOF was confirmed through diffuse-reflectance UV−vis, but it was also clear that a portion of Ni was directly deposited onto the Zr_6 cluster. Under batch condition (15 bar ethylene, room temperature), the Et_2AlCl-preactivated catalyst displayed a butene activity of 1560 mol C_4/(mol Ni·h) with decent C_4 selectivity (82%, rest hexenes and octenes) but poor 1-butene selectivity (57%, rest 2-butene). Under flow condition (20% ethylene in helium, 1 bar, room temperature), high activity (>95% conversion), and high C_4 selectivity (98%) was observed initially. The conversion decayed over time to 20% after 19 h time-on-stream, while the selectivity remained good (>75%). Polymer formation was observed and cited as the reason for catalyst deactivation, but no quantification was reported. In a related report, Kømurcu et al. studied bpyNi^{II} moieties incorporated into the framework of UiO-67, where the linkers are partially exchanged for 2,2′-bipyridine-4,4′-dicarboxylic acid.[221] After an O_2 treatment at 300 °C, the UiO-67 with bpyNi^{II} is capable of ethylene dimerization in flow (26 bar C_2H_4, 250 °C) in a self-activating manner after an induction period on the order of hours. Turnover frequencies of up to 41 mol C_4/(mol Ni·h) were observed. At conversion below 6%, the C_4 selectivity in the gaseous portion was good (99%) but the 1-butene selectivity was low (41%, rest 2-butene). Weight increase in the spent catalyst (15%) suggested formation of heavy oligomers/polymer as one reason of deactivation.

In both cases of bpyNi^{II} immobilized in Zr_6-MOF, direct metalation at the defective Zr_6 site was observed and partial activity was attributed to the Ni in these sites. Direct vapor-phase deposition of Ni(II) onto the node of NU-1000 and activation with Et_2AlCl gave rise to oligomerization catalyst with a turnover frequency of 252 mol C_2/(mol Ni·h) (45 °C, 2 bar). The selectivity for C_4 (<46%) and conversion (<5%) were low, and polymer formation was observed.[138] Modifying the Zr_6 node with hexafluoroacetylacetone or acetylacetone, which changes the accessibility of certain facets and the acidity of OH in the cluster, improves the selectivity (100% C_4, 80% 1-butene) at the cost of activity (<20 mol C_2/(mol Ni·h)).[222]

More recently, Agirrezabal-Telleria et al. discovered that Ru-HKUST-1 acts as a self-activating catalyst for ethylene dimerization at 50 °C and 42 bar.[223] It was hypothesized that a catalytically essential Ru−H species is generated via thermal defect engineering by heating the framework at 300 °C under a nitrogen atmosphere. The same species can be generated in higher concentrations by heating the framework at 150 °C under a hydrogen atmosphere or by incorporating defect-inducing ligands. Under optimized condition, activities as high as 200 mol C_4/(mol Ru·h) and mean lifetimes above 120 h (extrapolated) can be achieved. The selectivity for 1-butene scales negatively with conversion but is high across a decent range: 100% at 0% conversion (extrapolated) and 80% at 6% conversion. Importantly, the authors found that the rate of catalyst deactivation, which occurs by the irreversible binding of oligomer byproducts, shows an accelerated decrease with increased ethylene pressure and becomes essentially 0 and ethylene pressures equal to or above 40% of the ethylene saturation pressure in the MOF. This effect was attributed to intrapore liquid ethylene accumulation through capillary condensation.

Looking at the polymerization of ethylene, Park et al. explored solvent-free ethylene polymerization with Cr(III)-MFU-4l (Figure 11).[224] Notably, the use of Cr, an early

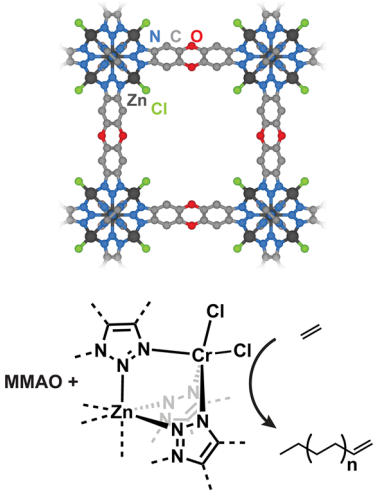

Figure 11. Chromium(III) exchanged into MFU-4l catalyzes ethylene polymerization (MMAO = modified methylaluminoxane).[224]

transition metal, favors a higher degree of polymerization products over competitive dimerization products. Inspired by Phillips chromium-oxide catalysts used commercially for high-density polyethylene production, Cr(III) was introduced into the secondary building unit of the parent all-zinc framework through cation exchange and adopted a pseudo-octahedral coordination with 3 nitrogen ligands from the framework and the rest from terminal chloride and solvent molecules. After preactivation with modified methylaluminoxane (MMAO) and removal of solvent, the solid catalyst displayed an activity of 52 000 mol C_2H_4/(mol Cr·h) (ambient temperature, 40 bar), nearly 10-fold higher than the same catalyst operating in slurry phase. The polyethylene produced also had exceptionally low

https://doi.org/10.1021/acs.chemrev.2c00537
Chem. Rev. XXXX, XXX, XXX−XXX

polydispersity index of 1.36, attesting to the single-site nature of this catalyst.

Brønsted acidic sites within MOFs provide a second mechanistic approach for olefin polymerization via carbocation intermediates. One main limitation of the carbocation-mediated olefin dimerization and polymerization strategy is the ability to access the carbocation intermediate as well as its lifetime, both factors being strongly correlated with the carbocation stability. While tertiary (or conjugated) carbocation intermediates can be generated with relative ease and have high enough lifetimes to engage in bimolecular reactions, less stabilized carbocations (i.e., secondary or primary) are generally prohibitively high in energy, diminishing the scope of the carbocation-catalyzed olefin polymerization approach. Still, for the majority of industrial reactions involving a zeolite, the zeolite acts as an acid catalyst.[225,226] Naturally, many have wondered if MOFs, with their well-defined and tunable acid sites, can catalyze the same reactions more effectively, such as at lower reaction temperatures and/or with higher selectivities. MIL-100 and MIL-101 have been extensively studied for their Lewis acidity due to the coordinatively unsaturated trivalent metal site in the $[M_3O(RCO_2)_6]^+$ cluster. The Lewis and Brønsted acidity were probed with IR spectroscopy coupled with CO, CD_3CN, and pyridine adsorption. Strong Lewis acidity was identified at the 5-coordinated metal sites within fully dehydrated MIL-100(M) (M = Al, Fe, Cr) in the order (Al > Fe ∼ Cr). Medium Brønsted acidity was found for partially hydrated samples at metal-bound H_2O ligands, whose Δ(O−H) upon dosing of CO are 160 cm^{-1} (M = Cr) and 191 cm^{-1} (M = Al).[227−229]

A strategy used to increase the Brønsted acidity of MOFs is the incorporation of protic functional groups. Inspired by the Brønsted superacidity of sulfated zirconia,[230] Yaghi and co-workers installed hydrosulfate onto the zirconium oxo cluster of MOF-808 to synthesize MOF-808-SO_4.[231] The acidity of the sulfated MOF-808 was determined to be slightly higher than pure sulfuric acid, based on solid-state ^{31}P NMR of adsorbed trimethylphosphine oxide, $Me_3P{=}O$, thus making it a superacid. The structure of MOF-808-SO_4 was determined using single-crystal X-ray diffraction and powder neutron diffraction, and the source of the superacidity was determined to be a terminal aqua hydrogen bonded to a κO,κO-chelating sulfate based on solid-state NMR and DFT computation.[232] The material was found to catalyze the isobutene dimerization in a gas−solid flow setup with good selectivity (>90% C_8 up to 160 °C) and better activity than benchmark catalysts at low temperatures (<200 °C) (Figure 12). The catalyst was later shown to be competent for carbenium-based isomerization and oligomerization of a range of light olefins (C_4−C_6) at relatively low temperature (100 °C) with reaction outcome highly dependent on the olefin. One of the deactivation pathways was found to be desorption of the Brønsted acidic water, which could be regenerated by a high temperature water vapor treatment.[233] Nevertheless, these works demonstrated the benefit of translating catalysis on metal oxides into SBUs of MOFs, such as active site elucidation and improved performance at lower temperature.

3.3.2. Isomerization Reactions. As in the case of the olefin oligo/polymerization, olefin isomerization can also occur through two main mechanisms: either a metal-catalyzed pathway involving metal−alkyl intermediates, or, more commonly, an acid-catalyzed pathway involving carbocation intermediates (Table 8).

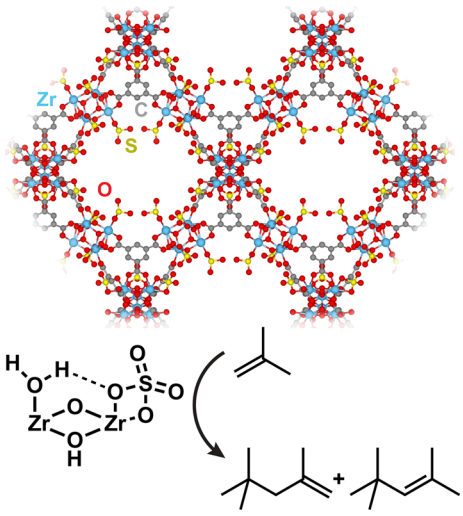

Figure 12. Superacidity of MOF-808-SO_4 catalyzes the dimerization of isobutene.[232]

In 2013, researchers from the Kitagawa group reported La-BTTc (BTTc = benzene-1,3,5-tris(2-thiophene-5-carboxylate)) and measured its Lewis acidity at the monometallic La centers by ammonia temperature-programmed desorption (NH_3-TPD) and IR spectroscopy (monitoring the red-shift of ν(C═O) of adsorbed acetone).[234] They found that the Lewis acidity of La-BTTc is higher than those of MIL-101(Cr) and zeolite H-ZSM-5. The study tested the reactivity of La-BTTc toward 1-hexene but found that there was very little catalytic activity. In 2015, the same group tested the 1-hexene isomerization activity of MOF-76(Yb) at 400 °C under a reaction time of 2 min.[235] The conversion in the presence of the MOF catalyst was noticeably higher: 5.8% compared to 2% in the absence of any catalyst. The selectivity for 1-hexene isomerization in the presence of the MOF-76(Yb) was promising, ∼92%, compared to ∼88% in the absence of any catalyst. The activity of the MOF-76(Yb) catalyst was attributed to its Lewis acidity, which was determined via IR measurements using acetone as probe, and NH_3-TPD, and placed between those of MIL-101(Cr) and La-BTTc.

Sabyrov et al. studied the hydroisomerization of *n*-hexane using MIL-101(Cr) as a solid support.[236] To synthesize the catalytically active material, Brønsted acidic phosphotungstic acid (PTA) was first deposited into MIL-101(Cr). The MOF here acts solely as a porous support that allows dispersion of PTA at very high loading of 60% by weight relative to the mass of the total material. Afterward, Pt nanoparticles, which mediate hydrogenation/dehydrogenation, were deposited onto the surface of the MOF. The resulting bifunctional catalyst was highly active for gas-phase hexane hydroisomerization. The Pt nanoparticles dehydrogenate the alkane to form an alkene, which can then be protonated by the PTA Brønsted acid sites to generate a carbocation. The latter can subsequently rearrange, eventually leading to the formation of isoalkanes. At 250 °C and 1 bar, the catalyst generates isohexanes with 100% selectivity and high activity (noting that the selectivity reported for 60% PTA@MIL-101/Pt in Figures 2 and 4 disagree with each other and neither displays 100% selectivity), on the order of 10^{-8} mol/g/s, a 9-fold increase in mass activity compared to traditional aluminosilicate bifunctional catalysts.

https://doi.org/10.1021/acs.chemrev.2c00537
Chem. Rev. XXXX, XXX, XXX−XXX

Table 8. Comparison of Isomerization MOF Catalysts

MOF	reaction conditions	catalyst stability	activity	selectivity	ref
La-BTTc	400 °C, 1-hexene:catalyst ratio not reported, 7 min	crystallinity is preserved after catalysis		2.42% C_{1-5}:21.61% C_6, 73.73% unreacted:2.24% C_{7+} and aromatics	234
MOF-76(Yb)	400 °C, 1-hexene:catalyst = 6:1, 2 min	no *post operando* characterization		0.39% C_{1-5}:5.35% C_6, 94.2% unreacted:0.09% C_{7+} and aromatics	235
no catalyst (reference)	400 °C, 2 min, 1-hexene			0.18% C_{1-5}:1.77% C_6, 98.0% unreacted:0.08% C_{7+} and aromatics	235
PTA@MIL-101/Pt	1 bar, 250 °C, 16 sccm H2, 1.2 mL/h *n*-hexane	activity decreases over time, possibly due to coking; crystallinity is preserved and some porosity is lost after catalysis	~10.0×10^{-8} mol/g/s for isomerization	distribution of C_6 alkanes not reported	236
$0.9PW_{12}$@NU-1000	250 °C, 1 bar, 10 sccm *o*-xylene/Ar, 10 sccm H_2	conversion decreases and selectivity remains constant with time on stream; crystallinity lost after catalysis	0.16 mol/mol(W)/h	17% isomerization and 83% disproportionation	237
WO_x-ZrO_2 (reference)	250 °C, 1 bar, 10 sccm *o*-xylene/Ar, 10 sccm H_2	conversion decreases with time on stream due to coking, can be regenerated at 300 °C	0.11 mol/mol(W)/h	100% isomerization	237
Rh(1)BF_4@Mn(bdpdmpm)	1 bar 1-butene, 46 °C	activity retained after 5 cycles; crystallinity retained after catalysis	$TOF^{90\%}$ = 1845 h^{-1}	reaches thermodynamic limit (98% 2-butene) after 9 min	141

Similarly, PTA-impregnated NU-1000, a Zr based MOF with Zr-oxo cluster SBUs, was found to be active in the rather demanding *o*-xylene isomerization/disproportionation reaction, which requires protonation of xylene. Tungstanated zirconia, WO_x-ZrO_2, known to catalyze challenging reactions such as alkane isomerizations, alcohol dehydrations, etherifications, and xylene isomerizations, was used as a control material. Compared to WO_x-ZrO_2, the initial activity of PTA-NU-1000 at 250 °C was slightly higher and the selectivity profile was quite different. In particular, PTA-NU-1000 was much more active than WO_x-ZrO_2 toward *o*-xylene disproportionation (i.e., the formation of one equivalent of toluene and one equivalent of trimethylbenzene from 2 equiv of *o*-xylene). The activity of the MOF catalyst, however, gradually decreases over time (i.e., its activity drops to 60% of its initial value after 200 min). Coking and pore collapse were ruled out for this. The authors instead suggested irreversible formation of strongly bound catalyst−substrate complexes as the reason for the observed decrease in activity.[237] It has also been reported that acidic MOFs promote the alkylation of benzene with ethanol at lower temperatures (100−200 °C) than zeolites (>350 °C). Although the nature of the acid sites in these MOFs was not elucidated, this reaction likely proceeds through a mechanism that is related to *o*-xylene isomerization and disproportionation.[238,239]

Metal sites capable of engaging C−H bonds in oxidative addition reactions can also catalyze the isomerization of terminal alkenes to internal alkenes. The catalyst designed by Peralta et al. by incorporating Rh(I) into the dipyrazole binding pocket of the framework Mn(bcpdmpm) (bcpdmpm^{2-} = bis(4-carboxyphenyl-3,5-dimethyl-pyrazol-1-yl)methane), discussed in section 3.1.1, for its alkene hydrogenation activity, also displays high activity toward alkene isomerization.[141] The suggested mechanism for this reaction involves the coordination of the alkene to the Rh(I) metal center, the activation of the allylic C−H bond in an oxidative addition reaction to form a Rh(III)-allyl anion intermediate, and a reductive elimination step with the formation of a new C−H bond and a new alkene product. The reaction studied was the isomerization of 1-butene to 2-butene. Notably, this is a thermodynamically favorable reaction, as *E*-2-butene is lower in energy by ~1.3 kcal/mol than 1-butene, and *Z*-2-butene is, in turn, ~0.7 kcal/mol lower in energy than *E*-2-butene. Therefore, at equilibrium, 1-butene should account for ~2% among all isomers. Indeed, Peralta et al. observed that 1-butene in the presence of the MOF-supported [Rh(ethylene)$_2$]BF_4 species quickly isomerizes to 2-butenes. At 46 °C, 1 bar, and 2 mol % Rh loading, the relative ratio of 1-butene in the gaseous mixture decreases to the thermodynamic 2% value within 9 min. Similarly to the hydrogenation reaction, the activity of the catalyst is inhibited by chloride anions; MOF-supported [Rh(ethylene)$_2$]Cl species only shows a 19% conversion of 1-butene over the course of 9 h. The authors attributed this observation to chloride's ability to stabilize the Rh(III) intermediate, which decreases the TOF of the catalyst, based on computational studies as well as formation of an IR-observable Rh hydride species in the presence of chloride.

3.3.3. Carbonylation Reactions. Transition metal-catalyzed carbon monoxide insertion is a vital reaction for the generation of carboxylic acid and derivatives such as lactones, acyl halides, and amides (Table 9).[240] For instance, the dominant route for the production of acetic acid is through carbonylation of methanol. This reaction is typically catalyzed

https://doi.org/10.1021/acs.chemrev.2c00537
Chem. Rev. XXXX, XXX, XXX−XXX

Table 9. Comparison of Carbonylation MOF Catalysts

MOF	reaction conditions	catalyst stability	activity	ref
$Rh(CO)_2$@Mn-bcpdmpm	0.95 bar MeBr, 9.4 bar CO, 25−120 °C	crystallinity preserved after catalysis	TON = 11 (10 h), TOF ∼ 1 mol(acetyl bromide)/mol/h at 120 °C	243
$Co(CO)_4$@Cr-MIL-101	20 bar CO, 0.05% propylene oxide, 70 °C, flow rate = 120 mL/min	crystallinity preserved after catalysis; activity decreases with time on stream	TON = 60 (24 h), TOF ∼ 6 mol(β-butyrolactone)/mol(Co)/h	246
$(PtCl_2)_2$@ $CaCu_6[(S,S)\text{-methox}]_3(OH)_2(H_2O)$	4 bar CO, 2 bar NH_3	no *post operando* characterization	TON = 25, TOF = 612 mol(NH_4CN)/mol/h	248
$(Pt_2)_{0.5}(PtCl_2)$@ $CaCu_6[(S,S)\text{-methox}]_3(OH)_2(H_2O)$	4 bar CO, 2 bar NH_3	activity retained for 10 h on stream; no *post operando* characterization	TON = 56, TOF = 1260 mol(NH_4CN)/mol/h	248

by a homogeneous noble metal catalyst, such as Rh for the Monsanto process and Ir for the Cativa process.[241]

The Doonan and Sumby groups have probed the mechanism for Rh-catalyzed carbonylation of methyl halides to generate acetyl halides through single-crystal X-ray diffraction. Postsynthetic installation of $[Rh(CO)_2]^+$ units into the binding pocket of the dipyrazole linker of $[Mn_3L_2L']$ (L and L′ = bis(4-(4-carboxyphenyl)-1*H*-3,5-dimethylpyrazolyl)methane, where the ligand has two crystallographically unique orientations) yields a framework analogous to homogeneous catalysts, with the added benefit of site isolation.[242] Exposure of the framework to MeBr in acetonitrile leads to carbonyl insertion and the formation of the MOF-supported $[Rh(CH_3CN)_2(COMe)Br]^+$ species. Further exposure to 10 bar of 1:9 MeBr:CO at 120 °C results in catalytic formation of MeCOBr (TON = 11).[243] Interestingly, this catalytic reaction does not proceed in acetonitrile, presumably due to low CO solubility in this solvent. The reaction also stalls with MeI, which is attributed to the larger size of iodide, preventing the *cis*−*trans* isomerization and subsequent reductive elimination. In both cases, single-crystal structures of the acetyl intermediate provide unprecedented mechanistic insight and highlight the advantage conferred by MOFs in mechanistic studies.

The carbonylation of epoxides is an emerging method to produce β-lactones, which has been restricted to homogeneous catalysis until recently. In solution, epoxide carbonylation catalysts typically consist of a Lewis acid and $Co(CO)_4^-$.[244,245] Park et al. utilized the Lewis acidic site in MIL-101(Cr) and constructed the first heterogeneous epoxide carbonylation catalyst (Figure 13). They demonstrated that under 20 bar total pressure (0.02% propylene oxide in CO, 125 mL/min) at 70 °C, the catalyst $Co(CO)_4$⊂Cr-MIL-101 is capable of 60 turnovers after 24 h.[246] Even higher turnover number (1300) was achieved using the same catalyst in liquid flow for the related carbonylation reaction of β-butyrolactone to succinic anhydride.[247]

More recently, Mon et al. discovered that Pt(0) deposited in the MOF $CaCu_6[(S,S)\text{-methox}]_3(OH)_2(H_2O)$ ((*S*,*S*)-methoxH$_4$ = *N*,*N*-oxalyldimethionine) can catalyze gas-phase condensation of CO and NH_3 to NH_4CN, which they proposed to occur via carbonylation of Pt-NH_3.[248] This framework features one-dimensional channels decorated with thioethers. Pt(0) was introduced by impregnating the MOF with K_2PtCl_4 and reduction with $NaBH_4$. Through a combination of single-crystal XRD, AC-HAADF-STEM, and XPS, they determined that Pt(0) and Pt(II) coexist in the framework. Pt(II) likely persists after reduction due to lack of accessibility, while the accessible Pt(0) forms a Pt_2 dimer bound by a single thioether ligand. We note that the low occupancy (0.1667) and disorder of guest molecules likely prevented accurate determination of the local structure. Nevertheless, the MOF catalyzes at room temperature the condensation of CO and NH_3 as a gas−solid reaction with a total TON of 56 after 10 h. The unreduced Pt(II)-containing MOF also catalyzes the same reaction, albeit with lower TON of 25.

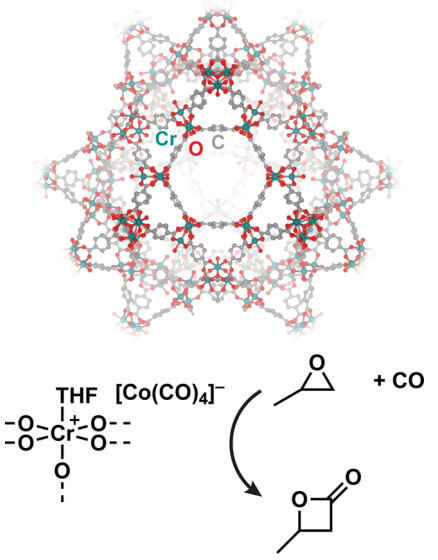

Figure 13. MIL-101 exchanged with a noncoordinating anion facilitates the carbonylation of epoxides to β-lactones.[246]

3.4. Other Gas−Solid MOF-Catalyzed Reactions

Hydrolysis of organophosphate chemical warfare agent (CWA) is another example of a Lewis acid catalyzed reaction.[249] Most studies on MOF-catalyzed CWA hydrolysis are conducted in buffered aqueous solution, but recently interest has arisen in solid-state hydrolysis using atmospheric moisture, which is more suitable for filters and personal protection.[250] Wang et al. were the first to test solid-state hydrolysis with MOFs.[251] Specifically, a series of MOFs with Zr_6 nodes (NU-1000, UiO-66, and UiO-66-NH_2) were mixed with CWAs or CWA simulants under controlled relative humidity, and the hydrolysis was monitored by digestion and ^{1}H NMR. The solid-state reactions were found to be uniformly much slower compared to reactions in buffered solutions, which was attributed to catalyst poisoning by the hydrolysis product and potentially the reduced (catalytically competent) defect formation that normally occurs in buffered solution. The relative activity of the three MOFs tested was also found to be different from previous solution-based results but lack of particle size control precluded detailed analysis.

https://doi.org/10.1021/acs.chemrev.2c00537
Chem. Rev. XXXX, XXX, XXX−XXX

Another reaction that proceeds via an acid-generated carbocation intermediate is the alcohol dehydration reaction. Hasan et al. attached sulfonic acid functional groups onto the ligand of MIL-101(Cr) and demonstrated its improved catalytic activity in the 2-butanol dehydration reaction which is proposed to occur through the aforementioned mechanism.[252] The sulfonic acid version, MIL-101(Cr)-SO_3H, was active at 225 °C, whereas regular MIL-101(Cr) showed little activity even at 250 °C. The activity of MIL-101(Cr)-SO_3H is stable for 24 h on stream.

4. SUMMARY AND OUTLOOK

The potential utility of MOFs particularly in heterogeneous catalysis involving small substrates is underlined by tremendous recent progress in gas−solid reactivity studies involving these materials. This survey of the current landscape of gas−solid reactivity in MOFs reveals that the majority of reports to date have been inspired and modeled after catalysis on traditional heterogeneous supports like metal oxides and silica. In such cases, the binding environment of the catalytic active metal center is often not predetermined, and a distribution of sites are observed as a result. The generation of active catalysts by means of intrinsically less defined processes such as autoreduction or pyrolytic defect generation further convolutes the study of the active site. In contrast, in the limited cases where a dedicated metal-binding site is present, the structure of the active site is often much more predictable. The performance of the resulting catalyst, often superior to its solution counterpart, can be correlated to a set of defined parameters, thus providing guidelines for rational design and improvement. Therefore, there is an exciting opportunity in transforming molecular catalysts into catalysts operating at the gas−solid interface through creative MOF design. We would like to note, however, that if MOFs are to become state-of-the-art catalysts with real industrial value, further investigations are necessary to find more active, more stable, and more cost-effective materials.

Operating at the verge of traditional molecular and bulk solid catalysis could bring about new concepts that are not known or have not been demonstrated in conventional systems. One example is the use of Lewis acidic sites in MOFs as universal anion abstractors and, subsequently, as anchoring sites for cationic catalytic species. While a similar concept has been demonstrated with methylaluminoxane ($(Al(CH_3)O)_n$, MAO) immobilized on silica,[253,254] no well-defined Lewis acidic sites in MOFs have been examined for this purpose despite the relatively large number of MOFs that present such sites.

Similarly, the use of Lewis acid−base pairs anchored on the rigid MOF platform could open up a vast landscape of heterogeneous catalysis which has not yet been explored in depth. Among the examples discussed herein, Shakya et al. proposed that their Rh(II)-carboxylate framework, discussed in more detail in section 3.1.1, catalyzes the hydrogenation of propene to propane by the initial dissociation of the carboxylate ligand from the Rh(II) center followed by the heterolytic splitting of H_2 by the two separated ions, to form a carboxylic acid-Rh(II) hydride intermediate.[144] Similarly, Desai et al. suggested that the Ga−Rh(I)-grafted MOF, discussed in more detail in section 3.1.2, catalyzes the hydrogenation of propyne to propene by the initial dissociation of a pyridine ligand from the Rh(I) center followed by the heterolytic splitting of H_2, to form a pyridinium cation-Rh(I) hydride intermediate.[151] Both hydrogenation examples are reminiscent of the way nature has been suggested to split H_2 in hydrogenase enzymes, whereby a ligand-based amine group and an Fe(I) active site act as a frustrated Lewis pair (FLP).[255] Relevantly, this strategy is now well-established in homogeneous systems employing sterically crowded phosphine−borane pairs to heterolyze H_2,[256,257] and subsequently engage in catalytic hydrogenation of weak, polarized bonds such as imines, enamines, silyl ethers, α,β-enones, ynones, *N*-alkylanilines, as well as the partial hydrogenation of alkynes to alkenes.[257−259] The FLP strategy has been extended with homogeneous systems to enable enantioselective hydrogenation,[260] as well as activate other small molecules, such as CO_2 and N_2O, and functional groups, including carbon−carbon π bonds (in alkynes, alkenes, and conjugated dienes), strained carbon−carbon σ bonds, sulfur−sulfur bonds[261] In other words, the concept of Lewis acid−base pairs promoting reactivity has been studied extensively and shown to be very versatile. Site isolation in MOFs allows, with judicious framework design, for the generation of FLPs comprised of metal nodes and linkers or postsynthetically installed functional groups. MOFs should offer an alternative, highly modular platform for the design and study of FLP-catalyzed reactions in the gas phase, perhaps by analogy with Lewis acid−base pairs in MOFs that have already been used for the design of carbon capture materials.[262] We note that the catalytic activity of FLPs within MOFs has already been demonstrated in a number of cases in the presence of solvent for several reactions, including CO_2 fixation and imine hydrogenation.[263−265]

In a different context, the abundance of multinuclear SBUs in MOFs provides an excellent platform for exploring multicenter, multielectron activation and reactivity of small molecule substrates such as dioxygen or dinitrogen, a long-lasting interest in molecular chemistry.[266] As discussed in section 3.2.1, we find that the use of dioxygen as an oxygen atom source in controlled oxygenation reactions has been sparse due to the limited number of systems designed to promote multielectron reactivity. This stems primarily from the research focus on single-metal units within MOFs which are usually capable of upward to 2-electron transfer, as evidenced by some of the hydrogenation, olefin polymerization, and olefin isomerization reactions discussed previously. Judicious design of well-defined multimetallic, redox-active cluster SBUs within MOFs capable to cooperatively reduce O_2 by 4 electrons could lead to improved performance in alkane oxygenation catalysis. Likewise, the development of multimetallic, redox-active cluster SBUs could also promote the much sought-after multielectron N_2 reduction to ammonia or organic nitrogen-containing compounds.

On a more critical note, we would like to emphasize the necessity for thorough characterization of MOF catalysts, both before and after catalytic reactions. A clear comparison is necessary to determine if any MOF decomposition occurs, which may produce other active catalysts such as metal oxides. At the very minimum, we would advise that all catalysts be cycled multiple times/run on stream for as long as possible and that diffraction be measured after cycling. We further suggest that other *post operando* characterizations such as gas isotherms, thermogravimetric analysis, and EXAFS are performed (to determine if any coking or coking-like processes occur, as well as if the local structure about the metal sites drastically changes). We further recommend in situ character-

https://doi.org/10.1021/acs.chemrev.2c00537
Chem. Rev. XXXX, XXX, XXX−XXX

ization or mechanistic studies if possible, in order to help elucidate the true active site, as the active site may not always be the assumed sites (i.e., defects or surface sites may drive reactivity). For the mechanistic studies, we also suggest that pressure dependence of rate and particle size dependence of rate are both studied to determine whether the reaction is rate limited by the intrinsic kinetics of the reaction of interest or by diffusion. If the reaction is diffusion limited, then measures should be tested to lift the limitation, such as running the reaction in flow rather than batch or decreasing particle sizes. Finally, we suggest that researchers probe the mechanism and kinetics of MOF-catalyzed using isotope labeling experiments when possible.[114,267]

A potential advantage and a line of future research for MOFs is the possibility of using secondary coordination sphere interactions to influence catalysis. Taking advantage of the modular, well-defined three-dimensional structure around the MOF active site, moieties could be installed in the vicinity of MOF active sites to serve as hemilabile stabilizing ligands, temporary proton shuttles, or H-bond partners to modulate the selectivity and activity of the active site through cooperative activation or colocalization of reaction partners. Functionally, this allows the secondary coordination sphere of MOFs to mimic the behavior of metalloenzyme cofactors, where the environment around the activity is often crucial for defining both selectivity and activity. Relatedly, MOF catalysts have yet to take full advantage of the geometry of the host structure. Systematic structure−function studies whereby the same catalyst is installed in multiple frameworks of varying pore size, shape, hydrophobicity, and Lewis acidity will be critical for this purpose. Surveying the literature, we find that a broad trend in the field of MOF catalysis is the relative lack of detailed kinetic studies that are much more common with homogeneous systems. While many reports comment on the kinetics governing MOF catalysis (e.g., kinetic isotope effects, rate-determining steps), the data presented is often unstandardized. This is also in part due to the difficulty of accurately measuring the concentration of active sites in MOFs, especially in the case of the deposition of catalytic units inside the pores, which leads to difficulties in calculating accurate TON values. Therefore, more systematic and standardized ways of measuring catalytic performance for MOFs should be implemented. Nevertheless, heterogeneous MOF catalysis is an emergent, fast-evolving field promising an expansive landscape of underexplored transformations, both by translating molecular catalysis onto better-performing, well-defined, solid supports and by providing opportunities for new transformations unaffected by solvent-mediated decomposition pathways.

AUTHOR INFORMATION

Corresponding Author

Mircea Dincă − *Department of Chemistry, Massachusetts Institute of Technology, Cambridge, Massachusetts 02139, United States*; Email: mdinca@mit.edu

Authors

Andrei Iliescu − *Department of Chemistry, Massachusetts Institute of Technology, Cambridge, Massachusetts 02139, United States*

Julius J. Oppenheim − *Department of Chemistry, Massachusetts Institute of Technology, Cambridge, Massachusetts 02139, United States*; orcid.org/0000-0002-5988-0677

Chenyue Sun − *Department of Chemistry, Massachusetts Institute of Technology, Cambridge, Massachusetts 02139, United States*

Complete contact information is available at: https://pubs.acs.org/10.1021/acs.chemrev.2c00537

Author Contributions

‡A.I., J.J.O., and C.S. contributed equally to this work. CRediT: **Andrei Iliescu** writing-original draft, writing-review & editing; **Julius Oppenheim** writing-original draft, writing-review & editing; **Chenyue Sun** writing-original draft, writing-review & editing; **Mircea Dincă** supervision, writing-review & editing.

Notes

The authors declare no competing financial interest.

Biographies

Andrei Iliescu is a Ph.D. student in Mircea Dincă's group at MIT. His current research focuses on postsynthetic modifications of metal−organic frameworks to target multielectron transformations. He received his A.B. in Chemistry in 2020 from Harvard University, where he worked with Theodore Betley on the isolation and study of reactive intermediates using coordinatively unsaturated copper complexes.

Julius J. Oppenheim is a Ph.D. student in Mircea Dincă's group at MIT. His current research focuses on the reactivity of site-isolated low valent metals in metal−organic frameworks. He received his B.Sc. in Chemistry in 2019 from the California Institute of Technology, where he worked with William A. Goddard III on the development of polarizable force fields.

Chenyue Sun was a graduate student in the Dincă group. He received his B.Sc. from University of Hong Kong before joining the Dincă group in 2016. His work is centered around discovering new porous materials as well as new reactivities enabled by porous materials. He received his Ph.D. in 2021 and worked as a postdoctoral associate in the Coates group at Cornell. Currently, Chenyue works for ExxonMobil in Texas.

Mircea Dincă is a Professor of Chemistry and the W. M. Keck Professor of Energy at MIT. His group's research focuses on the reactivity of small molecules facilitated by the unusual metal geometries enforced with metal−organic frameworks. He finds that the study of the fundamental reaction pathways leads to interesting new catalysts, including that for ethylene dimerization/polymerization, the Guerbet reaction, NO disproportionation, hydrocarbon and carbon monoxide oxidation, β-lactone and epoxide carbonylation, olefin cyclopropanation, olefin epoxidation, and the oxygen reduction reaction. He was educated at Princeton University (A.B. in Chemistry, 2003) and UC Berkeley (Ph.D. in Inorganic Chemistry, 2008).

ACKNOWLEDGMENTS

Work on small molecule reactivity and catalysis in the Dincă lab is currently supported by the National Science Foundation (Alan T. Waterman Award to M.D.: DMR-1645232) and by the Dow Chemical Company.

REFERENCES

(1) Kim, S.; Loose, F.; Chirik, P. J. Beyond Ammonia: Nitrogen-Element Bond Forming Reactions with Coordinated Dinitrogen. *Chem. Rev.* **2020**, *120*, 5637−5681.

(2) Que, L.; Tolman, W. B. Biologically Inspired Oxidation Catalysis. *Nature* **2008**, *455*, 333−340.
(3) Cavaliere, V. N.; Wicker, B. F.; Mindiola, D. J. Homogeneous Organometallic Chemistry of Methane. In *Advances in Organometallic Chemistry*; Hill, A. F., Fink, M. J., Eds.; Academic Press, 2012; Vol *60*, Chapter 1, pp 1−47.
(4) Forrest, S. J. K.; Schluschaß, B.; Yuzik-Klimova, E. Y.; Schneider, S. Nitrogen Fixation via Splitting into Nitrido Complexes. *Chem. Rev.* **2021**, *121*, 6522−6587.
(5) Milani, B.; Licini, G.; Clot, E.; Albrecht, M. Small Molecule Activation. *Dalton Trans.* **2016**, *45*, 14419−14420.
(6) Cokoja, M.; Bruckmeier, C.; Rieger, B.; Herrmann, W. A.; Kühn, F. E. Transformation of Carbon Dioxide with Homogeneous Transition-Metal Catalysts. *Angew. Chem., Int. Ed.* **2011**, *50*, 8510−8537.
(7) Seyler, C.; Capello, C.; Hellweg, S.; Bruder, C.; Bayne, D.; Huwiler, A.; Hungerbühler, K. Waste-Solvent Management as an Element of Green Chemistry. *Ind. Eng. Chem. Res.* **2006**, *45*, 7700−7709.
(8) Chen, Z.; Concepcion, J. J.; Hu, X.; Yang, W.; Hoertz, P. G.; Meyer, T. J. Concerted O Atom-Proton Transfer in the O—O Bond Forming Step in Water Oxidation. *Proc. Natl. Acad. Sci. U. S. A.* **2010**, *107*, 7225−7229.
(9) Furukawa, H.; Cordova, K. E.; O'Keeffe, M.; Yaghi, O. M. The Chemistry and Applications of Metal-Organic Frameworks. *Science* **2013**, *341*, 1230444.
(10) Kalmutzki, M. J.; Hanikel, N.; Yaghi, O. M. Secondary Building Units as the Turning Point in the Development of the Reticular Chemistry of MOFs. *Sci. Adv.* **2018**, *4*, No. eaat9180.
(11) Morozan, A.; Jaouen, F. Metal Organic Frameworks for Electrochemical Applications. *Energy Environ. Sci.* **2012**, *5*, 9269−9290.
(12) Hod, I.; Sampson, M. D.; Deria, P.; Kubiak, C. P.; Farha, O. K.; Hupp, J. T. Fe-Porphyrin-Based Metal-Organic Framework Films as High-Surface Concentration, Heterogeneous Catalysts for Electrochemical Reduction of CO_2. *ACS Catal.* **2015**, *5*, 6302−6309.
(13) Bloch, E. D.; Britt, D.; Lee, C.; Doonan, C. J.; Uribe-Romo, F. J.; Furukawa, H.; Long, J. R.; Yaghi, O. M. Metal Insertion in a Microporous Metal-Organic Framework Lined with 2,2′-Bipyridine. *J. Am. Chem. Soc.* **2010**, *132*, 14382−14384.
(14) Fateeva, A.; Chater, P. A.; Ireland, C. P.; Tahir, A. A.; Khimyak, Y. Z.; Wiper, P. V.; Darwent, J. R.; Rosseinsky, M. J. A Water-Stable Porphyrin-Based Metal-Organic Framework Active for Visible-Light Photocatalysis. *Angew. Chem., Int. Ed.* **2012**, *51*, 7440−7444.
(15) Denysenko, D.; Jelic, J.; Reuter, K.; Volkmer, D. Postsynthetic Metal and Ligand Exchange in MFU-4l. *Chem. - Eur. J.* **2015**, *21*, 8188−8199.
(16) Comito, R. J.; Wu, Z.; Zhang, G.; Lawrence, J. A.; Korzyński, M. D.; Kehl, J. A.; Miller, J. T.; Dincă, M. Stabilized Vanadium Catalyst for Olefin Polymerization by Site Isolation in a Metal-Organic Framework. *Angew. Chem., Int. Ed.* **2018**, *57*, 8135−8139.
(17) Sun, C.; Skorupskii, G.; Dou, J.-H.; Wright, A. M.; Dincă, M. Reversible Metalation and Catalysis with a Scorpionate-like Metallo-Ligand in a Metal-Organic Framework. *J. Am. Chem. Soc.* **2018**, *140*, 17394−17398.
(18) Healy, C.; Patil, K. M.; Wilson, B. H.; Hermanspahn, L.; Harvey-Reid, N. C.; Howard, B. I.; Kleinjan, C.; Kolien, J.; Payet, F.; Telfer, S. G.; et al. The Thermal Stability of Metal-Organic Frameworks. *Coord. Chem. Rev.* **2020**, *419*, 213388.
(19) Wang, W.; Sharapa, D. I.; Chandresh, A.; Nefedov, A.; Heißler, S.; Heinke, L.; Studt, F.; Wang, Y.; Wöll, C. Interplay of Electronic and Steric Effects to Yield Low-Temperature CO Oxidation at Metal Single Sites in Defect-Engineered HKUST-1. *Angew. Chem., Int. Ed.* **2020**, *59*, 10514−10518.
(20) Burgess, S. A.; Kassie, A.; Baranowski, S. A.; Fritzsching, K. J.; Schmidt-Rohr, K.; Brown, C. M.; Wade, C. R. Improved Catalytic Activity and Stability of a Palladium Pincer Complex by Incorporation into a Metal-Organic Framework. *J. Am. Chem. Soc.* **2016**, *138*, 1780−1783.
(21) Wang, C.; An, B.; Lin, W. Metal-Organic Frameworks in Solid-Gas Phase Catalysis. *ACS Catal.* **2019**, *9*, 130−146.
(22) Johnson, B. A.; Ott, S. Diagnosing Surface versus Bulk Reactivity for Molecular Catalysis within Metal-Organic Frameworks Using a Quantitative Kinetic Model. *Chem. Sci.* **2020**, *11*, 7468−7478.
(23) Kärger, J.; Freude, D. Mass Transfer in Micro- and Mesoporous Materials. *Chem. Eng. Technol.* **2002**, *25*, 769−778.
(24) Jennings, S. G. The Mean Free Path in Air. *J. Aerosol Sci.* **1988**, *19*, 159−166.
(25) Deng, H.; Grunder, S.; Cordova, K. E.; Valente, C.; Furukawa, H.; Hmadeh, M.; Gándara, F.; Whalley, A. C.; Liu, Z.; Asahina, S.; et al. Large-Pore Apertures in a Series of Metal-Organic Frameworks. *Science* **2012**, *336*, 1018−1023.
(26) Férey, G.; Mellot-Draznieks, C.; Serre, C.; Millange, F.; Dutour, J.; Surblé, S.; Margiolaki, I. A Chromium Terephthalate-Based Solid with Unusually Large Pore Volumes and Surface Area. *Science* **2005**, *309*, 2040−2042.
(27) Fogler, H. S. *Essentials of Chemical Reaction Engineering*; Prentice Hall, 2017.
(28) Satterfield, C. N. *Mass Transfer in Heterogeneous Catalysis*; MIT Press: Cambridge, MA, 1969.
(29) Wang, R.; Bukowski, B. C.; Duan, J.; Sheridan, T. R.; Atilgan, A.; Zhang, K.; Snurr, R. Q.; Hupp, J. T. Investigating the Process and Mechanism of Molecular Transport within a Representative Solvent-Filled Metal-Organic Framework. *Langmuir* **2020**, *36*, 10853−10859.
(30) Do, D. D. *Adsorption Analysis: Equilibria And Kinetics (With Cd Containing Computer Matlab Programs)*; World Scientific, 1998.
(31) Burada, P. S.; Hänggi, P.; Marchesoni, F.; Schmid, G.; Talkner, P. Diffusion in Confined Geometries. *ChemPhysChem* **2009**, *10*, 45−54.
(32) Hahn, K.; Kärger, J.; Kukla, V. Single-File Diffusion Observation. *Phys. Rev. Lett.* **1996**, *76*, 2762−2765.
(33) Zhao, Z.; Li, X.; Huang, S.; Xia, Q.; Li, Z. Adsorption and Diffusion of Benzene on Chromium-Based Metal Organic Framework MIL-101 Synthesized by Microwave Irradiation. *Ind. Eng. Chem. Res.* **2011**, *50*, 2254−2261.
(34) Lee, H.; Chi, W. S.; Lee, M. J.; Zhang, K.; Edhaim, F.; Mizrahi Rodriguez, K.; DeWitt, S. J. A.; Smith, Z. P. Network-Nanostructured ZIF-8 to Enable Percolation for Enhanced Gas Transport. *Adv. Funct. Mater.* **2022**, *32*, 2207775.
(35) Karge, H. G.; Nießen, W. A New Method for the Study of Diffusion and Counter-Diffusion in Zeolites. *Catal. Today* **1991**, *8*, 451−465.
(36) Stejskal, E. O.; Tanner, J. E. Spin Diffusion Measurements. *J. Chem. Phys.* **1965**, *42*, 288−292.
(37) Forse, A. C.; Gonzalez, M. I.; Siegelman, R. L.; Witherspoon, V. J.; Jawahery, S.; Mercado, R.; Milner, P. J.; Martell, J. D.; Smit, B.; Blümich, B.; et al. Unexpected Diffusion Anisotropy of Carbon Dioxide in the Metal-Organic Framework Zn_2(dobpdc). *J. Am. Chem. Soc.* **2018**, *140*, 1663−1673.
(38) Singh, U. K.; Vannice, M. A. Kinetics of Liquid-Phase Hydrogenation Reactions over Supported Metal Catalysts — a Review. *Appl. Catal. Gen.* **2001**, *213*, 1−24.
(39) Madon, R. J.; Boudart, M. Experimental Criterion for the Absence of Artifacts in the Measurement of Rates of Heterogeneous Catalytic Reactions. *Ind. Eng. Chem. Fundam.* **1982**, *21*, 438−447.
(40) Gascon, J.; Aktay, U.; Hernandez-Alonso, M. D.; van Klink, G. P. M.; Kapteijn, F. Amino-Based Metal-Organic Frameworks as Stable, Highly Active Basic Catalysts. *J. Catal.* **2009**, *261*, 75−87.
(41) Pérez-Ramírez, J.; Christensen, C. H.; Egeblad, K.; Christensen, C. H.; Groen, J. C. Hierarchical Zeolites. *Chem. Soc. Rev.* **2008**, *37*, 2530−2542.
(42) Colwell, K. A.; Jackson, M. N.; Torres-Gavosto, R. M.; Jawahery, S.; Vlaisavljevich, B.; Falkowski, J. M.; Smit, B.; Weston, S. C.; Long, J. R. Buffered Coordination Modulation as a Means of Controlling Crystal Morphology and Molecular Diffusion in an Anisotropic Metal-Organic Framework. *J. Am. Chem. Soc.* **2021**, *143*, 5044−5052.

https://doi.org/10.1021/acs.chemrev.2c00537
Chem. Rev. XXXX, XXX, XXX−XXX

(43) Gao, W.-Y.; Cardenal, A. D.; Wang, C.-H.; Powers, D. C. In Operando Analysis of Diffusion in Porous Metal-Organic Framework Catalysts. *Chem. - Eur. J.* **2019**, *25*, 3465−3476.
(44) Brunner, E. Solubility of Hydrogen in 10 Organic Solvents at 298.15, 323.15, and 373.15 K. *J. Chem. Eng. Data* **1985**, *30*, 269−273.
(45) Goettmann, F.; Sanchez, C. How Does Confinement Affect the Catalytic Activity of Mesoporous Materials? *J. Mater. Chem.* **2007**, *17*, 24−30.
(46) Derouane, E. G.; Andre, J.-M.; Lucas, A. A. Surface Curvature Effects in Physisorption and Catalysis by Microporous Solids and Molecular Sieves. *J. Catal.* **1988**, *110*, 58−73.
(47) Venuto, P. B. Organic Catalysis over Zeolites. *Microporous Mater.* **1994**, *2*, 297−411.
(48) Langmuir, I. THE ADSORPTION OF GASES ON PLANE SURFACES OF GLASS, MICA AND PLATINUM. *J. Am. Chem. Soc.* **1918**, *40*, 1361−1403.
(49) Rouquerol, J.; Rouquerol, F.; Sing, K. S. W. *Adsorption by Powders and Porous Solids: Principles, Methodology and Applications*; Elsevier, 1998.
(50) Jiang, Z.-R.; Wang, H.; Hu, Y.; Lu, J.; Jiang, H.-L. Polar Group and Defect Engineering in a Metal-Organic Framework. *ChemSusChem* **2015**, *8*, 878−885.
(51) Xiao, D. J.; Oktawiec, J.; Milner, P. J.; Long, J. R. Pore Environment Effects on Catalytic Cyclohexane Oxidation in Expanded Fe_2(dobdc) Analogues. *J. Am. Chem. Soc.* **2016**, *138*, 14371−14379.
(52) Gelb, L. D.; Gubbins, K. E.; Radhakrishnan, R.; Sliwinska-Bartkowiak, M. Phase Separation in Confined Systems. *Rep. Prog. Phys.* **1999**, *62*, 1573−1659.
(53) Gregg, S. J.; Sing, K. S. W. *Adsorption, Surface Area, and Porosity*; Academic Press: London, New York, 1982.
(54) Agirrezabal-Telleria, I.; Iglesia, E. Stabilization of Active, Selective, and Regenerable Ni-Based Dimerization Catalysts by Condensation of Ethene Withinordered Mesopores. *J. Catal.* **2017**, *352*, 505−514.
(55) Agirrezabal-Telleria, I.; Iglesia, E. Mechanistic Insights and Consequences of Intrapore Liquids in Ethene, Propene, and Butene Dimerization on Isolated Ni^{2+} Sites Grafted within Aluminosilicate Mesopores. *J. Catal.* **2020**, *389*, 690−705.
(56) Soubeyrand-Lenoir, E.; Vagner, C.; Yoon, J. W.; Bazin, P.; Ragon, F.; Hwang, Y. K.; Serre, C.; Chang, J.-S.; Llewellyn, P. L. How Water Fosters a Remarkable 5-Fold Increase in Low-Pressure CO_2 Uptake within Mesoporous MIL-100(Fe). *J. Am. Chem. Soc.* **2012**, *134*, 10174−10181.
(57) Clauzier, S.; Ho, L. N.; Pera-Titus, M.; Coasne, B.; Farrusseng, D. Enhanced H_2 Uptake in Solvents Confined in Mesoporous Metal-Organic Framework. *J. Am. Chem. Soc.* **2012**, *134*, 17369−17371.
(58) Ho, L. N.; Clauzier, S.; Schuurman, Y.; Farrusseng, D.; Coasne, B. Gas Uptake in Solvents Confined in Mesopores. *J. Phys. Chem. Lett.* **2013**, *4*, 2274−2278.
(59) Peureux, J.; Torres, M.; Mozzanega, H.; Giroir-Fendler, A.; Dalmon, J.-A. Nitrobenzene Liquid-Phase Hydrogenation in a Membrane Reactor. *Catal. Today* **1995**, *25*, 409−415.
(60) Coasne, B.; Farrusseng, D. Gas Oversolubility in Nanoconfined Liquids. *Microporous Mesoporous Mater.* **2019**, *288*, 109561.
(61) Liu, C.-C.; Mou, C.-Y.; Yu, S. S.-F.; Chan, S. I. Heterogeneous Formulation of the Tricopper Complex for Efficient Catalytic Conversion of Methane into Methanol at Ambient Temperature and Pressure. *Energy Environ. Sci.* **2016**, *9*, 1361−1374.
(62) Metzger, E. D.; Brozek, C. K.; Comito, R. J.; Dincă, M. Selective Dimerization of Ethylene to 1-Butene with a Porous Catalyst. *ACS Cent. Sci.* **2016**, *2*, 148−153.
(63) Roux, B.; Yu, H. Ai.; Karplus, M. Molecular Basis for the Born Model of Ion Solvation. *J. Phys. Chem.* **1990**, *94*, 4683−4688.
(64) Uppili, S.; Thomas, K. J.; Crompton, E. M.; Ramamurthy, V. Probing Zeolites with Organic Molecules. *Langmuir* **2000**, *16*, 265−274.
(65) Deye, J. F.; Berger, T. A.; Anderson, A. G. Nile Red as a Solvatochromic Dye for Measuring Solvent Strength in Normal Liquids and Mixtures of Normal Liquids with Supercritical and near Critical Fluids. *Anal. Chem.* **1990**, *62*, 615−622.
(66) Corma, A.; Iborra, S.; Rodrıguez, I.; Sánchez, F. Immobilized Proton Sponge on Inorganic Carriers. *J. Catal.* **2002**, *211*, 208−215.
(67) Derouane, E. G. Zeolites as Solid Solvents. *J. Mol. Catal. Chem.* **1998**, *134*, 29−45.
(68) Gounder, R.; Iglesia, E. The Roles of Entropy and Enthalpy in Stabilizing Ion-Pairs at Transition States in Zeolite Acid Catalysis. *Acc. Chem. Res.* **2012**, *45*, 229−238.
(69) Raja, R.; Thomas, J. M.; Jones, M. D.; Johnson, B. F. G.; Vaughan, D. E. W. Constraining Asymmetric Organometallic Catalysts within Mesoporous Supports Boosts Their Enantioselectivity. *J. Am. Chem. Soc.* **2003**, *125*, 14982−14983.
(70) Rieth, A. J.; Hunter, K. M.; Dincă, M.; Paesani, F. Hydrogen Bonding Structure of Confined Water Templated by a Metal-Organic Framework with Open Metal Sites. *Nat. Commun.* **2019**, *10*, 4771.
(71) Bates, J. S.; Bukowski, B. C.; Greeley, J.; Gounder, R. Structure and Solvation of Confined Water and Water-Ethanol Clusters within Microporous Brønsted Acids and Their Effects on Ethanol Dehydration Catalysis. *Chem. Sci.* **2020**, *11*, 7102−7122.
(72) Paolucci, C.; Khurana, I.; Parekh, A. A.; Li, S.; Shih, A. J.; Li, H.; Di Iorio, J. R.; Albarracin-Caballero, J. D.; Yezerets, A.; Miller, J. T.; et al. Dynamic Multinuclear Sites Formed by Mobilized Copper Ions in NOx Selective Catalytic Reduction. *Science* **2017**, *357*, 898−903.
(73) Haw, J. F.; Xu, T.; Nicholas, J. B.; Goguen, P. W. Solvent-Assisted Proton Transfer in Catalysis by Zeolite Solid Acids. *Nature* **1997**, *389*, 832−835.
(74) Mondal, S.; Bagchi, B. Water in Carbon Nanotubes. *J. Phys. Chem. Lett.* **2019**, *10*, 6287−6292.
(75) Zecchina, A.; Scarano, D.; Bordiga, S.; Spoto, G.; Lamberti, C. Surface Structures of Oxides and Halides and Their Relationships to Catalytic Properties. *Adv. Catal.* **2001**, *46*, 265−397.
(76) Jiang, J.; Yaghi, O. M. Brønsted Acidity in Metal-Organic Frameworks. *Chem. Rev.* **2015**, *115*, 6966−6997.
(77) Zhu, L.; Liu, X.-Q.; Jiang, H.-L.; Sun, L.-B. Metal-Organic Frameworks for Heterogeneous Basic Catalysis. *Chem. Rev.* **2017**, *117*, 8129−8176.
(78) Zecchina, A.; Lamberti, C.; Bordiga, S. Surface Acidity and Basicity. *Catal. Today* **1998**, *41*, 169−177.
(79) Gusev, D. G.; Ozerov, O. V. Calculated Hydride and Fluoride Affinities of a Series of Carbenium and Silylium Cations in the Gas Phase and in C_6H_5Cl Solution. *Chem. - Eur. J.* **2011**, *17*, 634−640.
(80) Bartmess, J. E. Negative Ion Energetics Data. In *NIST Chemistry WebBook, NIST Standard Reference Database Number 69, Eds. P.J. Linstrom and W.G. Mallard*; Linstrom, P. J., Mallard, W. G., Eds.; National Institute of Standards and Technology: Gaithersburg MD, 1997; p 20899.
(81) Busca, G. Bases and Basic Materials in Chemical and Environmental Processes. Liquid versus Solid Basicity. *Chem. Rev.* **2010**, *110*, 2217−2249.
(82) Haag, W. O.; Lago, R. M.; Weisz, P. B. The Active Site of Acidic Aluminosilicate Catalysts. *Nature* **1984**, *309*, 589−591.
(83) Haag, W. O. Catalysis by Zeolites—Science and Technology. In *Studies in Surface Science and Catalysis*; Weitkamp, J., Karge, H. G., Pfeifer, H., Hölderich, W., Eds.; *Zeolites and Related Microporous Materials: State of the Art 1994 - Proceedings of the 10th International Zeolite Conference, Garmisch-Partenkirchen, Germany, 17−22 July 1994*; Elsevier, 1994; Vol *84*, pp 1375−1394.
(84) Bordiga, S.; Lamberti, C.; Bonino, F.; Travert, A.; Thibault-Starzyk, F. Probing Zeolites by Vibrational Spectroscopies. *Chem. Soc. Rev.* **2015**, *44*, 7262−7341.
(85) Gorte, R. J.; White, D. Interactions of Chemical Species with Acid Sites in Zeolites. *Top. Catal.* **1997**, *4*, 57−69.
(86) Zheng, A.; Li, S.; Liu, S.-B.; Deng, F. Acidic Properties and Structure-Activity Correlations of Solid Acid Catalysts Revealed by Solid-State NMR Spectroscopy. *Acc. Chem. Res.* **2016**, *49*, 655−663.
(87) Farneth, W. E.; Gorte, R. J. Methods for Characterizing Zeolite Acidity. *Chem. Rev.* **1995**, *95*, 615−635.

https://doi.org/10.1021/acs.chemrev.2c00537
Chem. Rev. XXXX, XXX, XXX−XXX

(88) Boronat, M.; Corma, A. What Is Measured When Measuring Acidity in Zeolites with Probe Molecules? *ACS Catal.* **2019**, *9*, 1539−1548.
(89) Derouane, E. G.; Védrine, J. C.; Pinto, R. R.; Borges, P. M.; Costa, L.; Lemos, M. A. N. D. A.; Lemos, F.; Ribeiro, F. R. The Acidity of Zeolites. *Catal. Rev.* **2013**, *55*, 454−515.
(90) Lavalley, J. C. Infrared Spectrometric Studies of the Surface Basicity of Metal Oxides and Zeolites Using Adsorbed Probe Molecules. *Catal. Today* **1996**, *27*, 377−401.
(91) Drake, T.; Ji, P.; Lin, W. Site Isolation in Metal-Organic Frameworks Enables Novel Transition Metal Catalysis. *Acc. Chem. Res.* **2018**, *51*, 2129−2138.
(92) Young, R. J.; Huxley, M. T.; Pardo, E.; Champness, N. R.; Sumby, C. J.; Doonan, C. J. Isolating Reactive Metal-Based Species in Metal-Organic Frameworks - Viable Strategies and Opportunities. *Chem. Sci.* **2020**, *11*, 4031−4050.
(93) Wang, Y.; Wöll, C. Chemical Reactions at Isolated Single-Sites Inside Metal-Organic Frameworks. *Catal. Lett.* **2018**, *148*, 2201−2222.
(94) Zhang, X.; Llabrés i Xamena, F. X.; Corma, A. Gold(III) - Metal Organic Framework Bridges the Gap between Homogeneous and Heterogeneous Gold Catalysts. *J. Catal.* **2009**, *265*, 155−160.
(95) Hecht, H. G. The Interpretation of Diffuse Reflectance Spectra. *J. Res. Natl. Bur. Stand. Sect. Phys. Chem.* **1976**, *80A*, 567.
(96) Hadjiivanov, K. I.; Panayotov, D. A.; Mihaylov, M. Y.; Ivanova, E. Z.; Chakarova, K. K.; Andonova, S. M.; Drenchev, N. L. Power of Infrared and Raman Spectroscopies to Characterize Metal-Organic Frameworks and Investigate Their Interaction with Guest Molecules. *Chem. Rev.* **2021**, *121*, 1286−1424.
(97) Bonino, F.; Lamberti, C.; Bordiga, S. IR and Raman Spectroscopies Probing MOFs Structure, Defectivity, and Reactivity. In *The Chemistry of Metal−Organic Frameworks*; John Wiley & Sons, Ltd, 2016; pp 657−690.
(98) Brozek, C. K.; Miller, J. T.; Stoian, S. A.; Dincă, M. NO Disproportionation at a Mononuclear Site-Isolated Fe^{2+} Center in Fe^{2+}-MOF-5. *J. Am. Chem. Soc.* **2015**, *137*, 7495−7501.
(99) Sun, C.; Yang, L.; Ortuño, M. A.; Wright, A. M.; Chen, T.; Head, A. R.; López, N.; Dincă, M. Spectroscopic Evidence of Hyponitrite Radical Intermediate in NO Disproportionation at a MOF-Supported Mononuclear Copper Site. *Angew. Chem., Int. Ed.* **2021**, *60*, 7845−7850.
(100) Baek, J.; Rungtaweevoranit, B.; Pei, X.; Park, M.; Fakra, S. C.; Liu, Y.-S.; Matheu, R.; Alshmimri, S. A.; Alshehri, S.; Trickett, C. A.; et al. Bioinspired Metal-Organic Framework Catalysts for Selective Methane Oxidation to Methanol. *J. Am. Chem. Soc.* **2018**, *140*, 18208−18216.
(101) Bloch, E. D.; Murray, L. J.; Queen, W. L.; Chavan, S.; Maximoff, S. N.; Bigi, J. P.; Krishna, R.; Peterson, V. K.; Grandjean, F.; Long, G. J.; et al. Selective Binding of O_2 over N_2 in a Redox-Active Metal-Organic Framework with Open Iron(II) Coordination Sites. *J. Am. Chem. Soc.* **2011**, *133*, 14814−14822.
(102) Anderson, J. S.; Gallagher, A. T.; Mason, J. A.; Harris, T. D. A Five-Coordinate Heme Dioxygen Adduct Isolated within a Metal-Organic Framework. *J. Am. Chem. Soc.* **2014**, *136*, 16489−16492.
(103) Sholl, D. S.; Lively, R. P. Defects in Metal-Organic Frameworks. *J. Phys. Chem. Lett.* **2015**, *6*, 3437−3444.
(104) Xiang, W.; Zhang, Y.; Chen, Y.; Liu, C.; Tu, X. Synthesis, Characterization and Application of Defective Metal-Organic Frameworks. *J. Mater. Chem. A* **2020**, *8*, 21526−21546.
(105) Fang, Z.; Bueken, B.; De Vos, D. E.; Fischer, R. A. Defect-Engineered Metal-Organic Frameworks. *Angew. Chem., Int. Ed.* **2015**, *54*, 7234−7254.
(106) Fang, Z.; Ju, Q. Role of Defects in Catalysis. In *Metal−Organic Frameworks*; John Wiley & Sons, Ltd, 2018; pp 341−378.
(107) Ravon, U.; Savonnet, M.; Aguado, S.; Domine, M. E.; Janneau, E.; Farrusseng, D. Engineering of Coordination Polymers for Shape Selective Alkylation of Large Aromatics and the Role of Defects. *Microporous Mesoporous Mater.* **2010**, *129*, 319−329.
(108) Vermoortele, F.; Bueken, B.; Le Bars, G.; Van de Voorde, B.; Vandichel, M.; Houthoofd, K.; Vimont, A.; Daturi, M.; Waroquier, M.; Van Speybroeck, V.; et al. Synthesis Modulation as a Tool To Increase the Catalytic Activity of Metal-Organic Frameworks. *J. Am. Chem. Soc.* **2013**, *135*, 11465−11468.
(109) Wu, H.; Chua, Y. S.; Krungleviciute, V.; Tyagi, M.; Chen, P.; Yildirim, T.; Zhou, W. Unusual and Highly Tunable Missing-Linker Defects in Zirconium Metal-Organic Framework UiO-66 and Their Important Effects on Gas Adsorption. *J. Am. Chem. Soc.* **2013**, *135*, 10525−10532.
(110) DeStefano, M. R.; Islamoglu, T.; Garibay, S. J.; Hupp, J. T.; Farha, O. K. Room-Temperature Synthesis of UiO-66 and Thermal Modulation of Densities of Defect Sites. *Chem. Mater.* **2017**, *29*, 1357−1361.
(111) Klet, R. C.; Liu, Y.; Wang, T. C.; Hupp, J. T.; Farha, O. K. Evaluation of Brønsted Acidity and Proton Topology in Zr- and Hf-Based Metal-Organic Frameworks Using Potentiometric Acid-Base Titration. *J. Mater. Chem. A* **2016**, *4*, 1479−1485.
(112) Wang, J.; Liu, L.; Chen, C.; Dong, X.; Wang, Q.; Alfilfil, L.; AlAlouni, M. R.; Yao, K.; Huang, J.; Zhang, D.; et al. Engineering Effective Structural Defects of Metal-Organic Frameworks to Enhance Their Catalytic Performances. *J. Mater. Chem. A* **2020**, *8*, 4464−4472.
(113) Idrees, K. B.; Chen, Z.; Zhang, X.; Mian, M. R.; Drout, R. J.; Islamoglu, T.; Farha, O. K. Tailoring Pore Aperture and Structural Defects in Zirconium-Based Metal-Organic Frameworks for Krypton/Xenon Separation. *Chem. Mater.* **2020**, *32*, 3776−3782.
(114) Wang, C.-H.; Gao, W.-Y.; Powers, D. C. Measuring and Modulating Substrate Confinement during Nitrogen-Atom Transfer in a Ru2-Based Metal-Organic Framework. *J. Am. Chem. Soc.* **2019**, *141*, 19203−19207.
(115) Dissegna, S.; Hardian, R.; Epp, K.; Kieslich, G.; Coulet, M.-V.; Llewellyn, P.; Fischer, R. A. Using Water Adsorption Measurements to Access the Chemistry of Defects in the Metal-Organic Framework UiO-66. *CrystEngComm* **2017**, *19*, 4137−4141.
(116) Valenzano, L.; Civalleri, B.; Chavan, S.; Bordiga, S.; Nilsen, M. H.; Jakobsen, S.; Lillerud, K. P.; Lamberti, C. Disclosing the Complex Structure of UiO-66 Metal Organic Framework. *Chem. Mater.* **2011**, *23*, 1700−1718.
(117) Xu, R.; Ji, Q.; Zhao, P.; Jian, M.; Xiang, C.; Hu, C.; Zhang, G.; Tang, C.; Liu, R.; Zhang, X.; et al. Hierarchically Porous UiO-66 with Tunable Mesopores and Oxygen Vacancies for Enhanced Arsenic Removal. *J. Mater. Chem. A* **2020**, *8*, 7870−7879.
(118) Cirujano, F. G.; Llabrés i Xamena, F. X. Tuning the Catalytic Properties of UiO-66 Metal-Organic Frameworks. *J. Phys. Chem. Lett.* **2020**, *11*, 4879−4890.
(119) Gentile, F. S.; Pannico, M.; Causà, M.; Mensitieri, G.; Di Palma, G.; Scherillo, G.; Musto, P. Metal Defects in HKUST-1 MOF Revealed by Vibrational Spectroscopy. *J. Mater. Chem. A* **2020**, *8*, 10796−10812.
(120) Xue, Z.; Liu, K.; Liu, Q.; Li, Y.; Li, M.; Su, C.-Y.; Ogiwara, N.; Kobayashi, H.; Kitagawa, H.; Liu, M.; et al. Missing-Linker Metal-Organic Frameworks for Oxygen Evolution Reaction. *Nat. Commun.* **2019**, *10*, 5048.
(121) Liu, L.; Chen, Z.; Wang, J.; Zhang, D.; Zhu, Y.; Ling, S.; Huang, K.-W.; Belmabkhout, Y.; Adil, K.; Zhang, Y.; et al. Imaging Defects and Their Evolution in a Metal-Organic Framework at Sub-Unit-Cell Resolution. *Nat. Chem.* **2019**, *11*, 622−628.
(122) Cliffe, M. J.; Wan, W.; Zou, X.; Chater, P. A.; Kleppe, A. K.; Tucker, M. G.; Wilhelm, H.; Funnell, N. P.; Coudert, F.-X.; Goodwin, A. L. Correlated Defect Nanoregions in a Metal-Organic Framework. *Nat. Commun.* **2014**, *5*, 4176.
(123) Shearer, G. C.; Chavan, S.; Bordiga, S.; Svelle, S.; Olsbye, U.; Lillerud, K. P. Defect Engineering. *Chem. Mater.* **2016**, *28*, 3749−3761.
(124) Xiao, B.; Byrne, P. J.; Wheatley, P. S.; Wragg, D. S.; Zhao, X.; Fletcher, A. J.; Thomas, K. M.; Peters, L.; Evans, J. S. O.; Warren, J. E.; et al. Chemically Blockable Transformation and Ultraselective Low-Pressure Gas Adsorption in a Non-Porous Metal Organic Framework. *Nat. Chem.* **2009**, *1*, 289−294.

https://doi.org/10.1021/acs.chemrev.2c00537
Chem. Rev. XXXX, XXX, XXX−XXX

(125) Shöâeè, M.; Agger, J. R.; Anderson, M. W.; Attfield, M. P. Crystal Form, Defects and Growth of the Metal Organic Framework HKUST-1 Revealed by Atomic Force Microscopy. *CrystEngComm* **2008**, *10*, 646−648.
(126) Ameloot, R.; Vermoortele, F.; Hofkens, J.; De Schryver, F. C.; De Vos, D. E.; Roeffaers, M. B. J. Three-Dimensional Visualization of Defects Formed during the Synthesis of Metal-Organic Frameworks. *Angew. Chem., Int. Ed.* **2013**, *52*, 401−405.
(127) Kang, X.; Lyu, K.; Li, L.; Li, J.; Kimberley, L.; Wang, B.; Liu, L.; Cheng, Y.; Frogley, M. D.; Rudić, S.; et al. Integration of Mesopores and Crystal Defects in Metal-Organic Frameworks via Templated Electrosynthesis. *Nat. Commun.* **2019**, *10*, 4466.
(128) Kočiřík, M.; Struve, P.; Fiedler, K.; Bülow, M. A Model for the Mass-Transfer Resistance at the Surface of Zeolite Crystals. *J. Chem. Soc. Faraday Trans. 1 Phys. Chem. Condens. Phases* **1988**, *84*, 3001−3013.
(129) Arya, G.; Maginn, E. J.; Chang, H.-C. Effect of the Surface Energy Barrier on Sorbate Diffusion in AlPO4−5. *J. Phys. Chem. B* **2001**, *105*, 2725−2735.
(130) Hibbe, F.; Chmelik, C.; Heinke, L.; Pramanik, S.; Li, J.; Ruthven, D. M.; Tzoulaki, D.; Kärger, J. The Nature of Surface Barriers on Nanoporous Solids Explored by Microimaging of Transient Guest Distributions. *J. Am. Chem. Soc.* **2011**, *133*, 2804−2807.
(131) Chmelik, C.; Hibbe, F.; Tzoulaki, D.; Heinke, L.; Caro, J.; Li, J.; Kärger, J. Exploring the Nature of Surface Barriers on MOF Zn(Tbip) by Applying IR Microscopy in High Temporal and Spatial Resolution. *Microporous Mesoporous Mater.* **2010**, *129*, 340−344.
(132) Chase, M. W., Jr. JANAF thermochemical tables. *J. Phys. Chem. Ref Data* **1998**, *9*, 1−1951 Data Reported in NIST Standard Reference Database 69, June 2005 Release: NIST Chemistry WebBook.
(133) Rimoldi, M.; Nakamura, A.; Vermeulen, N. A.; Henkelis, J. J.; Blackburn, A. K.; Hupp, J. T.; Stoddart, J. F.; Farha, O. K. A Metal-Organic Framework Immobilised Iridium Pincer Complex. *Chem. Sci.* **2016**, *7*, 4980−4984.
(134) Yang, D.; Odoh, S. O.; Borycz, J.; Wang, T. C.; Farha, O. K.; Hupp, J. T.; Cramer, C. J.; Gagliardi, L.; Gates, B. C. Tuning Zr6Metal-Organic Framework (MOF) Nodes as Catalyst Supports. *ACS Catal.* **2016**, *6*, 235−247.
(135) Yang, D.; Odoh, S. O.; Wang, T. C.; Farha, O. K.; Hupp, J. T.; Cramer, C. J.; Gagliardi, L.; Gates, B. C. Metal-Organic Framework Nodes as Nearly Ideal Supports for Molecular Catalysts. *J. Am. Chem. Soc.* **2015**, *137*, 7391−7396.
(136) Yang, D.; Gaggioli, C. A.; Conley, E.; Babucci, M.; Gagliardi, L.; Gates, B. C. Synthesis and Characterization of Tetrairidium Clusters in the Metal Organic Framework UiO-67. *J. Catal.* **2020**, *382*, 165−172.
(137) Li, Z.; Peters, A. W.; Liu, J.; Zhang, X.; Schweitzer, N. M.; Hupp, J. T.; Farha, O. K. Size Effect of the Active Sites in UiO-66-Supported Nickel Catalysts Synthesized via Atomic Layer Deposition for Ethylene Hydrogenation. *Inorg. Chem. Front.* **2017**, *4*, 820−824.
(138) Li, Z.; Schweitzer, N. M.; League, A. B.; Bernales, V.; Peters, A. W.; Getsoian, A. B.; Wang, T. C.; Miller, J. T.; Vjunov, A.; Fulton, J. L.; et al. Sintering-Resistant Single-Site Nickel Catalyst Supported by Metal-Organic Framework. *J. Am. Chem. Soc.* **2016**, *138*, 1977−1982.
(139) Liu, J.; Li, Z.; Zhang, X.; Otake, K.; Zhang, L.; Peters, A. W.; Young, M. J.; Bedford, N. M.; Letourneau, S. P.; Mandia, D. J.; et al. Introducing Nonstructural Ligands to Zirconia-like Metal-Organic Framework Nodes To Tune the Activity of Node-Supported Nickel Catalysts for Ethylene Hydrogenation. *ACS Catal.* **2019**, *9*, 3198−3207.
(140) Bernales, V.; Yang, D.; Yu, J.; Gümüşlü, G.; Cramer, C. J.; Gates, B. C.; Gagliardi, L. Molecular Rhodium Complexes Supported on the Metal-Oxide-Like Nodes of Metal Organic Frameworks and on Zeolite HY. *ACS Appl. Mater. Interfaces* **2017**, *9*, 33511−33520.
(141) Peralta, R. A.; Huxley, M. T.; Evans, J. D.; Fallon, T.; Cao, H.; He, M.; Zhao, X. S.; Agnoli, S.; Sumby, C. J.; Doonan, C. J. Highly Active Gas Phase Organometallic Catalysis Supported Within Metal-Organic Framework Pores. *J. Am. Chem. Soc.* **2020**, *142*, 13533−13543.
(142) Grigoropoulos, A.; McKay, A. I.; Katsoulidis, A. P.; Davies, R. P.; Haynes, A.; Brammer, L.; Xiao, J.; Weller, A. S.; Rosseinsky, M. J. Encapsulation of Crabtree's Catalyst in Sulfonated MIL-101(Cr). *Angew. Chem., Int. Ed.* **2018**, *57*, 4532−4537.
(143) Babucci, M.; Hoffman, A. S.; Bare, S. R.; Gates, B. C. Characterization of a Metal-Organic Framework Zr6O8 Node-Supported Atomically Dispersed Iridium Catalyst for Ethylene Hydrogenation by X-Ray Absorption Near-Edge Structure and Infrared Spectroscopies. *J. Phys. Chem. C* **2021**, *125*, 16995−17007.
(144) Shakya, D. M.; Ejegbavwo, O. A.; Rajeshkumar, T.; Senanayake, S. D.; Brandt, A. J.; Farzandh, S.; Acharya, N.; Ebrahim, A. M.; Frenkel, A. I.; Rui, N.; et al. Selective Catalytic Chemistry at Rhodium(II) Nodes in Bimetallic Metal-Organic Frameworks. *Angew. Chem., Int. Ed.* **2019**, *58*, 16533−16537.
(145) Schbib, N. S.; García, M. A.; Gígola, C. E.; Errazu, A. F. Kinetics of Front-End Acetylene Hydrogenation in Ethylene Production. *Ind. Eng. Chem. Res.* **1996**, *35*, 1496−1505.
(146) Borodziński, A.; Bond, G. C. Selective Hydrogenation of Ethyne in Ethene-Rich Streams on Palladium Catalysts. Part 1. Effect of Changes to the Catalyst During Reaction. *Catal. Rev.* **2006**, *48*, 91−144.
(147) Zhang, L.; Zhou, M.; Wang, A.; Zhang, T. Selective Hydrogenation over Supported Metal Catalysts. *Chem. Rev.* **2020**, *120*, 683−733.
(148) Studt, F.; Abild-Pedersen, F.; Bligaard, T.; Sørensen, R. Z.; Christensen, C. H.; Nørskov, J. K. Identification of Non-Precious Metal Alloy Catalysts for Selective Hydrogenation of Acetylene. *Science* **2008**, *320*, 1320−1322.
(149) Tejeda-Serrano, M.; Mon, M.; Ross, B.; Gonell, F.; Ferrando-Soria, J.; Corma, A.; Leyva-Pérez, A.; Armentano, D.; Pardo, E. Isolated Fe(III)-O Sites Catalyze the Hydrogenation of Acetylene in Ethylene Flows under Front-End Industrial Conditions. *J. Am. Chem. Soc.* **2018**, *140*, 8827−8832.
(150) Ji, S.; Chen, Y.; Zhao, S.; Chen, W.; Shi, L.; Wang, Y.; Dong, J.; Li, Z.; Li, F.; Chen, C.; et al. Atomically Dispersed Ruthenium Species Inside Metal-Organic Frameworks. *Angew. Chem., Int. Ed.* **2019**, *58*, 4271−4275.
(151) Desai, S. P.; Ye, J.; Zheng, J.; Ferrandon, M. S.; Webber, T. E.; Platero-Prats, A. E.; Duan, J.; Garcia-Holley, P.; Camaioni, D. M.; Chapman, K. W.; et al. Well-Defined Rhodium-Gallium Catalytic Sites in a Metal-Organic Framework. *J. Am. Chem. Soc.* **2018**, *140*, 15309−15318.
(152) Guan, B.; Zhan, R.; Lin, H.; Huang, Z. Review of State of the Art Technologies of Selective Catalytic Reduction of NOx from Diesel Engine Exhaust. *Appl. Therm. Eng.* **2014**, *66*, 395−414.
(153) Smolders, S.; Jacobsen, J.; Stock, N.; De Vos, D. Selective Catalytic Reduction of NO by Cerium-Based Metal-Organic Frameworks. *Catal. Sci. Technol.* **2020**, *10*, 337−341.
(154) Zhang, X.; Shen, B.; Zhang, X.; Wang, F.; Chi, G.; Si, M. A Comparative Study of Manganese-Cerium Doped Metal-Organic Frameworks Prepared via Impregnation and in Situ Methods in the Selective Catalytic Reduction of NO. *RSC Adv.* **2017**, *7*, 5928−5936.
(155) Liu, Y.; Zhao, J.; Lee, J.-M. Conventional and New Materials for Selective Catalytic Reduction (SCR) of NOx. *ChemCatChem.* **2018**, *10*, 1499−1511.
(156) Jiang, H.; Wang, Q.; Wang, H.; Chen, Y.; Zhang, M. MOF-74 as an Efficient Catalyst for the Low-Temperature Selective Catalytic Reduction of NOx with NH3. *ACS Appl. Mater. Interfaces* **2016**, *8*, 26817−26826.
(157) Wang, P.; Zhao, H.; Sun, H.; Yu, H.; Chen, S.; Quan, X. Porous Metal-Organic Framework MIL-100(Fe) as an Efficient Catalyst for the Selective Catalytic Reduction of NO_x with NH_3. *RSC Adv.* **2014**, *4*, 48912−48919.
(158) Zhang, W.; Shi, Y.; Li, C.; Zhao, Q.; Li, X. Synthesis of Bimetallic MOFs MIL-100(Fe-Mn) as an Efficient Catalyst for

https://doi.org/10.1021/acs.chemrev.2c00537
Chem. Rev. XXXX, XXX, XXX−XXX

Selective Catalytic Reduction of NO_x with NH_3. *Catal. Lett.* **2016**, *146*, 1956−1964.
(159) Zhang, M.; Wang, W.; Chen, Y. Theoretical Investigation of Selective Catalytic Reduction of NO on MIL-100-Fe. *Phys. Chem. Chem. Phys.* **2018**, *20*, 2211−2219.
(160) Jiang, H.; Zhou, J.; Wang, C.; Li, Y.; Chen, Y.; Zhang, M. Effect of Cosolvent and Temperature on the Structures and Properties of Cu-MOF-74 in Low-Temperature NH_3-SCR. *Ind. Eng. Chem. Res.* **2017**, *56*, 3542−3550.
(161) Zhang, M.; Gu, K.; Huang, X.; Chen, Y. A DFT Study on the Effect of Oxygen Vacancies and H2O in Mn-MOF-74 on SCR Reactions. *Phys. Chem. Chem. Phys.* **2019**, *21*, 19226−19233.
(162) *Rankings about Energy in the World*; U.S. Energy Information Administration (EIA), 2022; https://www.eia.gov/international/data/world (accessed 2022-06-15).
(163) Ravi, M.; Ranocchiari, M.; van Bokhoven, J. A. The Direct Catalytic Oxidation of Methane to Methanol—A Critical Assessment. *Angew. Chem., Int. Ed.* **2017**, *56*, 16464−16483.
(164) Olivos-Suarez, A. I.; Szécsényi, A.; Hensen, E. J. M.; Ruiz-Martinez, J.; Pidko, E. A.; Gascon, J. Strategies for the Direct Catalytic Valorization of Methane Using Heterogeneous Catalysis. *ACS Catal.* **2016**, *6*, 2965−2981.
(165) Xiao, D. J.; Bloch, E. D.; Mason, J. A.; Queen, W. L.; Hudson, M. R.; Planas, N.; Borycz, J.; Dzubak, A. L.; Verma, P.; Lee, K.; et al. Oxidation of Ethane to Ethanol by N_2O in a Metal-Organic Framework with Coordinatively Unsaturated Iron(II) Sites. *Nat. Chem.* **2014**, *6*, 590−595.
(166) Rosen, A. S.; Notestein, J. M.; Snurr, R. Q. Exploring Mechanistic Routes for Light Alkane Oxidation with an Iron-Triazolate Metal-Organic Framework. *Phys. Chem. Chem. Phys.* **2022**, *24*, 8129−8141.
(167) Hall, J. N.; Bollini, P. Low-Temperature, Ambient Pressure Oxidation of Methane to Methanol Over Every Tri-Iron Node in a Metal-Organic Framework Material. *Chem. - Eur. J.* **2020**, *26*, 16639−16643.
(168) Ikuno, T.; Zheng, J.; Vjunov, A.; Sanchez-Sanchez, M.; Ortuño, M. A.; Pahls, D. R.; Fulton, J. L.; Camaioni, D. M.; Li, Z.; Ray, D.; et al. Methane Oxidation to Methanol Catalyzed by Cu-Oxo Clusters Stabilized in NU-1000 Metal-Organic Framework. *J. Am. Chem. Soc.* **2017**, *139*, 10294−10301.
(169) Zheng, J.; Ye, J.; Ortuño, M. A.; Fulton, J. L.; Gutiérrez, O. Y.; Camaioni, D. M.; Motkuri, R. K.; Li, Z.; Webber, T. E.; Mehdi, B. L.; et al. Selective Methane Oxidation to Methanol on Cu-Oxo Dimers Stabilized by Zirconia Nodes of an NU-1000 Metal-Organic Framework. *J. Am. Chem. Soc.* **2019**, *141*, 9292−9304.
(170) Ahn, S.; Nauert, S. L.; Hicks, K. E.; Ardagh, M. A.; Schweitzer, N. M.; Farha, O. K.; Notestein, J. M. Demonstrating the Critical Role of Solvation in Supported Ti and Nb Epoxidation Catalysts via Vapor-Phase Kinetics. *ACS Catal.* **2020**, *10*, 2817−2825.
(171) He, X.; Yang, T.; Iliescu, A.; Arguilla, M.; Chen, T.; Kulik, H.; Dinca, M. Reversible O−O Bond Scission and O2 Evolution at MOF-Supported Tetramanganese Clusters. *ChemRxiv*2022, 2022-14g3n.
(172) Carrero, C. A.; Schloegl, R.; Wachs, I. E.; Schomaecker, R. Critical Literature Review of the Kinetics for the Oxidative Dehydrogenation of Propane over Well-Defined Supported Vanadium Oxide Catalysts. *ACS Catal.* **2014**, *4*, 3357−3380.
(173) Zimmermann, H. Propene. In *Ullmann's Encyclopedia of Industrial Chemistry*; Wiley-VCH, 2013; pp 1−18.
(174) Nguyen, H. G. T.; Schweitzer, N. M.; Chang, C.-Y.; Drake, T. L.; So, M. C.; Stair, P. C.; Farha, O. K.; Hupp, J. T.; Nguyen, S. T. Vanadium-Node-Functionalized UiO-66. *ACS Catal.* **2014**, *4*, 2496−2500.
(175) Li, Z.; Peters, A. W.; Bernales, V.; Ortuño, M. A.; Schweitzer, N. M.; DeStefano, M. R.; Gallington, L. C.; Platero-Prats, A. E.; Chapman, K. W.; Cramer, C. J.; et al. Metal-Organic Framework Supported Cobalt Catalysts for the Oxidative Dehydrogenation of Propane at Low Temperature. *ACS Cent. Sci.* **2017**, *3*, 31−38.
(176) Peters, A. W.; Otake, K.; Platero-Prats, A. E.; Li, Z.; DeStefano, M. R.; Chapman, K. W.; Farha, O. K.; Hupp, J. T. Site-Directed Synthesis of Cobalt Oxide Clusters in a Metal-Organic Framework. *ACS Appl. Mater. Interfaces* **2018**, *10*, 15073−15078.
(177) Li, Z.; Peters, A. W.; Platero-Prats, A. E.; Liu, J.; Kung, C.-W.; Noh, H.; DeStefano, M. R.; Schweitzer, N. M.; Chapman, K. W.; Hupp, J. T.; et al. Fine-Tuning the Activity of Metal-Organic Framework-Supported Cobalt Catalysts for the Oxidative Dehydrogenation of Propane. *J. Am. Chem. Soc.* **2017**, *139*, 15251−15258.
(178) Simons, M. C.; Vitillo, J. G.; Babucci, M.; Hoffman, A. S.; Boubnov, A.; Beauvais, M. L.; Chen, Z.; Cramer, C. J.; Chapman, K. W.; Bare, S. R.; et al. Structure, Dynamics, and Reactivity for Light Alkane Oxidation of Fe(II) Sites Situated in the Nodes of a Metal-Organic Framework. *J. Am. Chem. Soc.* **2019**, *141*, 18142−18151.
(179) Barona, M.; Ahn, S.; Morris, W.; Hoover, W.; Notestein, J. M.; Farha, O. K.; Snurr, R. Q. Computational Predictions and Experimental Validation of Alkane Oxidative Dehydrogenation by Fe_2M MOF Nodes. *ACS Catal.* **2020**, *10*, 1460−1469.
(180) Zhou, Y.; Wang, Z.; Liu, C. Perspective on CO Oxidation over Pd-Based Catalysts. *Catal. Sci. Technol.* **2015**, *5*, 69−81.
(181) Dey, S.; Chandra Dhal, G. Controlling Carbon Monoxide Emissions from Automobile Vehicle Exhaust Using Copper Oxide Catalysts in a Catalytic Converter. *Mater. Today Chem.* **2020**, *17*, 100282.
(182) Ketrat, S.; Maihom, T.; Wannakao, S.; Probst, M.; Nokbin, S.; Limtrakul, J. Coordinatively Unsaturated Metal-Organic Frameworks $M_3(btc)_2$ (M = Cr, Fe, Co, Ni, Cu, and Zn) Catalyzing the Oxidation of CO by N_2O. *Inorg. Chem.* **2017**, *56*, 14005−14012.
(183) Montemore, M. M.; Medlin, J. W. Scaling Relations between Adsorption Energies for Computational Screening and Design of Catalysts. *Catal. Sci. Technol.* **2014**, *4*, 3748−3761.
(184) Jernigan, G. G.; Somorjai, G. A. Carbon Monoxide Oxidation over Three Different Oxidation States of Copper. *J. Catal.* **1994**, *147*, 567−577.
(185) Liu, W.; Flytzani-Stephanopoulos, M. Transition Metal-Promoted Oxidation Catalysis by Fluorite Oxides. *Chem. Eng. J. Biochem. Eng. J.* **1996**, *64*, 283−294.
(186) He, X.; Looker, B. G.; Dinh, K. T.; Stubbs, A. W.; Chen, T.; Meyer, R. J.; Serna, P.; Román-Leshkov, Y.; Lancaster, K. M.; Dincă, M. Cerium(IV) Enhances the Catalytic Oxidation Activity of Single-Site Cu Active Sites in MOFs. *ACS Catal.* **2020**, *10*, 7820−7825.
(187) Abdel-Mageed, A. M.; Rungtaweevoranit, B.; Parlinska-Wojtan, M.; Pei, X.; Yaghi, O. M.; Behm, R. J. Highly Active and Stable Single-Atom Cu Catalysts Supported by a Metal-Organic Framework. *J. Am. Chem. Soc.* **2019**, *141*, 5201−5210.
(188) Yousuf, M. R.; Johnson, E. M.; Maynes, A. J.; Johnston, C. R.; Karim, A. M.; Morris, A. J.; Morris, J. R.; Troya, D. Catalytic CO Oxidation by Cu Single Atoms on the UiO-66 Metal-Organic Framework. *J. Phys. Chem. C* **2022**, *126*, 12507.
(189) Dey, S.; Dhal, G. C. Catalytic Conversion of Carbon Monoxide into Carbon Dioxide over Spinel Catalysts. *Mater. Sci. Energy Technol.* **2019**, *2*, 575−588.
(190) Li, G.; Li, L.; Shi, J.; Yuan, Y.; Li, Y.; Zhao, W.; Shi, J. One-Pot Pyrolytic Synthesis of Mesoporous $MCo_2O_{4(4.5)}$ (M = Mn, Ni, Fe, Cu) Spinels and Its High Efficient Catalytic Properties for CO Oxidation at Low Temperature. *J. Mol. Catal. Chem.* **2014**, *390*, 97−104.
(191) Wang, L. J.; Deng, H.; Furukawa, H.; Gándara, F.; Cordova, K. E.; Peri, D.; Yaghi, O. M. Synthesis and Characterization of Metal-Organic Framework-74 Containing 2, 4, 6, 8, and 10 Different Metals. *Inorg. Chem.* **2014**, *53*, 5881−5883.
(192) Zou, R.-Q.; Sakurai, H.; Xu, Q. Preparation, Adsorption Properties, and Catalytic Activity of 3D Porous Metal-Organic Frameworks Composed of Cubic Building Blocks and Alkali-Metal Ions. *Angew. Chem., Int. Ed.* **2006**, *45*, 2542−2546.
(193) Ahmed, A.; Hodgson, N.; Barrow, M.; Clowes, R.; Robertson, C. M.; Steiner, A.; McKeown, P.; Bradshaw, D.; Myers, P.; Zhang, H. Macroporous Metal-Organic Framework Microparticles with Improved Liquid Phase Separation. *J. Mater. Chem. A* **2014**, *2*, 9085−9090.

https://doi.org/10.1021/acs.chemrev.2c00537
Chem. Rev. XXXX, XXX, XXX−XXX

(194) Noei, H.; Amirjalayer, S.; Müller, M.; Zhang, X.; Schmid, R.; Muhler, M.; Fischer, R. A.; Wang, Y. Low-Temperature CO Oxidation over Cu-Based Metal-Organic Frameworks Monitored by Using FTIR Spectroscopy. *ChemCatChem.* **2012**, *4*, 755−759.
(195) Chen, Y.; Mu, X.; Lester, E.; Wu, T. High Efficiency Synthesis of HKUST-1 under Mild Conditions with High BET Surface Area and CO2 Uptake Capacity. *Prog. Nat. Sci. Mater. Int.* **2018**, *28*, 584−589.
(196) Ye, J.; Liu, C. $Cu_3(BTC)_2$. *Chem. Commun.* **2011**, *47*, 2167−2169.
(197) Su, S.; Zhang, Y.; Zhu, M.; Song, X.; Wang, S.; Zhao, S.; Song, S.; Yang, X.; Zhang, H. An Active-Site-Accessible Porous Metal-Organic Framework Composed of Triangular Building Units. *Chem. Commun.* **2012**, *48*, 11118−11120.
(198) Tu, B.; Pang, Q.; Xu, H.; Li, X.; Wang, Y.; Ma, Z.; Weng, L.; Li, Q. Reversible Redox Activity in Multicomponent Metal-Organic Frameworks Constructed from Trinuclear Copper Pyrazolate Building Blocks. *J. Am. Chem. Soc.* **2017**, *139*, 7998−8007.
(199) Zou, R.-Q.; Sakurai, H.; Han, S.; Zhong, R.-Q.; Xu, Q. Probing the Lewis Acid Sites and CO Catalytic Oxidation Activity of the Porous Metal-Organic Polymer [Cu(5-Methylisophthalate)]. *J. Am. Chem. Soc.* **2007**, *129*, 8402−8403.
(200) Zhao, Y.; Padmanabhan, M.; Gong, Q.; Tsumori, N.; Xu, Q.; Li, J. CO Catalytic Oxidation by a Metal Organic Framework Containing High Density of Reactive Copper Sites. *Chem. Commun.* **2011**, *47*, 6377−6379.
(201) Wang, X.; Zhong, W.; Li, Y. Nanoscale Co-Based Catalysts for Low-Temperature CO Oxidation. *Catal. Sci. Technol.* **2015**, *5*, 1014−1020.
(202) Kim, T.; Kim, D. H.; Kim, S.; Kim, Y. D.; Bae, Y.-S.; Lee, C. Y. Low-Temperature CO Oxidation Using a Metal Organic Framework with Unsaturated Co^{2+} Sites. *Polyhedron* **2015**, *90*, 18−22.
(203) Tan, H.; Liu, C.; Yan, Y.; Wu, J. Simple Preparation of Crystal $Co_3(BTC)_2{\cdot}12H_2O$ and Its Catalytic Activity in CO Oxidation Reaction. *J. Wuhan Univ. Technol.-Mater. Sci. Ed* **2015**, *30*, 71−75.
(204) Lukashuk, L.; Yigit, N.; Rameshan, R.; Kolar, E.; Teschner, D.; Hävecker, M.; Knop-Gericke, A.; Schlögl, R.; Föttinger, K.; Rupprechter, G. Operando Insights into CO Oxidation on Cobalt Oxide Catalysts by NAP-XPS, FTIR, and XRD. *ACS Catal.* **2018**, *8*, 8630−8641.
(205) Yoshida, Y.; Izumi, Y. Binary Metal (Ti, Cu) Oxyhydroxy-Organic (Terephthalate) Framework. *J. Catal.* **2015**, *332*, 1−12.
(206) Tan, Z.-D.; Tan, H.-Y.; Shi, X.-Y.; Zhuan-Ji; Yan, Y.-F.; Yin-Zhou. Metal-Organic Framework MIL-53(Al)-Supported Copper Catalyst for CO Catalytic Oxidation Reaction. *Inorg. Chem. Commun.* **2015**, *61*, 128−131.
(207) Zamaro, J. M.; Pérez, N. C.; Miró, E. E.; Casado, C.; Seoane, B.; Téllez, C.; Coronas, J. HKUST-1 MOF: A matrix to synthesize CuO and CuO−CeO2 nanoparticle catalysts for CO oxidation. *Chem. Eng. J.* **2012**, *195−196*, 180−187.
(208) Keim, W. Oligomerization of Ethylene to α-Olefins. *Angew. Chem., Int. Ed.* **2013**, *52*, 12492−12496.
(209) McGuinness, D. S. Olefin Oligomerization via Metallacycles. *Chem. Rev.* **2011**, *111*, 2321−2341.
(210) Mlinar, A. N.; Baur, G. B.; Bong, G. G.; Getsoian, A. B.; Bell, A. T. Propene Oligomerization over Ni-Exchanged Na-X Zeolites. *J. Catal.* **2012**, *296*, 156−164.
(211) Heveling, J.; van der Beek, A.; de Pender, M. Oligomerization of Ethene over Nickel-Exchanged Zeolite y into a Diesel-Range Product. *Appl. Catal.* **1988**, *42*, 325−336.
(212) Olivier-Bourbigou, H.; Breuil, P. A. R.; Magna, L.; Michel, T.; Espada Pastor, M. F.; Delcroix, D. Nickel Catalyzed Olefin Oligomerization and Dimerization. *Chem. Rev.* **2020**, *120*, 7919−7983.
(213) Canivet, J.; Aguado, S.; Schuurman, Y.; Farrusseng, D. MOF-Supported Selective Ethylene Dimerization Single-Site Catalysts through One-Pot Postsynthetic Modification. *J. Am. Chem. Soc.* **2013**, *135*, 4195−4198.
(214) Yuan, S.; Zhang, P.; Zhang, L.; Garcia-Esparza, A. T.; Sokaras, D.; Qin, J.-S.; Feng, L.; Day, G. S.; Chen, W.; Drake, H. F.; et al. Exposed Equatorial Positions of Metal Centers via Sequential Ligand Elimination and Installation in MOFs. *J. Am. Chem. Soc.* **2018**, *140*, 10814−10819.
(215) Cossee, P. Ziegler-Natta Catalysis I. Mechanism of Polymerization of α-Olefins with Ziegler-Natta Catalysts. *J. Catal.* **1964**, *3*, 80−88.
(216) Arlman, E. J.; Cossee, P. Ziegler-Natta Catalysis III. Stereospecific Polymerization of Propene with the Catalyst System $TiCl_3$-$AlEt_3$. *J. Catal.* **1964**, *3*, 99−104.
(217) Roy, D.; Sunoj, R. B. Ni-, Pd-, or Pt-Catalyzed Ethylene Dimerization. *Org. Biomol. Chem.* **2010**, *8*, 1040−1051.
(218) Metzger, E. D.; Comito, R. J.; Hendon, C. H.; Dincă, M. Mechanism of Single-Site Molecule-Like Catalytic Ethylene Dimerization in Ni-MFU-4l. *J. Am. Chem. Soc.* **2017**, *139*, 757−762.
(219) Mlinar, A. N.; Keitz, B. K.; Gygi, D.; Bloch, E. D.; Long, J. R.; Bell, A. T. Selective Propene Oligomerization with Nickel(II)-Based Metal-Organic Frameworks. *ACS Catal.* **2014**, *4*, 717−721.
(220) Madrahimov, S. T.; Gallagher, J. R.; Zhang, G.; Meinhart, Z.; Garibay, S. J.; Delferro, M.; Miller, J. T.; Farha, O. K.; Hupp, J. T.; Nguyen, S. T. Gas-Phase Dimerization of Ethylene under Mild Conditions Catalyzed by MOF Materials Containing $(Bpy)Ni^{II}$ Complexes. *ACS Catal.* **2015**, *5*, 6713−6718.
(221) Kømurcu, M.; Lazzarini, A.; Kaur, G.; Borfecchia, E.; Øien-Ødegaard, S.; Gianolio, D.; Bordiga, S.; Lillerud, K. P.; Olsbye, U. Co-Catalyst Free Ethene Dimerization over Zr-Based Metal-Organic Framework (UiO-67) Functionalized with Ni and Bipyridine. *Catal. Today* **2021**, *369*, 193−202.
(222) Liu, J.; Ye, J.; Li, Z.; Otake, K.; Liao, Y.; Peters, A. W.; Noh, H.; Truhlar, D. G.; Gagliardi, L.; Cramer, C. J.; et al. Beyond the Active Site. *J. Am. Chem. Soc.* **2018**, *140*, 11174−11178.
(223) Agirrezabal-Telleria, I.; Luz, I.; Ortuño, M. A.; Oregui-Bengoechea, M.; Gandarias, I.; López, N.; Lail, M. A.; Soukri, M. Gas Reactions under Intrapore Condensation Regime within Tailored Metal-Organic Framework Catalysts. *Nat. Commun.* **2019**, *10*, 2076.
(224) Park, H. D.; Comito, R. J.; Wu, Z.; Zhang, G.; Ricke, N.; Sun, C.; Van Voorhis, T.; Miller, J. T.; Román-Leshkov, Y.; Dincă, M. Gas-Phase Ethylene Polymerization by Single-Site Cr Centers in a Metal-Organic Framework. *ACS Catal.* **2020**, *10*, 3864−3870.
(225) Weckhuysen, B. M.; Yu, J. Recent Advances in Zeolite Chemistry and Catalysis. *Chem. Soc. Rev.* **2015**, *44*, 7022−7024.
(226) Vogt, E. T. C.; Weckhuysen, B. M. Fluid Catalytic Cracking. *Chem. Soc. Rev.* **2015**, *44*, 7342−7370.
(227) Vimont, A.; Goupil, J.-M.; Lavalley, J.-C.; Daturi, M.; Surblé, S.; Serre, C.; Millange, F.; Férey, G.; Audebrand, N. Investigation of Acid Sites in a Zeotypic Giant Pores Chromium(III) Carboxylate. *J. Am. Chem. Soc.* **2006**, *128*, 3218−3227.
(228) Volkringer, C.; Leclerc, H.; Lavalley, J.-C.; Loiseau, T.; Férey, G.; Daturi, M.; Vimont, A. Infrared Spectroscopy Investigation of the Acid Sites in the Metal-Organic Framework Aluminum Trimesate MIL-100(Al). *J. Phys. Chem. C* **2012**, *116*, 5710−5719.
(229) Leclerc, H.; Vimont, A.; Lavalley, J.-C.; Daturi, M.; Wiersum, A. D.; Llwellyn, P. L.; Horcajada, P.; Férey, G.; Serre, C. Infrared Study of the Influence of Reducible Iron(III) Metal Sites on the Adsorption of CO, CO_2, Propane, Propene and Propyne in the Mesoporous Metal-Organic Framework MIL-100. *Phys. Chem. Chem. Phys.* **2011**, *13*, 11748−11756.
(230) Schmidt, F. New Catalyst Preparation Technologies—Observed from an Industrial Viewpoint. *Appl. Catal. Gen.* **2001**, *221*, 15−21.
(231) Jiang, J.; Gándara, F.; Zhang, Y.-B.; Na, K.; Yaghi, O. M.; Klemperer, W. G. Superacidity in Sulfated Metal-Organic Framework-808. *J. Am. Chem. Soc.* **2014**, *136*, 12844−12847.
(232) Trickett, C. A.; Osborn Popp, T. M.; Su, J.; Yan, C.; Weisberg, J.; Huq, A.; Urban, P.; Jiang, J.; Kalmutzki, M. J.; Liu, Q.; et al. Identification of the Strong Brønsted Acid Site in a Metal-Organic Framework Solid Acid Catalyst. *Nat. Chem.* **2019**, *11*, 170−176.

https://doi.org/10.1021/acs.chemrev.2c00537
Chem. Rev. XXXX, XXX, XXX−XXX

(233) Liu, P.; Redekop, E.; Gao, X.; Liu, W.-C.; Olsbye, U.; Somorjai, G. A. Oligomerization of Light Olefins Catalyzed by Brønsted-Acidic Metal-Organic Framework-808. *J. Am. Chem. Soc.* **2019**, *141*, 11557−11564.
(234) Kajiwara, T.; Higuchi, M.; Yuasa, A.; Higashimura, H.; Kitagawa, S. One-Dimensional Alignment of Strong Lewis Acid Sites in a Porous Coordination Polymer. *Chem. Commun.* **2013**, *49*, 10459−10461.
(235) Kiyonaga, T.; Higuchi, M.; Kajiwara, T.; Takashima, Y.; Duan, J.; Nagashima, K.; Kitagawa, S. Dependence of Crystal Size on the Catalytic Performance of a Porous Coordination Polymer. *Chem. Commun.* **2015**, *51*, 2728−2730.
(236) Sabyrov, K.; Jiang, J.; Yaghi, O. M.; Somorjai, G. A. Hydroisomerization of n-Hexane Using Acidified Metal-Organic Framework and Platinum Nanoparticles. *J. Am. Chem. Soc.* **2017**, *139*, 12382−12385.
(237) Ahn, S.; Nauert, S. L.; Buru, C. T.; Rimoldi, M.; Choi, H.; Schweitzer, N. M.; Hupp, J. T.; Farha, O. K.; Notestein, J. M. Pushing the Limits on Metal-Organic Frameworks as a Catalyst Support. *J. Am. Chem. Soc.* **2018**, *140*, 8535−8543.
(238) Rahmani, E.; Rahmani, M. Alkylation of Benzene over Fe-Based Metal Organic Frameworks (MOFs) at Low Temperature Condition. *Microporous Mesoporous Mater.* **2017**, *249*, 118−127.
(239) Rahmani, E.; Rahmani, M. Al-Based MIL-53 Metal Organic Framework (MOF) as the New Catalyst for Friedel-Crafts Alkylation of Benzene. *Ind. Eng. Chem. Res.* **2018**, *57*, 169−178.
(240) Bertleff, W.; Roeper, M.; Sava, X. Carbonylation. In *Ullmann's Encyclopedia of Industrial Chemistry*; Wiley-VCH, 2007.
(241) Berre, C. L.; Serp, P.; Kalck, P.; Torrence, G. P. Acetic Acid. In *Ullmann's Encyclopedia of Industrial Chemistry*; Wiley-VCH, 2014; pp 1−34.
(242) Bloch, W. M.; Burgun, A.; Coghlan, C. J.; Lee, R.; Coote, M. L.; Doonan, C. J.; Sumby, C. J. Capturing Snapshots of Post-Synthetic Metallation Chemistry in Metal-Organic Frameworks. *Nat. Chem.* **2014**, *6*, 906−912.
(243) Burgun, A.; Coghlan, C. J.; Huang, D. M.; Chen, W.; Horike, S.; Kitagawa, S.; Alvino, J. F.; Metha, G. F.; Sumby, C. J.; Doonan, C. J. Mapping-Out Catalytic Processes in a Metal-Organic Framework with Single-Crystal X-Ray Crystallography. *Angew. Chem., Int. Ed.* **2017**, *56*, 8412−8416.
(244) Lee, J. T.; Thomas, P. J.; Alper, H. Synthesis of β-Lactones by the Regioselective, Cobalt and Lewis Acid Catalyzed Carbonylation of Simple and Functionalized Epoxides. *J. Org. Chem.* **2001**, *66*, 5424−5426.
(245) Mahadevan, V.; Getzler, Y. D. Y. L.; Coates, G. W. [Lewis Acid]$^+$[Co(CO)$_4$]$^-$ Complexes. *Angew. Chem., Int. Ed.* **2002**, *41*, 2781−2784.
(246) Park, H. D.; Dincă, M.; Román-Leshkov, Y. Heterogeneous Epoxide Carbonylation by Cooperative Ion-Pair Catalysis in Co(CO)$_4$—Incorporated Cr-MIL-101. *ACS Cent. Sci.* **2017**, *3*, 444−448.
(247) Park, H. D.; Dincă, M.; Román-Leshkov, Y. Continuous-Flow Production of Succinic Anhydrides via Catalytic β-Lactone Carbonylation by Co(CO)$_4$⊂Cr-MIL-101. *J. Am. Chem. Soc.* **2018**, *140*, 10669−10672.
(248) Mon, M.; Rivero-Crespo, M. A.; Ferrando-Soria, J.; Vidal-Moya, A.; Boronat, M.; Leyva-Pérez, A.; Corma, A.; Hernández-Garrido, J. C.; López-Haro, M.; Calvino, J. J.; et al. Synthesis of Densely Packaged, Ultrasmall Pt02 Clusters within a Thioether-Functionalized MOF. *Angew. Chem., Int. Ed.* **2018**, *57*, 6186−6191.
(249) Chen, H.; Snurr, R. Q. Insights into Catalytic Gas-Phase Hydrolysis of Organophosphate Chemical Warfare Agents by MOF-Supported Bimetallic Metal-Oxo Clusters. *ACS Appl. Mater. Interfaces* **2020**, *12*, 14631−14640.
(250) Kirlikovali, K. O.; Chen, Z.; Islamoglu, T.; Hupp, J. T.; Farha, O. K. Zirconium-Based Metal-Organic Frameworks for the Catalytic Hydrolysis of Organophosphorus Nerve Agents. *ACS Appl. Mater. Interfaces* **2020**, *12*, 14702−14720.
(251) Wang, H.; Mahle, J. J.; Tovar, T. M.; Peterson, G. W.; Hall, M. G.; DeCoste, J. B.; Buchanan, J. H.; Karwacki, C. J. Solid-Phase Detoxification of Chemical Warfare Agents Using Zirconium-Based Metal Organic Frameworks and the Moisture Effects. *ACS Appl. Mater. Interfaces* **2019**, *11*, 21109−21116.
(252) Hasan, Z.; Jun, J. W.; Jhung, S. H. Sulfonic Acid-Functionalized MIL-101(Cr). *Chem. Eng. J.* **2015**, *278*, 265−271.
(253) Sattler, A.; Aluthge, D. C.; Winkler, J. R.; Labinger, J. A.; Bercaw, J. E. Enhanced Productivity of a Supported Olefin Trimerization Catalyst. *ACS Catal.* **2016**, *6*, 19−22.
(254) Velthoen, M. E. Z.; Muñoz-Murillo, A.; Bouhmadi, A.; Cecius, M.; Diefenbach, S.; Weckhuysen, B. M. The Multifaceted Role of Methylaluminoxane in Metallocene-Based Olefin Polymerization Catalysis. *Macromolecules* **2018**, *51*, 343−355.
(255) Kleinhaus, J. T.; Wittkamp, F.; Yadav, S.; Siegmund, D.; Apfel, U.-P. [FeFe]-Hydrogenases. *Chem. Soc. Rev.* **2021**, *50*, 1668−1784.
(256) Welch, G. C.; Juan, R. R. S.; Masuda, J. D.; Stephan, D. W. Reversible, Metal-Free Hydrogen Activation. *Science* **2006**, *314*, 1124−1126.
(257) Stephan, D. W. Frustrated Lewis Pairs. *Org. Biomol. Chem.* **2008**, *6*, 1535−1539.
(258) Stephan, D. W.; Greenberg, S.; Graham, T. W.; Chase, P.; Hastie, J. J.; Geier, S. J.; Farrell, J. M.; Brown, C. C.; Heiden, Z. M.; Welch, G. C.; et al. Metal-Free Catalytic Hydrogenation of Polar Substrates by Frustrated Lewis Pairs. *Inorg. Chem.* **2011**, *50*, 12338−12348.
(259) Chernichenko, K.; Madarász, A.; Pápai, I.; Nieger, M.; Leskelä, M.; Repo, T. A Frustrated-Lewis-Pair Approach to Catalytic Reduction of Alkynes to Cis-Alkenes. *Nat. Chem.* **2013**, *5*, 718−723.
(260) Chen, D.; Wang, Y.; Klankermayer, J. Enantioselective Hydrogenation with Chiral Frustrated Lewis Pairs. *Angew. Chem., Int. Ed.* **2010**, *49*, 9475−9478.
(261) Fontaine, F.-G.; Stephan, D. W. On the Concept of Frustrated Lewis Pairs. *Philos. Trans. R. Soc. Math. Phys. Eng. Sci.* **2017**, *375*, 20170004.
(262) McDonald, T. M.; Mason, J. A.; Kong, X.; Bloch, E. D.; Gygi, D.; Dani, A.; Crocellà, V.; Giordanino, F.; Odoh, S. O.; Drisdell, W. S.; et al. Cooperative Insertion of CO_2 in Diamine-Appended Metal-Organic Frameworks. *Nature* **2015**, *519*, 303−308.
(263) Shyshkanov, S.; Nguyen, T. N.; Chidambaram, A.; Stylianou, K. C.; Dyson, P. J. Frustrated Lewis Pair-Mediated Fixation of CO_2 within a Metal-Organic Framework. *Chem. Commun.* **2019**, *55*, 10964−10967.
(264) Shyshkanov, S.; Nguyen, T. N.; Ebrahim, F. M.; Stylianou, K. C.; Dyson, P. J. In Situ Formation of Frustrated Lewis Pairs in a Water-Tolerant Metal-Organic Framework for the Transformation of CO2. *Angew. Chem., Int. Ed.* **2019**, *58*, 5371−5375.
(265) Niu, Z.; Zhang, W.; Lan, P. C.; Aguila, B.; Ma, S. Promoting Frustrated Lewis Pairs for Heterogeneous Chemoselective Hydrogenation via the Tailored Pore Environment within Metal-Organic Frameworks. *Angew. Chem., Int. Ed.* **2019**, *58*, 7420−7424.
(266) Singh, D.; Buratto, W. R.; Torres, J. F.; Murray, L. J. Activation of Dinitrogen by Polynuclear Metal Complexes. *Chem. Rev.* **2020**, *120*, 5517−5581.
(267) Wang, C.-H.; Das, A.; Gao, W.-Y.; Powers, D. C. Probing Substrate Diffusion in Interstitial MOF Chemistry with Kinetic Isotope Effects. *Angew. Chem., Int. Ed.* **2018**, *57*, 3676−3681.

https://doi.org/10.1021/acs.chemrev.2c00537
Chem. Rev. XXXX, XXX, XXX−XXX